CHARACTERIZING D-REGION ROUGHNESS USING LF/MF SIGNALS OF OPPORTUNITY

A Dissertation
Presented to
The Academic Faculty

By

Marc A. Higginson-Rollins

In Partial Fulfillment
of the Requirements for the Degree
Doctor of Philosophy in the
School of Electrical and Computer Engineering

Georgia Institute of Technology

May 2020

CHARACTERIZING D-REGION ROUGHNESS USING LF/MF SIGNALS OF OPPORTUNITY

Approved by:

Dr. Morris Cohen, Advisor
School of Electrical and Computer Engineering
Georgia Institute of Technology

Dr. Waymond Scott
School of Electrical and Computer Engineering
Georgia Institute of Technology

Dr. Gregory Durgin
School of Electrical and Computer Engineering
Georgia Institute of Technology

Dr. Sven Simon
School of Earth and Atmospheric Sciences
Georgia Institute of Technology

Dr. Alessio Medda
School of Electrical Engineering and Computer Engineering
Georgia Institute of Technology

Date Approved: March 19, 2020

To my loving family

Johanne, Alex, and Paige

ACKNOWLEDGEMENTS

First and foremost I would like to thank Professor Morris B. Cohen. He challenged me academically and provided me with thoughtful guidance and mentorship along the way. In addition, I am grateful for the many development opportunities he graciously made available to me along my doctoral path.

Thank you to my committee members: Dr. Waymond Scott, Dr. Gregory Durgin, Dr. Sven Simon, and Dr. Alessio Medda for their feedback, guidance, and patience through this process.

I am grateful to all members of the Georgia Tech LF Radio Lab. This thesis would not be possible if it were not for everyone's contributions towards the construction, deployment, operation, and maintenance of the Lab's radio receivers and support of the many field campaigns that collected the data used in this thesis. Thank you: Parker Singletary, Edward Slevin, Nathan Opalinski, Kevin Whitmore, Jackson McCormick, Nicholas Gross, Lee Thompson, Nikhil Pailoor, and all other members. Also, thank you Alex Akins, Amorée Hodges, and Amadeo Bellotti for your friendship.

I deeply appreciate the love and support of my family. I thank my sister, Paige, for her friendship and my mother, Johanne, and father, Alex, for their countless sacrifices. Without my family I wouldn't be where I am today.

This work was supported by the National Science Foundation under grants AGS 1451142 and AGS 1653114 (CAREER) to the Georgia Institute of Technology. The author's work was also supported by the NSF Graduate Research Fellowship, DGE 1650044.

TABLE OF CONTENTS

LIST OF TABLES

LIST OF FIGURES

SUMMARY

The D-region of the ionosphere, which ranges from about 60−100 km, is too high for continuous in-situ measurements, such as with high-altitude balloons, and too low for satellite-based measurements. As such, its properties remain largely unknown compared to other layers of the atmosphere and near-Earth space environment. Utilization of Very Low Frequency (VLF, 3−30 kHz) radio waves has proven to be useful for global, continuous D-region diagnostics. A ground-based radio receiver detects a signal from some distant source that propagates in the "Earth-Ionosphere waveguide". Changes in the signal with time are known to correspond to changes in the ionospheric conditions, which serves as an indirect measure of the D-region.

The small-scale roughness of the D-region electron density is not well understood. The bulk of VLF research studying the D-region has been focused on global or regional studies, and typically all assume a stratified ionosphere. Some works examined more localized variation, but these studies are by no means exhaustive and fail to truly characterize roughness on a scale less than 10-100 km, particularly under ambient conditions. Early work done using the partial reflection technique touches on the idea of "small-scale roughness", but the work was limited in scope and focused on understanding the mechanism of weak partial reflections rather than characterizing the roughness. This work presents a technique to characterize the roughness of the D-region electron density using Low Frequency (LF; $30 - 300$ kHz) and Medium Frequency (MF; $300 - 3000$ kHz) signals of opportunity. The horizontal roughness is measured using the correlation length scale and the vertical roughness is measured using the differential phase height. Field campaign measurements of both metrics are presented. The Monte Carlo Method (MCM) is applied to a Finite-Difference Time-Domain (FDTD) model to connect correlation length scale measurements to a parameterization of the electron density roughness, the ionospheric length scale. The ionospheric length scale values for two sets of field measurements are presented. Results show that this modeling technique can only characterize a small percentage of the observed data.

CHAPTER 1
INTRODUCTION AND BACKGROUND

1.1 Research Purpose

The D-region of the ionosphere, which ranges from about 60−100 km, is too high for continuous in-situ measurements, such as with high-altitude balloons, and too low for satellite-based measurements. As such, its properties remain largely unknown compared to other layers of the atmosphere and near-Earth space environment. However, this layer heavily impacts the attenuation of long-distance terrestrial communication signals and contributes to the absorption of satellite communication signals. Different remote sensing methods have been developed since the early 20th century to study this region, which will be discussed in more detail in Section 1.5. Figure 1.1 outlines at a high level the capabilities of current methods. Spatial resolution of the received signal is roughly related to the inverse wavelength of the signal, which determines the smallest feature in the D-region in which a reflecting wave would be "sensitive" to, and temporal resolution refers to the sampling rate of the method. The purpose of this research is to outline, validate, and leverage a new method of lower ionosphere remote sensing, which fills a capability gap in current methods, as seen in Figure 1.1.

Current methods for D-region sensing either use: 1) a forward modeling scheme in which data is detected and then the parameters of a model are adjusted to match the data, 2) a direct inference method that derives characteristics directly from the data. Ideally, we would like a remote sensing technique that allows direct ionospheric observation without the use of forward modeling, while still being applied with high time resolution and over long distances. Here we propose a method of D-region remote sensing that achieves this by utilizing signals of opportunity from the Nationwide Differential Global Position System (NDGPS) network, a collection of beacons which transmit ionospheric correction factors on frequencies between 285 and 325 kHz. Waves in the Low Frequency (LF; 30−300 kHz) and Medium Frequency (MF; 300−3000 kHz) range are known to travel in the Earth-

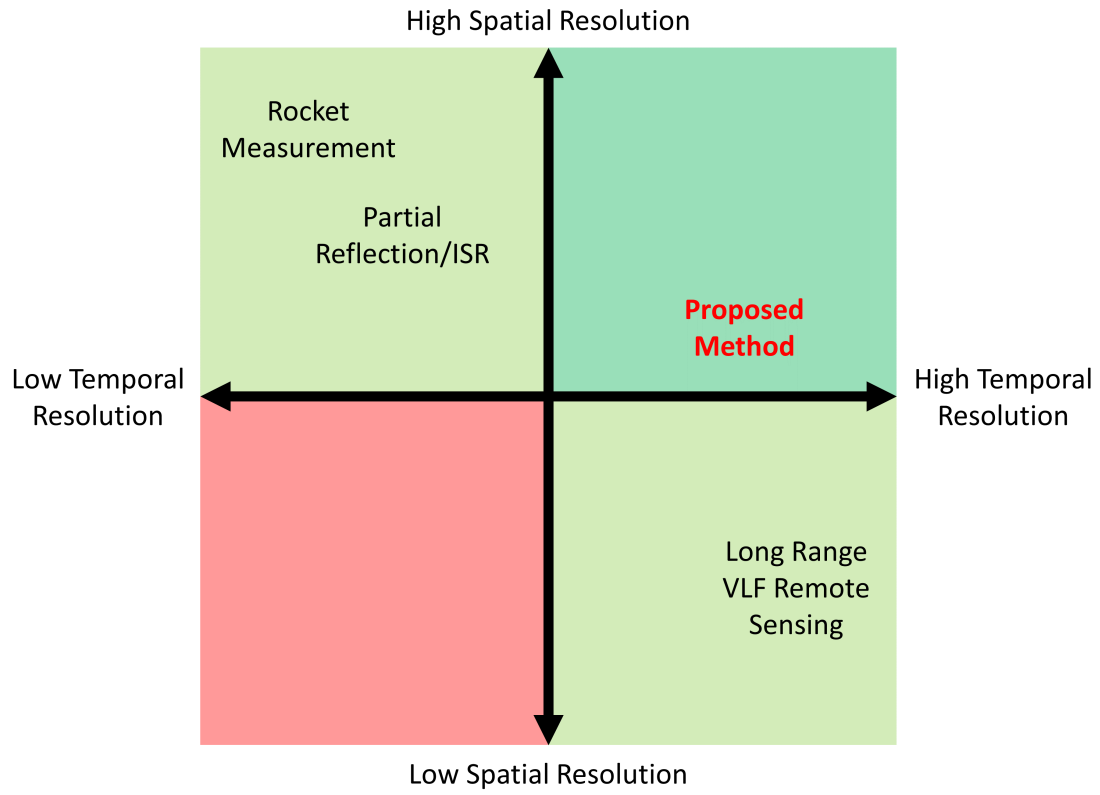

Figure 1.1: Summary of the prevalent methods currently used for D region remote sensing.

ionosphere waveguide, i.e. reflecting off the D-region of the ionosphere and the Earth in some combination, but with relatively high attenuation rates. Thus, at medium to long distances, waves only reflecting once or twice off the ionosphere are detectable [*Belrose et al.*, 1959]. On the other hand, LF/MF waves reflect efficiently enough to be detected thousands of kilometers away from the source, at least if a sufficiently sensitive receiver is used, allowing large ionospheric regions to nonetheless be observed. Research in the 20th century has exploited this phenomena to yield an abundance of publications, [e.g. *Huxley and Ratcliffe*, 1949; *Sprenger et al.*, 1962]. In this sense, LF/MF remote sensing is advantageous for ionospheric remote sensing.

The small-scale roughness of the D-region is not well understood. The bulk of VLF research studying the D-region has been focused on global or regional studies, and typically all assume a stratified ionosphere. Some previous work done at VLF, e.g. *Lay and Shao* [2011a,b]; *Füllekrug et al.* [2015a], examined more localized variation, but these studies are

by no means exhaustive and fail to truly characterize roughness on a scale less than 10-100 km, particularly under ambient conditions. Early work done using the partial reflection technique (see Section 1.5) touches on the idea of "small-scale roughness", but the work was limited in scope and focused on understanding the mechanism of weak partial reflections rather than characterizing the roughness. Figure 1.2 depicts a cartoon difference of a smooth, stratified ionosphere versus a rough ionosphere. The left panel of the figure is what has generally been used for VLF studies. The right panel, with the rough ionosphere, represents perhaps a more realistic scenario since the D-region and ionosphere are turbulent, non-stationary mediums. The goal of this research falls into two major pillars: 1) to validate use of the signals from NDGPS transmitters as a method for D-region remote sensing, 2) to use this technique to develop a method to characterize the small-scale "roughness" of the D-region. The second pillar, studying this electromagnetic roughness can be further broken down by: 1) measuring the correlation length scale, 2) measuring the height variation of reflections, 3) leverage modeling to connect the roughness metrics to D-region electron density, and 4) propose a theoretical D-region roughness observatory to measure the roughness metrics on a continual basis.

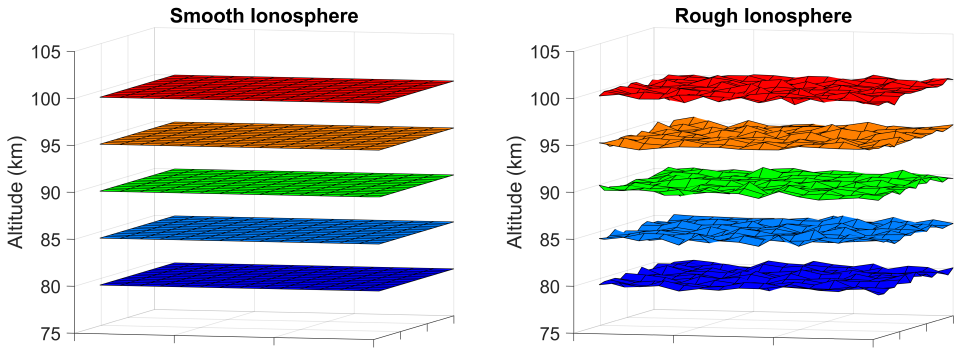

Figure 1.2: Cartoon depiction of a smooth ionosphere, left panel, and a rough ionosphere, right panel.

1.2 The NDGPS Network

The United States Coast Guard (USCG) operates the Nationwide Differential Global Position System (NDGPS). As of October 2018, the network consists of 33 sites which broadcast

the difference between a known, fixed location and the received GPS coordinates to improve the accuracy of commercial GPS to centimeter accuracy. The current coverage and site locations of NDGPS are shown in Figure 1.3. Some of the data presented in this thesis was collected prior to August 2016 when there were 84 operational NDGPS sites.

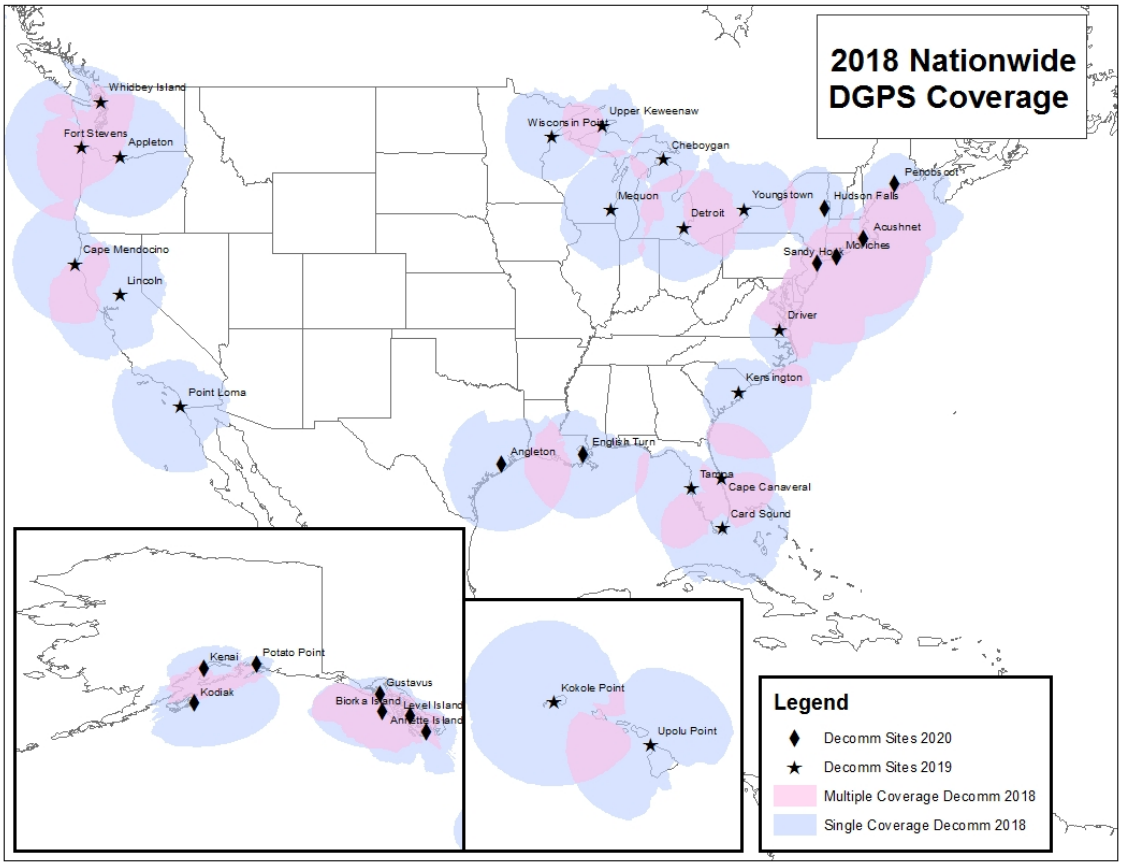

Figure 1.3: Map of the locations of the NDGPS transmitters and their respective coverage, *Emerson* [2018].

The different NDGPS towers transmit the correction values on beacon frequencies between 285−325 kHz and are geographically clustered along the coast and major waterways. There are four different antenna types used by the USCG at NDGPS sites with a transmitter carrier operating power between 50 and 1000 Watts: (1) a VALCOM 74-foot whip antenna ($\leq$3% efficiency), (2) a guyed ROHN tower in 90-ft (6-8% efficiency), 120-ft, and 150-ft heights (20% efficient), (3) the Longwire (approximately 13% efficiency), and (4) converted United States Air Force (USAF) Ground Wave Emergency Network (GWEN) sites which are 299-ft tall (approximately 55% efficiency) [*Wolfe et al.*, 2000].

1.3 Data Acquisition

1.3.1 The LF AWESOME Receiver

We have designed and developed an upgraded version of the VLF AWESOME (Atmospheric Weather Electromagnetic System for Observation, Modeling, and Education) Receiver, *Cohen et al.* [2010]. The updated receiver, called the LF AWESOME Receiver [*Cohen et al.*, 2018b], consists of two orthogonal air-core loop antennas, as in Figure 1.4, and has a sampling rate of 1 MHz. The pass band is approximately 0.5−470 kHz, with sensitivity up to 0.03 fT/$\sqrt{Hz}$ at 30 kHz and 0.1 fT/$\sqrt{Hz}$ at 300 kHz, and RMS timing accuracy of 15−20 ns based on the timing pulses that make up the 1 MHz clock. This implies precise phase estimation of <1.5 degrees at 300 kHz and there is no frequency drift/offset in the clock detectable with 0.5 part-per-billion resolution. In order to fully take advantage of the receiver sensitivity, the receiver must be in an electromagnetically quiet location. A signal cable ($\gtrsim$1000 ft) runs from the antenna to the backend of the system where sampling, AAF, and digital processing is done, see Figure 1.5. The key distinguishing feature of the receiver is its high sensitivity, which enables even weak LF/MF signals to be detected at long range.

1.3.2 The Georgia Tech Receiver Network

As of March 2019, the Georgia Tech LF Group operates 10 receivers across the United States. The map in Figure 1.6 shows the geographic distribution of the receivers. The network consists of 2 in Alaska, 7 in the continental US (CONUS), and 1 in Puerto Rico. The majority of the work for this thesis utilizes data from the subset in the southeast United States, which includes four receivers–PARI (NC), Briarwood (GA), Baxley (GA), and Oxford (MS).

1.4 LF/MF Waves in the Ionosphere

1.4.1 The D-Region of the Ionosphere

In general, the ionosphere, which extends from 60−1000 km, is seen as a mixture between the "neutral atmosphere" of the Earth, primarily consisting of neutral nitrogen and oxygen,

Figure 1.4: The front end of the LF AWESOME Receiver, consists of two orthogonal air-core loop antennas and a pre-amplifier (gray box).

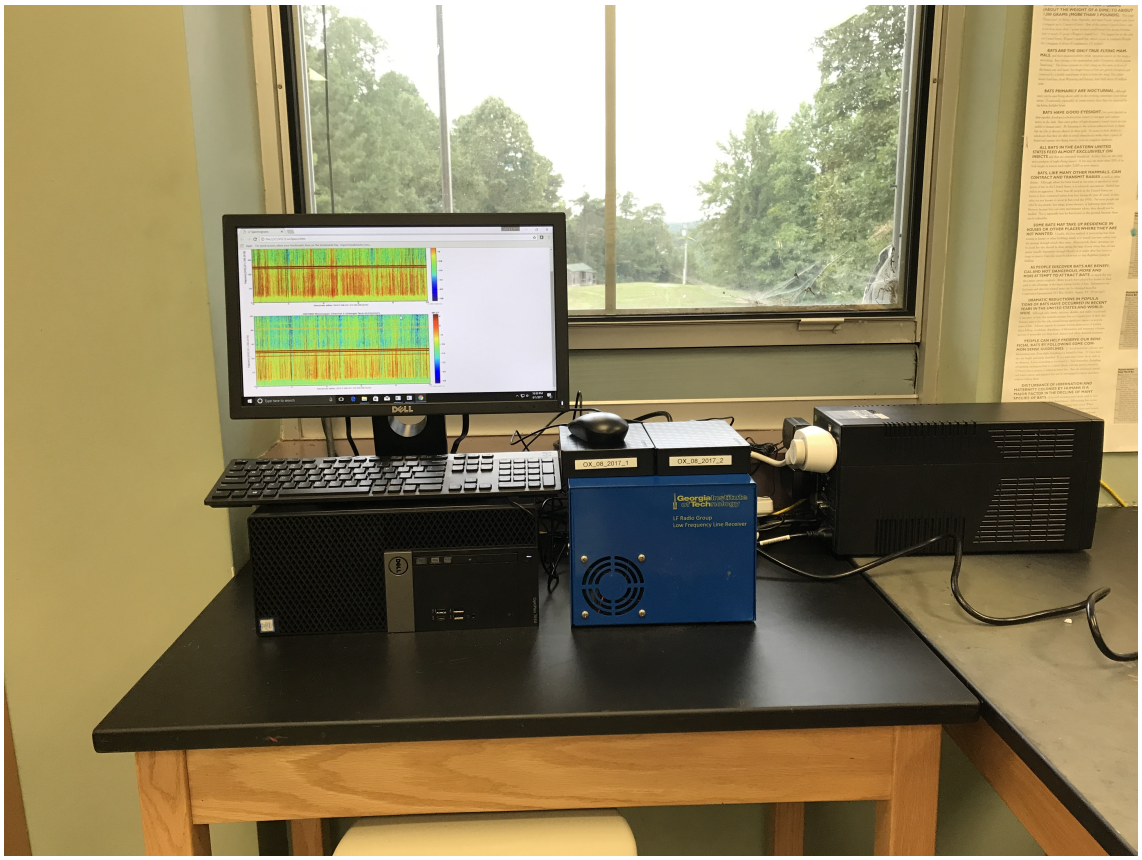

Figure 1.5: The back end of the LF AWESOME Receiver, consists of a desktop PC and Line Receiver (blue box).

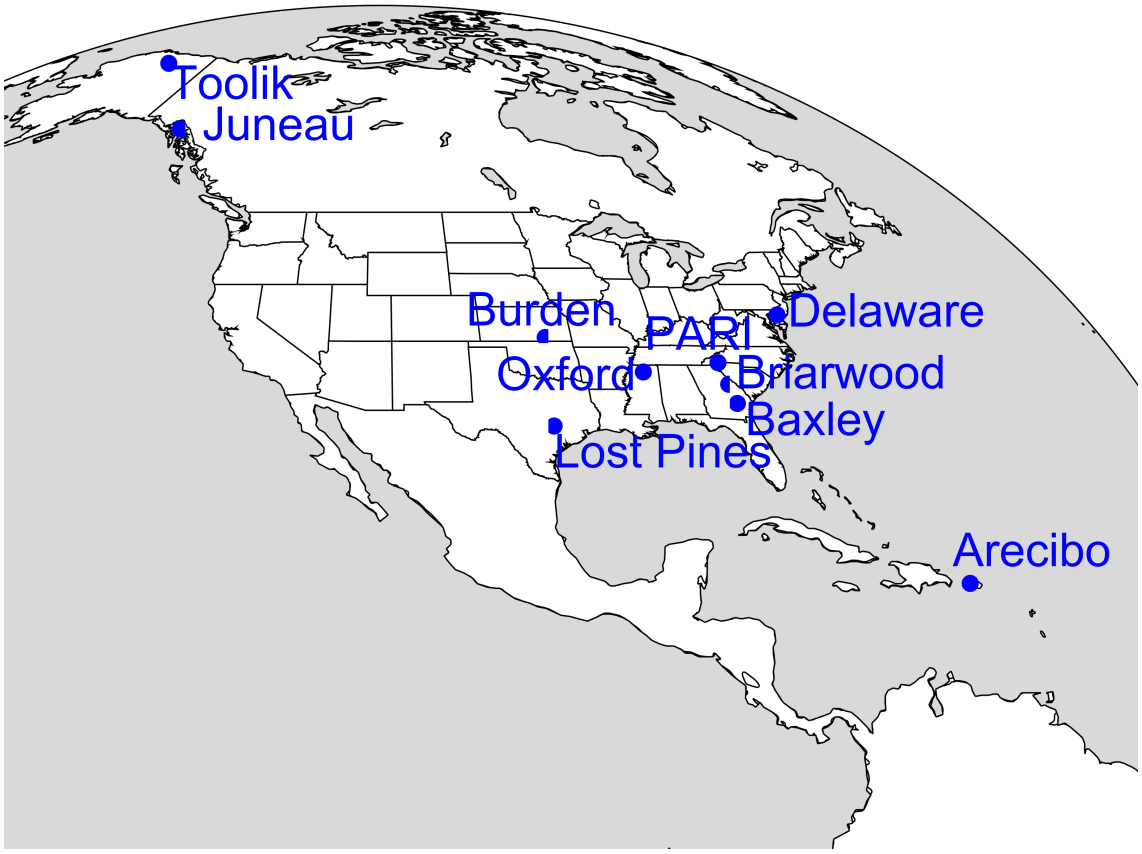

Figure 1.6: Map of the LF AWESOME Receivers active in the field as of March 2019.

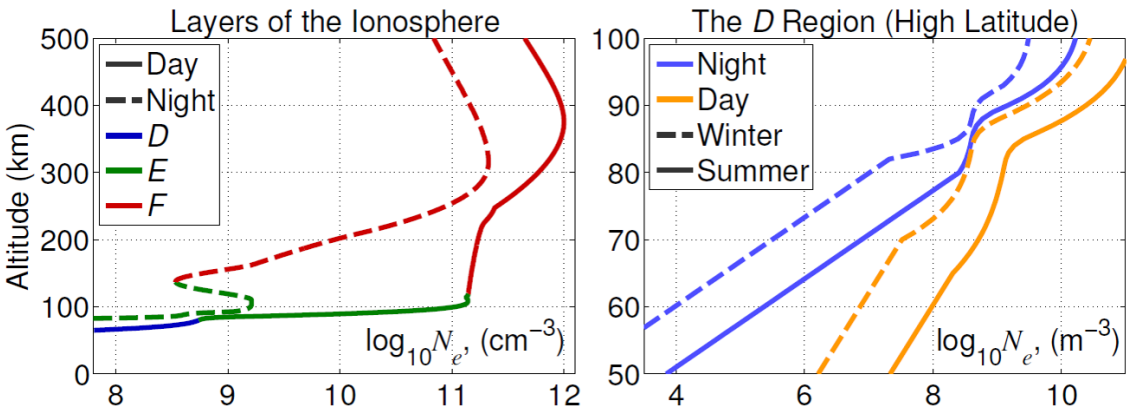

Figure 1.7: Example electron density. Left panel shows the full ionosphere for day/night. Right panel shows a more detailed version of the D-region. Figure adapted from *Cohen* [2009].

and the space environment above the ionosphere, also called the "magnetosphere", which consists primarily of charged particles (i.e. electrons, protons, and ions), or "plasma". When the plasma is magnetized, as in the case of the ionosphere, the plasma is said to be *anisotropic*, which means that it responds differently to applied $\bar{E}$ in different directions.

The ionized part of the atmosphere stretching from about 60−90 km is called the "D-region". Molecular oxygen and nitrogen, nitric oxide, and other atoms, such as sodium and calcium, constitute this layer of ionization *Nicolet and Aikin* [1960]. The ionization in the D-region of the ionosphere is primarily due to Lyman-α radiation during the day and cosmic rays and Lyman-β backscatter from the Earth's hydrogen exosphere at night *Kotovsky and Moore* [2016]. Thus, D-region electron densities are substantially larger during the day, and are subject to diurnal, seasonal, and solar-cycle variation. During the day, the ionospheric conditions are highly stable and predictable apart from during transient solar flare disturbances. On the other hand, nighttime ionospheric conditions are highly erratic due to the unpredictable nature of its sources.

Within the ionosphere, and especially in the lower ionosphere, the collision between neutral and charged particles plays a very important role. As a wave propagates through the ionosphere, the induced electric field moves the electrons, which in turn collide with the neutral particles (electron-neutral collision frequency) attenuating the wave. In general, since the electron-neutral collision frequency is often normalized by the angular frequency,

as altitude increases, the collision frequency decreases. However, simultaneously, as the altitude increases the electron plasma frequency increases. The inverse of this fundamental plasma parameter is approximately the minimum time required for a plasma to react to changes. Once the normalized electron-neutral collision frequency and normalized electron plasma frequency are equal, the plasma can no longer react quick enough to the traveling wave and it is reflected. This typically only happens with lower frequency waves (e.g. ELF, VLF, MF, HF), while higher frequency waves will penetrate the ionosphere. The described interaction between waves and the ionosphere is summarized by the "Appleton-Hartree Equation":

$$n^2 = 1 - \frac{X}{1 - jZ - \frac{Y^2 \sin^2\theta}{2(1-X-jZ)} \pm \sqrt{\left[\frac{Y^2 \sin^2\theta}{2(1-X-jZ)}\right]^2 + Y^2 \cos^2\theta}}\,, \tag{1.1}$$

where

$$X = \frac{\omega_{pe}^2}{\omega^2}\,, \qquad Y = \frac{\omega_{ce}}{\omega}\,, \qquad Z = \frac{\nu_e}{\omega}\,, \tag{1.2}$$

describe the electron plasma frequency (ω_{pe}), the electron gyro frequency (ω_{ce}), and the electron-neutral collision frequency (ν_e). The variable θ is the spatial angle between the wavevector $\mathbf{k}$ and Earth's background magnetic flux density $\mathbf{B}_0$ [*Ratcliffe*, 1959].

The left-hand-side of Equation 1.1 is the square of the index of refraction, a parameter that is fundamental for understanding propagation through the D-region and long distance terrestrial propagation of low frequency waves. This parameter is a function of three main unknowns: 1) the magnetic flux density, 2) the electron-neutral collision frequency, and 3) the electron density – all of which vary as a function of altitude. Values for the magnetic flux density are readily available from the numerous magnetic models available for the Earth, such as the International Geomagnetic Reference Field [*Thébault et al.*, 2015]. In contrast, the collision frequency and electron density are difficult to predict due to their dynamic nature. Existing models, such as the International Reference Ionosphere (IRI), *Bilitza et al.* [2017], aren't useful for studying changes D-region electron densities due to perturbations and vary vastly even under ambient conditions, *Han et al.* [2011]. These two parameters will be discussed in greater depth in the following sections.

There are a wealth of additional nuances found in Equation 1.1. First, the index of refraction is a complex term. The imaginary part is associated with wave attenuation. When the collision frequency goes to zero, the imaginary term disappears and there is no longer any wave attenuation. Second, the anisotropy of the D-region is expressed in the equation through θ. The angle of the background magnetic flux density, relative to the wave vector, controls the index of refraction as a function of direction of propagation. This term is why low-frequency propagation is very different between North-South and East-West paths and varies with latitudes, e.g. *Barr* [1971]. Finally, the $\pm$ sign in the equation creates a polarization dependence for the propagating radio wave. In the case of a wave propagating parallel to the background magnetic field ($\theta = 0°$), the '+' sign defines the left-hand mode and the '$-$' sign defines the right-hand mode. In the case of a wave propagating perpendicular to the background magnetic field ($\theta = \pm 90°$), the '+' sign defines the ordinary mode and the '$-$' sign defines the extraordinary mode. A well-known result of this birefringent phenomena is an effect known as "Faraday rotation" that occurs in transionospheric propagating radio waves. A summary of this polarization dependence and related topics can be found in *Piggott* [1953].

1.4.2 Electron Density

As previously stated when describing Equation 1.1, the electron density is difficult to predict due to its dynamic nature. Determining high fidelity electron density altitude profiles for the D-region using reflections from low frequency waves is a difficult problem. In general, the fidelity of a profile is related to the number of parameters that can be solved or optimized for, but, since VLF/LF measurement techniques only measure amplitude and phase for a single frequency over some path, it is much simpler to use two parameterized functions for the electron density and collision frequency. In practice, these parameterized functions are typically used in a *forward modeling* scheme in which a propagation model varies the parameters until the amplitude/phase match the observed results [e.g. *Thomson et al.*, 2007].

$$N_e(h) = 1.43 \cdot 10^{13} e^{-0.15h} e^{\beta(h-h')} \quad \mathrm{m}^{-3} \tag{1.3}$$

A widely used parameterization of the D-region electron density is the "Wait and Spies Two Parameter Model". This model was derived by *Wait and Spies* [1964] who used laboratory measurements, ionospheric sounding rocket measurements, and VLF propagation measurements to empirically derive exponential profiles for the electron density. The derived exponential electron density profile, Equation 1.3, uses two input parameters, called *waveguide parameters* to approximate the D-region electron density. The first parameter, h' (km), can be *roughly* thought of as the "y-intercept" of the equation since an increase or decrease in this value is typically associated with the electron density moving up or down. However, the electron density is not physically moving in altitude, but rather the ionization in the D-region is decreasing or increasing respectively. The second parameter, β (km^{-1}), can be thought of as the "slope" of the equation in logarithmic plots. This term describes the gradient of the D-region electron density. An increasing value would mean that the gradient increases, i.e. the D-region has become "sharper".

Table 1.1: Typical values for h' and β for a 30 kHz wave, taken from *Morfitt* [1977]; *Ferguson* [1980].

		Summer	Winter
High Latitude	Day	$\beta = 0.3$, $h' = 72$	$\beta = 0.3$, $h' = 72$
	Night	$\beta = 0.54$, $h' = 87$	$\beta = 1.2$, $h' = 76$
Middle Latitude	Day	$\beta = 0.5$, $h' = 70$	$\beta = 0.3$, $h' = 72$
	Night	$\beta = 0.54$, $h' = 87$	$\beta = 0.54$, $h' = 88$

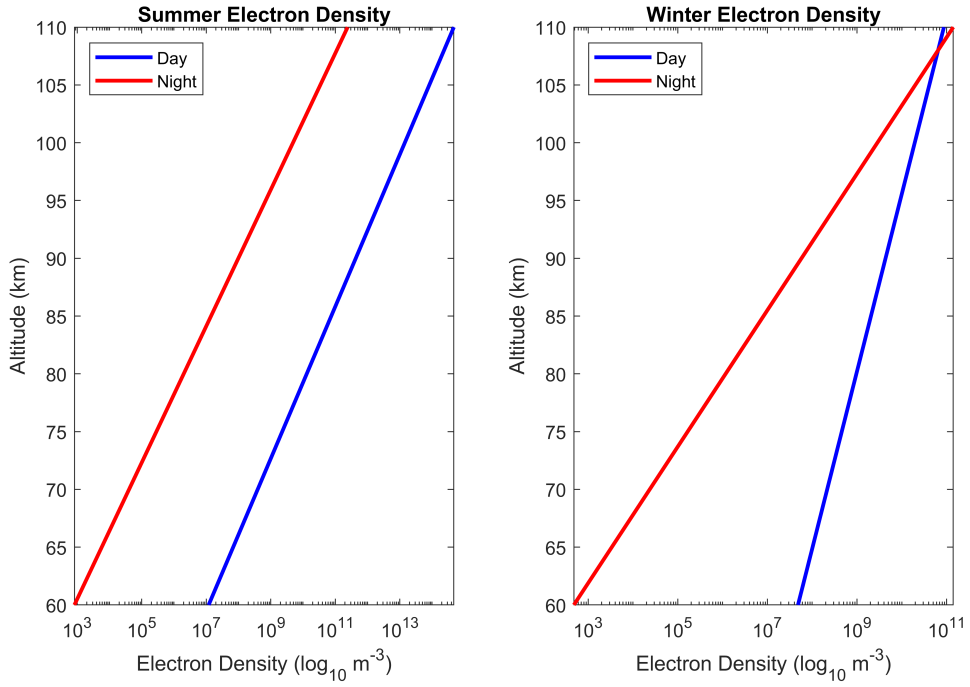

Figure 1.8: Seasonal and diurnal comparison of the middle latitude values of β and h' listed in Table 1.1.

The electron density of the D-region is known to vary diurnally, seasonally, with latitude. Table 1.1 shows a summary of typical types used for these different propagation situations for a 30 kHz wave. These values were derived from the extensive studies done by *Morfitt* [1977] and *Ferguson* [1980], which provide more generalized results for a range of frequencies. The waveguide parameter values in Table 1.1 are generalized estimates and ignore specific path variations, perturbations, or other geophysical phenomena. However, the table does highlight that the biggest difference between the parameters is between daytime and nighttime, which is expected since Lyman-α radiation is biggest source of ionization in the D-region and is only present during the day. The parameters vary more subtly when considering latitude and seasonality. The middle latitude values are plotted in Figure 1.8. The left panel shows the daytime electron density (blue) and nighttime electron density (red) for the summer. The right panel shows the winter daytime (blue) and nighttime (red) electron densities. Work done by later authors have tried to characterize waveguide parameters to account for different phenomena such as solar zenith angle [*Thomson*, 1993; *McRae and Thomson*, 2000; *Thomson et al.*, 2007], solar flares [*McRae and Thomson*, 2004; *Šulić*

et al., 2016a], and the day-night terminator [*Clilverd et al.*, 1999].

1.4.3 Electron-Neutral Collision Frequency

Like the electron density, the electron-neutral collision frequency is difficult to predict due to its dynamic nature. Two ways in which the electron-neutral collision frequency can be solved will be discussed. The first method was introduced by *Wait and Spies* [1964]. Wait used data from earlier electron-neutral collision frequency measurements from rocket based measurements [*Kane*, 1961] and partial reflection measurements [*Belrose and Burke*, 1964] to derive and validate an empirical model, Equation 1.4:

$$\nu_{en}(z) = 5 \cdot 10^6 e^{-0.15(z-70)} \approx 1.816 \cdot 10^{11} e^{-0.15z} \quad \text{collisions/sec}, \tag{1.4}$$

where z denotes the altitude in kilometers. This equation comes from a generalized form described in greater detail in *Thrane and Piggott* [1966]. However, in general, the Equation 1.4 is often treated as a constant since it is much less variable than the electron density profile, *Budden* [1985] and *Cummer et al.* [1998].

Table 1.2: Electron-neutral collision frequency equations for common D-region species as a function of altitude. Number densities are in units of cm^{-3}. Equations from *Schunk and Nagy* [2000].

Species	$\nu_{en}(z)$ in collisions/sec
N_2	$2.33 \cdot 10^{-11}[n_{N_2}(z)](1 - 1.21 \cdot 10^{-4} T_e) T_e$
O_2	$1.82 \cdot 10^{-10}[n_{O_2}(z)](1 + 3.6 \cdot 10^{-2} T_e^{1/2}) T_e^{1/2}$
O	$8.9 \cdot 10^{-11}[n_{O_2}(z)](1 + 5.7 \cdot 10^{-4} T_e) T_e^{1/2}$

The second method is based on the momentum transfer collision frequency equations derived from the Chapman-Cowling collision integral [*Chapman and Cowling* [1970]; *Schunk and Nagy* [2000]]. For this method, the collision frequency is solved for by using neutral density values of different ionospheric species in a moment transfer equation. Table 1.2 shows the equations needed to solve for the electron-neutral collision frequency of N_2, O_2, and O. In the equations in the table, $n_X(z)$ are the number densities of the respective species in cm^{-3} and T_e is the electron temperature (in Kelvin), both as a function of altitude in

kilometers. In the D-region, N_2 is the most abundant species, accounting for about 78% of the total particle concentration, and O_2 is the second most abundant species, serving as a "correction term", [*Thrane and Piggott*, 1966; *Nicolet and Aikin*, 1960]. The O species is shown as a third optional equation because at above about 85 km in the nighttime D-region it is thought to play a more important role, especially in regard to sporadic events, *Nicolet and Aikin* [1960]. The resulting collision frequency is a sum of the respective species used *Thrane and Piggott* [1966]. Neutral number densities can be retrieved from the *NRLMSISE-00* or similar empirical models, *Picone et al.* [2002], and used to solve the equations in Table 1.2.

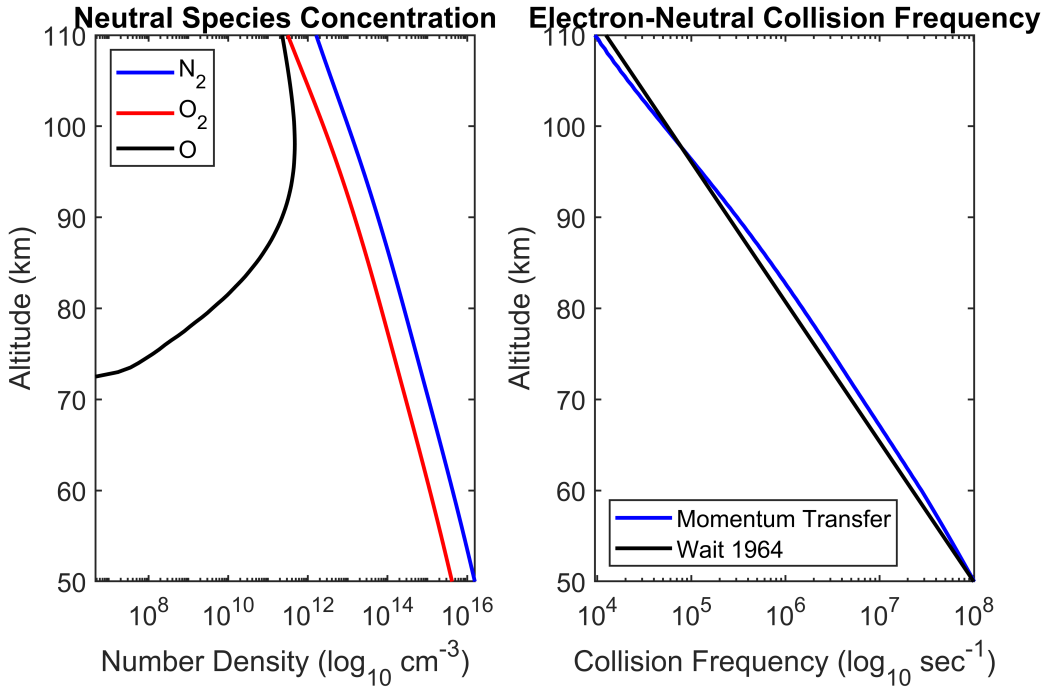

Figure 1.9: Comparison of VLF and LF/MF propagation in the "Earth-Ionosphere Waveguide".

1.4.4 LF/MF Propagation

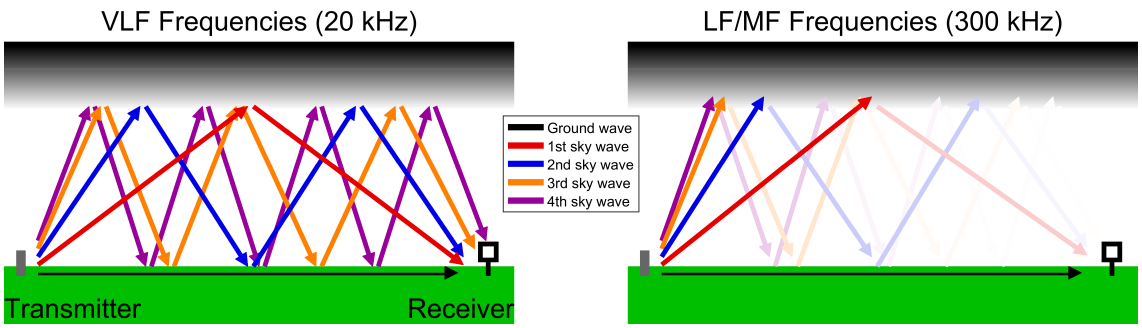

Figure 1.10: Comparison of VLF and LF/MF propagation in the "Earth-Ionosphere Waveguide".

The "Earth-Ionosphere Waveguide" is bounded by the Earth on the bottom and the ionosphere, a dispersive and anisotropic medium, on the top. The ground wave propagates along the surface of the Earth, guided by diffraction along the curvature of the earth. The skywaves reflect off the ionosphere and the Earth one or more times. A qualitative comparison between VLF and LF/MF waves is depicted in Figure 1.10. This propagation scheme is depicted for a VLF signal, left panel, and an LF/MF signal, right panel. As previously mentioned, ionospheric attenuation rates are much higher for LF/MF signals and is shown in the figure by the transparency of the arrows, [e.g. *Bickel*, 1957]. For this reason, LF/MF propagation generally only supports a small number of rays reaching the receiver, *Bickel* [1957], implying that, unlike VLF propagation, it may be possible to experimentally decompose a signal into its underlying components, and therefore directly infer the ionospheric characteristics. Experimental evidence to confirm this picture is shown in the next sections. In addition, the reflection of LF/MF signals is probably not at the same altitude as 20 kHz VLF signals. The reflection is thought to occur roughly at the altitude where $\omega = \omega_p^2/\nu$, where ω is the wave frequency, ω_p is the plasma frequency, and ν is the collision frequency. A first-order analysis using typical ionospheric profile indicates that 300 kHz waves reflect 10-15 km higher than 20 kHz signal for daytime hours, and 5-10 km higher during nighttime, as in Figure 1.11. So, although LF/MF signals still reflect within the D-region, they may access different altitudes. This will be discussed later.

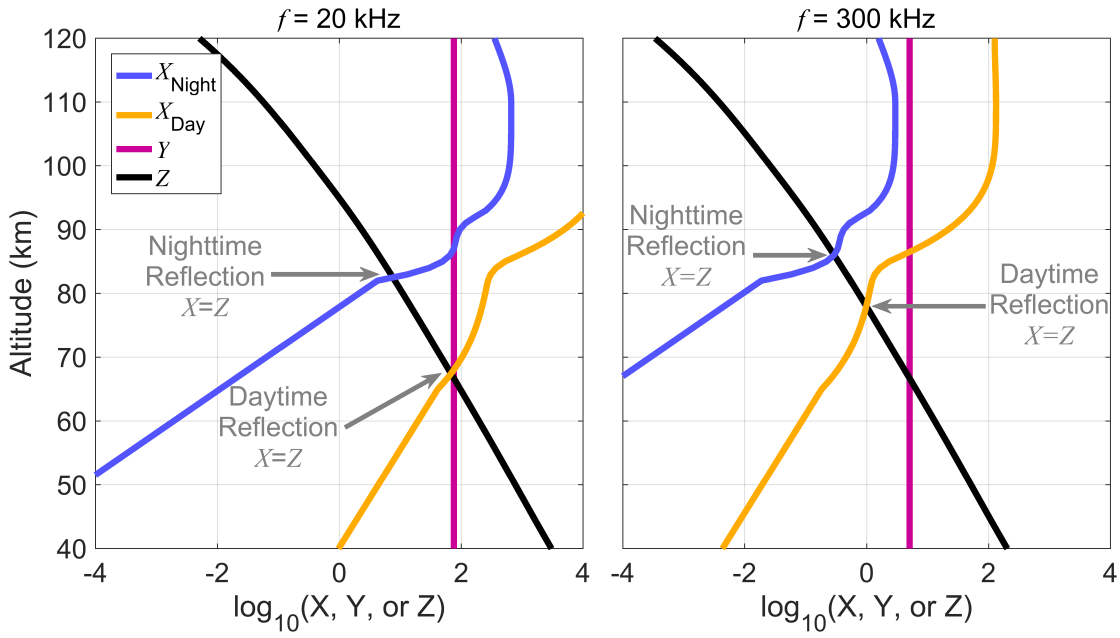

Figure 1.11: Comparison of approximate reflection heights for a 20 kHz wave (left) and a 300 kHz wave (right) using a typical ionospheric profile.

1.5 Current Remote Sensing Techniques

We now review the dominant techniques used to study the D-region. Some direct D-region diagnostics have been made, including rocket-based measurements, partial reflection technique, and incoherent scatter radar (ISR). These methods have a common problem: they are "spatial point" measurements, and, because of the weak reflections, require long time integrations to characterize the D-region. On the other hand, VLF or Sferic based techniques, which have high spatial and temporal resolution due to the low propagation losses, are very complicated to solve for electron density of the D-region. A more detailed overview of all these techniques can be found in *Sechrist* [1974].

1.5.1 Rocket Based Measurements

Two primary techniques exist for rocket-based measurements of D-region electron densities: 1) measuring the change in a propagating radio signal, 2) *in-situ* measurements of the electron densities.

The first technique was pioneered in the mid-20th century by *Seddon* [1953]. There

are many variations of this technique, but the general idea is that an upward traveling rocket measures the Faraday rotation and differential absorption of an HF or MF upward traveling wave. The waves consist of two linearly polarized components. As the components propagate upward, the polarization of the wave gradually becomes more elliptical. The ratio of the axes and the orientation of the ellipsoid describes the differential absorption and the Faraday rotation of the ionosphere, which can be used to determine the collision frequency, ν_{en}, and electron density, N_e, *Bennett et al.* [1972]. Conversely, the rocket may transmit the signal and a ground station could be used to measure the Faraday rotation. More information can be found from [e.g. *Seddon*, 1953; *Bennett et al.*, 1972; *Belrose et al.*, 1972]. In addition, multiple frequencies can be used to improve the accuracy of the measurement, [*Mechtly*, 1974].

The second technique for studying the D-region using rockets uses *in-situ* measurements. In this method, Langmuir probes are mounted on a rocket to measure positive and negative/electron currents and directly measure the electron density. However, due to the low number densities of the D-region, this method is often combined with the above method or other secondary method for calibration. More information on this method can be found in [e.g. *Reid*, 1970; *Røyrvik and Smith*, 1984; *Pfaff et al.*, 2001].

1.5.2 Partial Reflection Techniques

The partial reflection technique uses weak back-scatter of waves in the Medium Frequency (MF) and High Frequency (HF) ranges, about $1-6$ MHz, to measure the ratio of the ordinary and extraordinary amplitudes as a function of altitude to derive the collision frequency, ν_{en}, and electron density, N_e [*Belrose and Burke*, 1964; *Belrose*, 1970; *Hocking and Vincent*, 1982]. Using multiple frequencies, e.g. 2.66 MHz and 6.27 MHz such as in *Belrose and Burke* [1964], improves the accuracy of this technique.

1.5.3 Incoherent Scatter Radar

Incoherent scattering radar (ISR) technique utilizes a high-powered pulsed radio wave transmitted vertically upward and the received weak back-scatter to characterize the change in refractive index of the ionosphere, [e.g. *Sechrist*, 1974; *Mathews*, 1984]. ISR facilities in the

United States include the Haystack Observatory (Westford, MA), the Arecibo Observatory (Arecibo, Puerto Rico), and the Advanced Modular Incoherent Scatter Radar (AMISR) (Poker Flat, Alaska).

1.5.4 ELF/VLF Radio Waves

Utilization of Very Low Frequency (VLF, 3−30 kHz) radio waves has proven to be more useful for global, continuous D-region diagnostics. A ground-based radio receiver detects a signal from some distant source. Propagation in the "Earth-Ionosphere waveguide" allows signals to efficiently reach global distances [*Wait and Murphy*, 1956]. Changes in the signal with time are known to correspond to changes in the ionospheric conditions [*Barr et al.*, 2000; *Inan et al.*, 2010]. There are two chief sources of these signals: (1) one of a few dozen VLF transmitters typically operated by a navy for submarine communication [e.g. *McRae and Thomson*, 2000; *Thomson et al.*, 2007], or (2) the broadband radio atmospheric, or sferic, originating from lightning, [e.g. *Burton and Boardman*, 1933; *Cummer et al.*, 1998].

However, while the relatively low attenuation over very long distances makes VLF remote sensing useful on a large spatial scale, it also means the receiver signal is inherently "multi-mode", which makes inferring characteristics of the ionosphere difficult if using only experimental observations. The current method to connect VLF observations to ionospheric parameters is to utilize a forward modeling approach in which a propagation model is tweaked so that predictions match observations. This leads to a fundamental ambiguity that constrains VLF remote sensing from becoming a quantitative D-region measurement the way GPS TEC measurements are for the F-region. Recent work has utilized mini-arrays to analyze multipath propagation of low-frequency radio waves and map VLF lightning observations to provide a D-region diagnostic [e.g *Füllekrug et al.*, 2015b,a, 2016].

1.6 Past Work at LF/MF

Early studies examined the time variations in the skywave for LF signals around 100 kHz. *Bickel* [1957] examined a 135.6 kHz signal propagating over a 1,550 km path over the Pacific Ocean in Alaska. Assuming a homogeneous ionosphere over the propagation path and

that there are two dominant modes, a one-hop skywave and the groundwave, the author decomposed the nighttime phase interference pattern to estimate a reflection coefficient. The author found that daytime reflection coefficients were relatively low, between 0.003 to 0.032 for the frequency used, while the nighttime reflection coefficients were about an order of magnitude higher, about 0.074 to 0.26. *McKerrow* [1957] examined noise amplitudes at 107 kHz over a year to study diurnal and seasonal variations. The author found that the seasonal median variation at 107 kHz was 16 dB for the path-geometry used. *Belrose et al.* [1959] discussed LF propagation over short and long distances and, as in *Bickel* [1957], presented the case for 2-3 modes: 1) the groundwave, 2) the one-hop skywave, 3) the two-hop skywave. Amplitudes and reflection coefficients for signals at 100 kHz, 133.15 kHz, 135 kHz, and 191 kHz with paths from 813 km to 2420 km were analyzed for diurnal and seasonal variation. *McKerrow* [1960] provided a statistical analysis of the amplitude noise as a function of frequency, time of day, and season at multiple frequencies, including 135 kHz. This work found that: 1) higher frequencies are more sensitive to local "noise storms" (i.e. lightning storms), 2) the average amplitude decreased with frequency by about 1/f to $1/f^2$, among other interesting results. *Clarke* [1962] used amplitude-probability distributions of atmospheric noise in a power bandwidth of 370 Hz for 24 kHz, 135 kHz, 11 MHz, and 20 MHz to examine diurnal and seasonal variations of the noise power. Noise envelopes were derived and expressed in statistical terms. *Sprenger et al.* [1962] examined the absorption and apparent reflection height of signals between 125-1250 kHz for propagation paths between 45-450 km during a solar eclipse. This work found that the apparent reflection height varied by up to 5 km during the event. *Belrose and Thomas* [1968] studied the effects of geomagnetic storms on VLF, LF, and MF waves. Among other observations, the author found that LF waves had rapid fluctuations during the storm followed by increasing attenuation during recovery. Previous analysis of the skywave from NDGPS transmitters thus far has been limited to a radio engineering approach and focused on mitigating signal outages caused by fading (interference between the ground wave and skywaves), [e.g. *Last and Poppe*, 1996, 1997].

1.7 Past Work on Lower Ionospheric Roughness and Variability

A significant amount of work was done to investigate the physical scattering mechanism that produce D-region partial reflections, as it was previously not well understood. The work of *Rastogi and Holt* [1981], building on the previous work of *Tanenbaum et al.* [1973]; *Shapiro* [1973]; *von Biel* [1971]; *Newman and Ferraro* [1976]; *Mathews et al.* [1973], used a phenomenological model to explain HF scattering and weak partial reflections from the D-region. Three archetypes were used: 1) N_e contains only weak random fluctuations on a smooth background, 2) N_e contains weak random fluctuations and one plane horizontally extended region with a sharp gradient, 3) N_e contains weak fluctuations and several horizontal gradient structures. Observations of amplitude statistics made by the author found that this basic model explained some observations, but not all. Further work attempted to reconcile the different conclusions by research groups, *von Biel* [1981]; *Hocking* [1987], but the non-stationarity of the D-region proves to be problematic. Other research used spaced antennas with some success to determine the presence of "moving reflectors", *Lindner* [1975a,b].

Work done by *Lay and Shao* [2011a] and *Lay and Shao* [2011b], building on *Jacobson et al.* [2008], utilized the waveform of lightning strokes (sferics) detected by a network of receivers as a diagnostic of D-region roughness. The first two peaks in the sferic waveform are from the groundwave (direct path) and ionospheric reflection (skywave) respectively. Three critical assumptions made in this work was: 1) the first-hop skywave probes the middle of the propagation path, 2) the contribution to the skywave component is restricted to the region of the first Fresnel zone, and 3) the distance from the sferic source must be close enough to separate the groundwave and skywave ($\approx$<1000 km). An effective reflection height was found as the time delay between the groundwave and skywave. The reflection coefficient was found as the ratio between the skywave and groundwave (i.e. the sferic peaks). The studies measured the aforementioned metrics for several hours during a thunderstorm near Oklahoma and was able to detect interesting features in the D-region, such as an apparent "splitting" in the effective reflection height between "low frequencies" (<30 kHz) and "high frequencies" (30$-$60 kHz). The advantages of this technique are that:

1) the metrics are extracted directly from the sferic waveform which allows "direct" probing of the D-region variability, 2) during a thunderstorm, there is a multitude of probing sources available. However, the shortcomings of this method are that: 1) a nearby thunderstorm is needed as a source since the resolution (spatially and temporally) of this method decreases as the propagation distance increases since the Fresnel zone would increase in size and the delay between the modes would decrease until it becomes undetectable, 2) modeling is yet to be done to connected the measured metrics to D-region parameters, such as electron density. An alternative method proposed in *Han and Cummer* [2010] matches the frequency-domain spectrum of sferics to simulated spectra (using the Navy's Long Wave Propagation Capability (LWPC) code) to determine waveguide parameters of the D-region. The paper uses this method to study and discuss the spatial and temporal variability of the D-region over longer propagation distances.

Work done by *Füllekrug et al.* [2015b] utilizes a small aperture array of electric field sensors to study the variability in wave number vectors of a propagating signal using both VLF/LF transmitters, *Füllekrug et al.* [2014] and *Füllekrug et al.* [2015a], and sferics, *Füllekrug et al.* [2016]. Maps of electromagnetic noise maps are created by projecting the wave number plane onto a hemisphere by converting to spherical coordinates. In addition, the high time resolution of the electric field sensors was used to study frequency-dependent propagation effects in the D-region by resolving the frequency modulation of VLF transmitters, *Koh et al.* [2018]. The strengths of this method are the high angular resolution, on the order of 0.2° to 1.9°, and constant source, as opposed to sferics, enables the study of fine scale variability of a propagating wave over a long period of time. However, the shortcomings of this method are that many receivers are needed, e.g. ten are used in the papers cited.

1.8 Contributions

The following contributions are reported in this dissertation:

- We quantify the utility of NDGPS transmitters (285-325 kHz) for D-region remote sensing. It is shown that the skywave component of the signal from NDGPS trans-

mitters can be detected over a regional geography of ≈<2000 km at night and can interact with geophysical phenomena typically associated with the D-region.

- LF/MF propagation during the 2017 "Great American" solar eclipse is presented. Forward scattering and back scattering are detected and modeled. Wait and Spies waveguide parameters, h' and β, are estimated for the eclipse totality spot. The "settling rate" of the D-region is estimated from the back scattered signal.

- A new method of characterizing D-region roughness is presented. The roughness is segmented into 1) horizontal roughness, 2) vertical roughness. The horizontal roughness is measured using *correlation length scales*. The vertical roughness is measured using *differential phase height*.

- A technique for connecting roughness metrics to ionospheric parameters is also presented. A Monte Carlo Method (MCM) is used, which runs many iterations of an FDTD code seeded with randomly varying D-regions of different degrees of roughness. Simulated correlation length scales are compared to observed correlation length scales.

1.8.1 Journal Publications

- Higginson-Rollins, M. A., and M. B. Cohen (2020), Studying the Effects of the August 2017 Solar Eclipse using LF/MF Signals of Opportunity, manuscript in preparation for submission to *Geophysical Research Letters*.
- Higginson-Rollins, M. A., and M. B. Cohen (2020), Characterizing D-Region Roughness Using LF/MF Signals of Opportunity, manuscript in preparation for submission to *Journal of Geophysical Research*.
- Cohen, M. B., R. K. Said, E. W. Paschal, J. C. McCormick, N. C. Gross, L. Thompson, M. Higginson-Rollins, U. S. Inan, and J. Chang (2018b), Broadband longwave radio remote sensing instrumentation, *Review of Scientific Instruments*, *89*(9), 094,501, doi: 10.1063/1.5041419
- Cohen, M. B., N. C. Gross, M. A. Higginson-Rollins, R. A. Marshall, M. Gołkowski, W. Liles, D. Rodriguez, and J. Rockway (2018a), The Lower Ionospheric VLF/LF Response to the 2017 Great American Solar Eclipse Observed Across the Continent, *Geophysical Research Letters*, *45*(8), 3348–3355, doi: 10.1002/2018GL077351

- Higginson-Rollins, M. A., and M. B. Cohen (2017), Exploiting LF/MF signals of opportunity for lower ionospheric remote sensing, *Geophysical Research Letters*, *44*(16), 8665–8671, doi: 10.1002/2017GL074236

1.8.2 Conference Presentations

- Higginson-Rollins, M. A., and M. B. Cohen (2019), Characterizing D-Region Roughness using LF/MF Signals of Opportunity, Poster Presentation at the 2019 AGU Fall Meeting; paper SA51C-3174; San Francisco, CA; July 8-18.

- Higginson-Rollins, M. A., and M. B. Cohen (2019), Characterizing D-Region Roughness using LF/MF Signals of Opportunity, Oral Presentation at the 27th IUGG General Assembly; paper IUGG19-3070 JA04; Montreal, Canada; July 8-18.

- Higginson-Rollins, M. A., and M. B. Cohen (2017), LF/MF Propagation Modeling for D-Region Ionospheric Remote Sensing, Poster Presentation at the 2017 AGU Fall Meeting; paper SA43A-2644; New Orleans, LA; December 11-15.

- Higginson-Rollins, M. A., and M. B. Cohen (2017), D-Region Ionospheric Remote Sensing with LF/MF Signals of Opportunity, Oral Presentation at the 2017 URSI-GASS Meeting; paper HGE18-1; Montreal, Canada; August 19-26.

- Higginson-Rollins, M. A., and M. B. Cohen (2017), D-Region Ionospheric Remote Sensing Using LF/MF Signals of Opportunity, Oral Presentation at the 2017 URSI-NRSM Meeting; paper G2-2; Boulder, CO; January 4-7.

- Higginson-Rollins, M. A., and M. B. Cohen (2016), LF/MF D-Region Ionospheric Remote Sensing, Poster Presentation at the 2016 AGU Fall Meeting; San Francisco, CA; paper SA41A-2358; December 12-16.

- Cohen, M.B., Golkowski, M., and M. A. Higginson-Rollins (2016), VLF/LF Transmitters for Diagnostics of the Ionosphere, Oral Presentation at 2016 VERSIM-RBS; Hermanus, South Africa; September 19-24.

- Higginson-Rollins, M. A., and M. B. Cohen (2016), Diurnal Variation of LF Transmitter Signals at Many Locations, Poster Presentation at 2016 CEDAR-GEM Workshop; Santa Fe, NM; paper ITIT-05; June 19-24.

- Higginson-Rollins, M. A., and M. B. Cohen (2015), Ambient VLF Transmitter Variation Detected at Many Locations, Poster Presentation at 2015 AGU Fall Meeting; San Francisco, CA; paper SA51A-2389; December 14-18.

CHAPTER 2
REMOTE SENSING WITH NDGPS TRANSMITTERS

2.1 Data Interpretation

2.1.1 LF AWESOME Receiver Data

The data collected from the receiver is in a broadband form with 1 MHz sampling frequency from two channels: North/South (N/S) and East/West (E/W) channel. Transmitters, such as naval VLF transmitters and NDGPS transmitters, utilize a minimum-shift keying (MSK) modulation with a 100 or 200 baud rate (bits-per-second). In MSK, bits are encoded by varying the carrier frequency by a quarter of the baud rate. A synchronized MSK demodulation, [*Gross et al.*, 2018], is then applied to this data, which generates a quasi-continuous wave (CW) signal. The result is that the horizontal magnetic flux density of a narrowband transmitter can be represented by the amplitude and (carrier) phase of the N/S and E/W channel. Figure 2.1 depicts this output from a NDGPS transmitter located in English Turn, Louisiana, [29.8783° N, -89.9417° W] detected by a receiver in Baxley, Georgia, [31.8767° N, 82.3621° W] at a frequency of 293 kHz. The top panel of the figure shows the amplitude of the horizontal magnetic flux density in units of decibels of pico-Tesla (dB-pT) for both channels. The diurnal trend seen in the amplitude will be discussed in more detail later, but, other than the 3-dB offset, the two channel amplitudes track each other very closely. This is due to the orientation of the antenna in regard to the propagation path of the signal from the transmitter, which is predominately in the east-west direction. The bottom panel shows the phase in degrees for both channels. The phase has been "unwrapped" with a threshold of 180°. In contrast to more stable VLF transmitters, which have a stable phase that track diurnal/solar conditions during the day, the phase from NDGPS transmitters suffer from clock frequency instability. This presents itself has "ramping" in the unwrapped phase, as seen in Figure 2.1, or as "random jumps" between -180° and 180° without unwrapping, as seen in Figure 2.2. Figure 2.2 shows a

2-minute subset of the wrapped phase data. The "saw tooth" pattern emerges due to the phase exceeding 180° and jumping down to -180°. The unwrapping threshold value can be adjusted to resolve the saw tooth pattern, but there is a contention between using too low of a value and possibly losing information or using too large of a value and not fully resolving the problem. Figure 2.2 shows that the clipping in phase occurs occasionally a little below ±180, so the threshold could be reduced. Figure 2.3 shows the same example phase shown in the previous two figures, but with varying unwrapping thresholds. Note the drastic change in the shape of the curve between the top left and bottom right panels. The two channel phase lines track each other in both plots, but the shape and magnitudes (left axis) are drastically different.

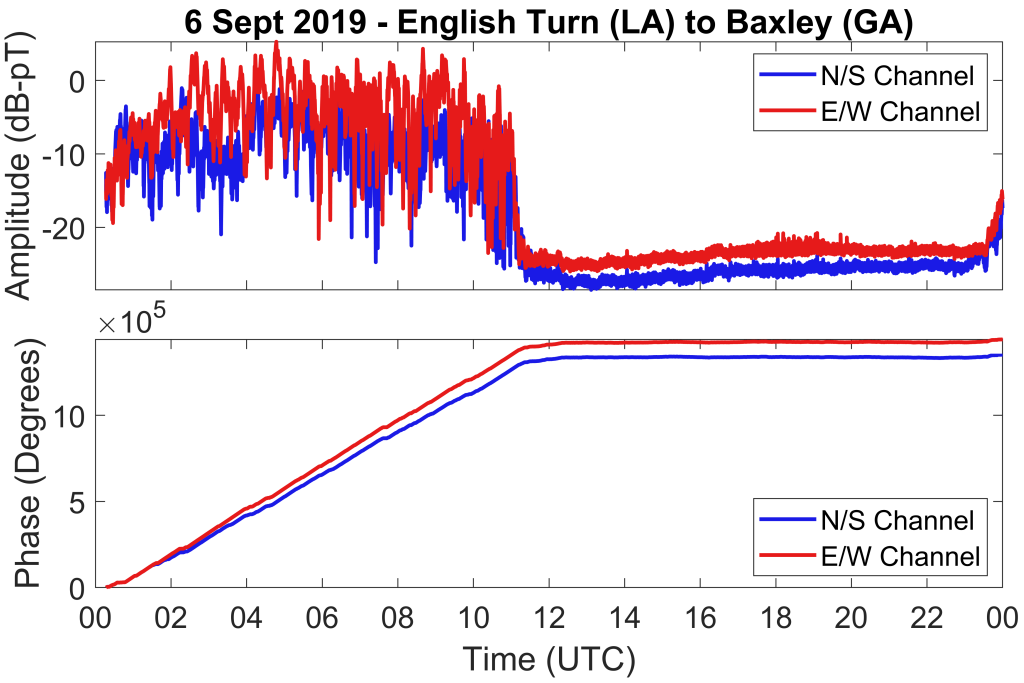

Figure 2.1: Example raw output from a synchronized MSK demodulation on a NDGPS narrowband signal.

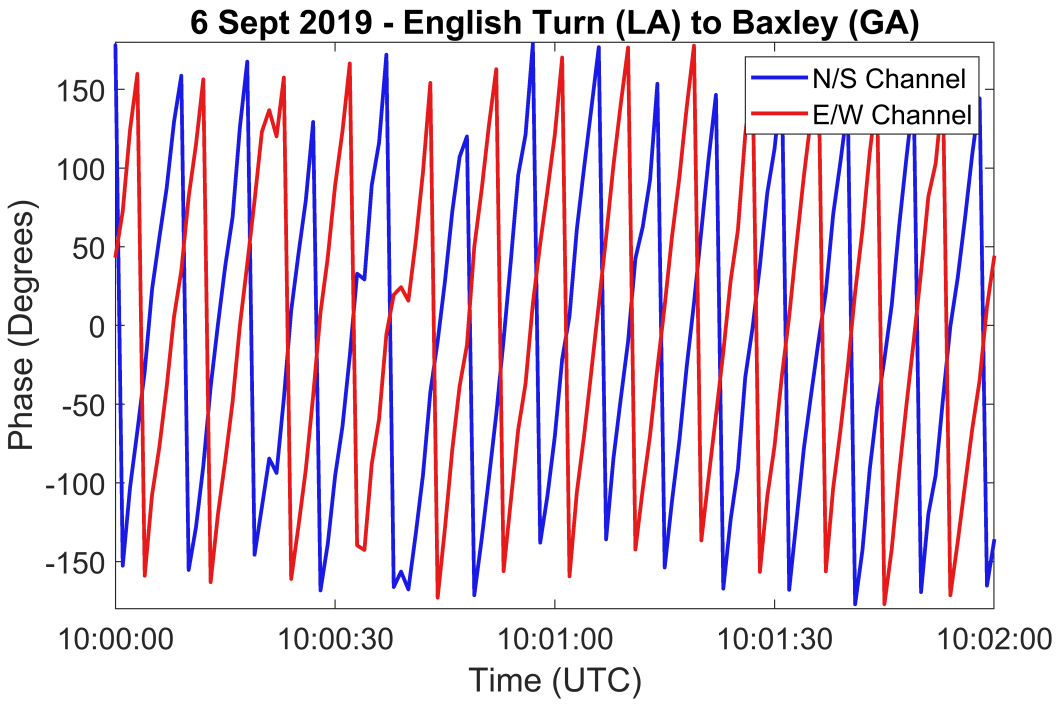

Figure 2.2: Example the wrapped phase detected from an NDGPS transmitter.

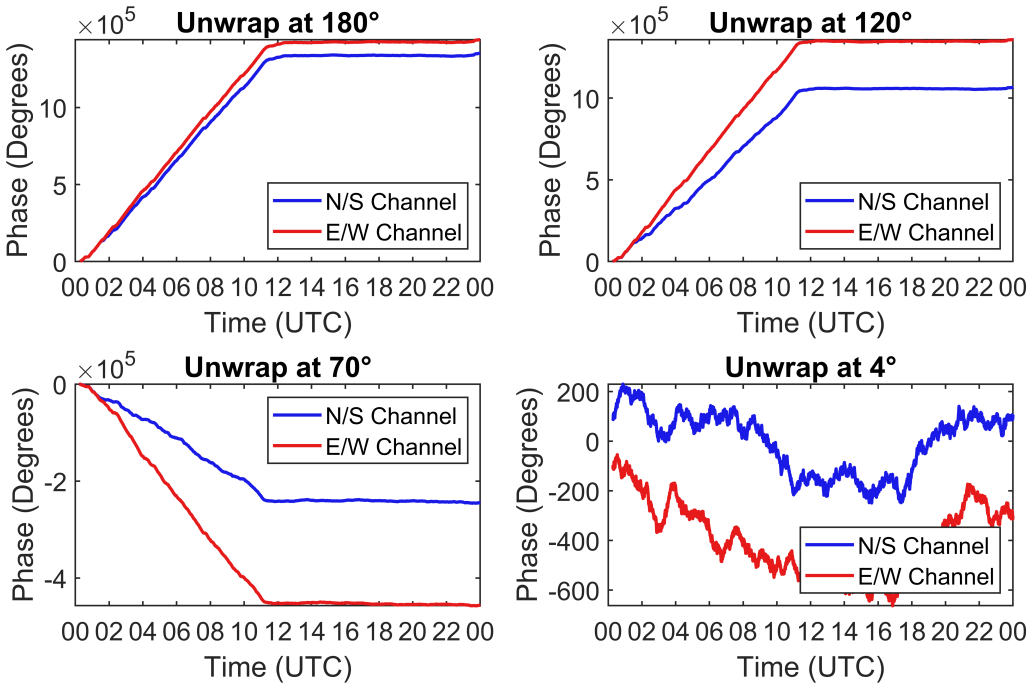

Figure 2.3: The example phase for the North-South and East-West channels with varying unwrapping thresholds.

2.1.2 Polarization Ellipse

The four expected values, amplitude and phase of each of the two channels, can be written as two separate complex phasors that define an ellipse centered at the origin. Figure 2.4 shows this polarization ellipse. Useful metrics can be derived from the resulting ellipse and are shown in this figure. Major axis length and minor axis length correspond to longer radius and shorter radius of the ellipse respectively. The nominal angle of arrival from the source, denoted as Θ_{az}, is the clockwise rotation sense between the northward direction and the transmitter direction derived using a clockwise rotation matrix. The tile angle, denoted as τ, is the difference between the major axis direction and the azimuthal direction (as defined by $\hat{\phi}$). This metric has a range of $-90^\circ \leq \tau \leq 90^\circ$. The ellipticity angle, χ, describes how linear/circular and the rotational sense of the ellipse. This metric ranges from $-45^\circ \leq \chi \leq 45^\circ$. The start phase is equal to the phase difference between the vector parallel to the major axis and the initial point of magnetic flux density. This metric captures the transmitter phase change and is independent of the geometric shape of the ellipse. Synchronized MSK demodulation and the polarization ellipse method are both covered in great detail by *Gross et al.* [2018].

The main benefit of using the polarization ellipse method is that it converts an arbitrary orientation to values with physical meaning (e.g. the major axis length corresponds to the transverse magnetic (TM) mode and the minor axis length corresponds to the transverse electric (TE) mode). The work in this thesis will primarily focus on the major axis length and the minor axis length. These parameters correspond to the transverse magnetic (TM) and transverse electric (TE) modes of the magnetic field respectively. The start phase will also be used to derive a metric discussed in a later section.

2.2 Observations

2.2.1 Propagation Distance

Figure 2.5 demonstrates the long range signal detection of the LF receivers for NDGPS signals. The green dots represent the locations of the NDGPS transmitters as of April 2016, and the blue star is the location of the receiver at PARI (North Carolina) [35.1996° N,

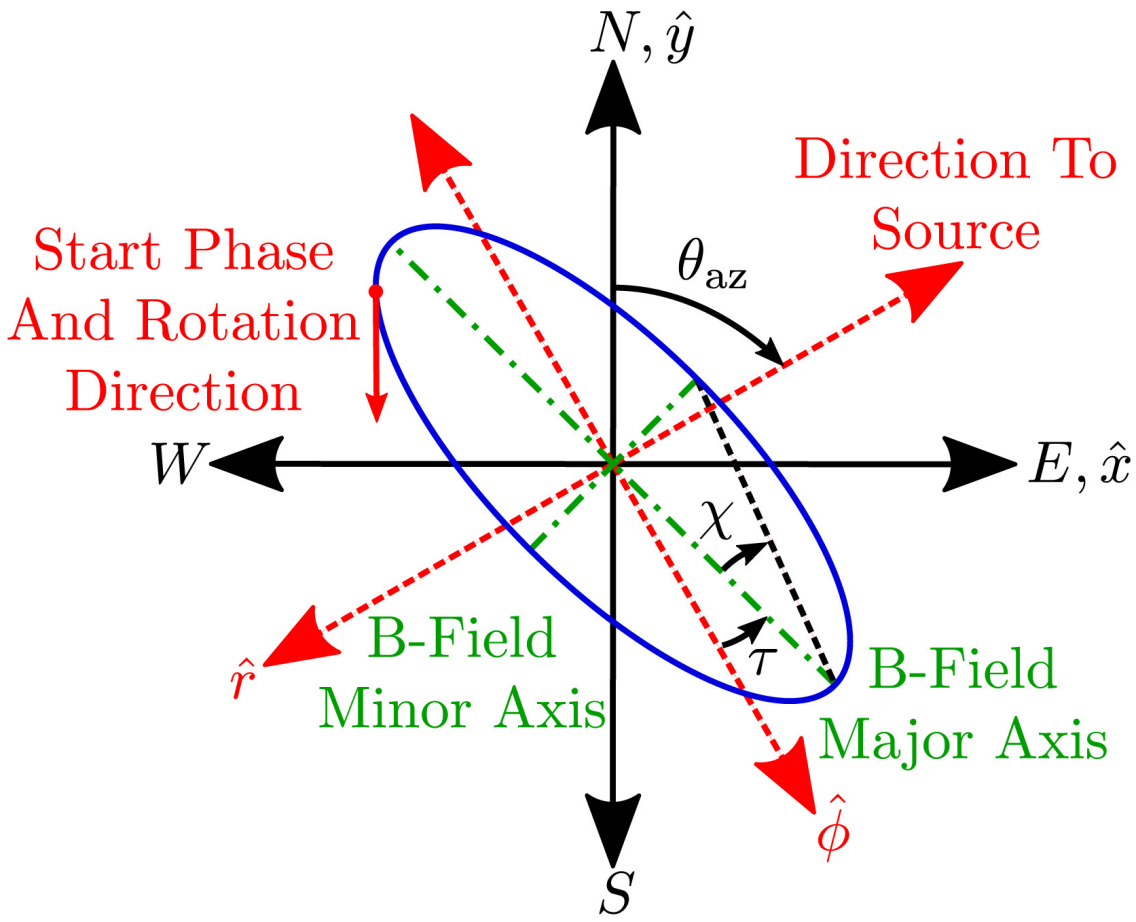

Figure 2.4: Measures derived from a "polarization ellipse", from *Gross et al.* [2018]

82.8718° W]. The right panel shows one minute of calibrated magnetic field data, integrated and presented as a frequency spectrum. The detected signal is a mix of spread-spectrum and coherent Minimum-Shift Keyed (MSK) signals, since the transmitted bits are not necessarily randomized. From examining the SNR of many transmitters, we ascertain that our receivers have a daytime range of approximately 750 km, as shown by the orange shading circle on the map, and a nighttime range of approximately 2400 km, as shown by the blue shading circle on the map, although there is some variation based on the type of antennas used by NDGPS sites. The bottom left inlaid panel shows an example of the analysis used to determine the detection range. The black dots represent the approximate amplitude of some observed transmitters. The red line represents the noise floor for this site and the blue dashed line is a linear fit to the transmitter amplitudes, where the two lines intersect is the approximate range. The red path in the map shows one signal, transmitted at 310

kHz from Whitney (Nebraska), nearly 2000 km away from PARI. As seen in the thumbnail in the right panel, the Whitney transmission is detected at PARI with ∼20 dB SNR. From this, we can establish that LF/MF waves can be used for ionospheric characterization over very large regions, unlike single-point techniques like rockets, HF partial reflections, and incoherent scatter radar.

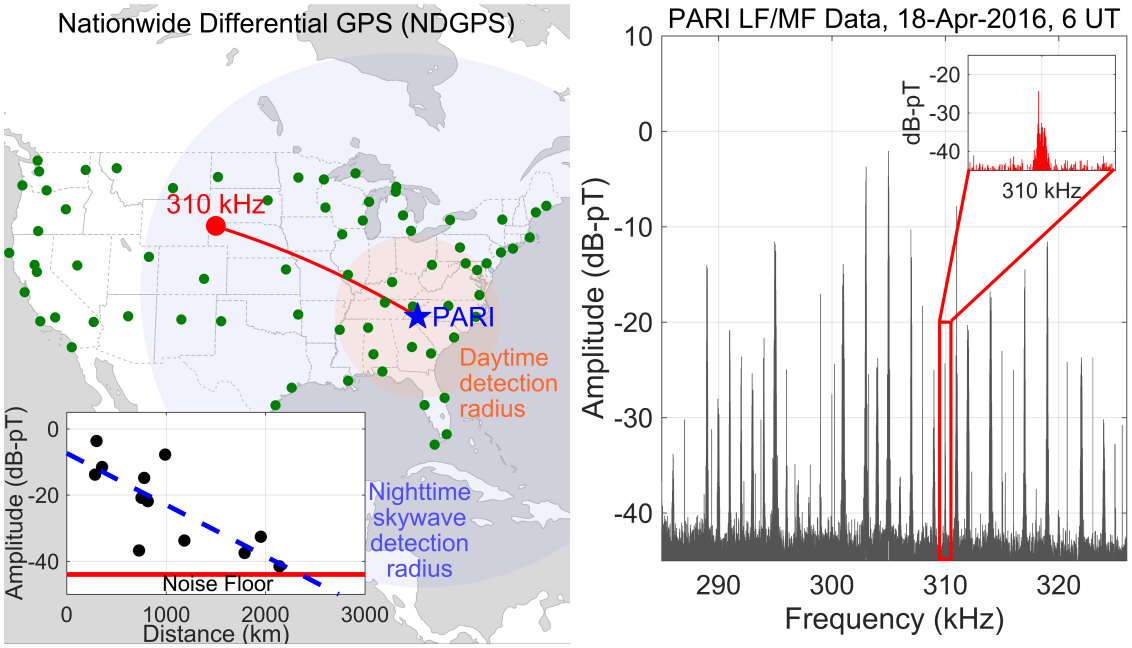

Figure 2.5: Estimated LF/MF detection radius for the LF AWESOME Receiver located at the Pisgah Astronomical Research Institute (PARI) in North Carolina. Figure adapted from *Higginson-Rollins and Cohen* [2017]

2.2.2 Diurnal Variations of the Skywave

As previously mentioned, the daytime D-region electron densities are subject to diurnal, seasonal, and solar-cycle variation, and are thus highly stable and predictable apart from during transient events. These time variations in the skywave for LF signals around 100 kHz are well documented in early studies [e.g. *Bickel*, 1957; *Belrose et al.*, 1959; *McKerrow*, 1960; *Clarke*, 1962]. However, for the LF/MF signals from NDGPS transmitters to be utilized as a diagnostic tool for the D-region of the ionosphere, the skywave component of the signal must be detectable by our receiver. The diurnal trend offers perhaps the easiest way to assess this for a given transmitter-to-receiver path. For example, Figure 2.6 shows

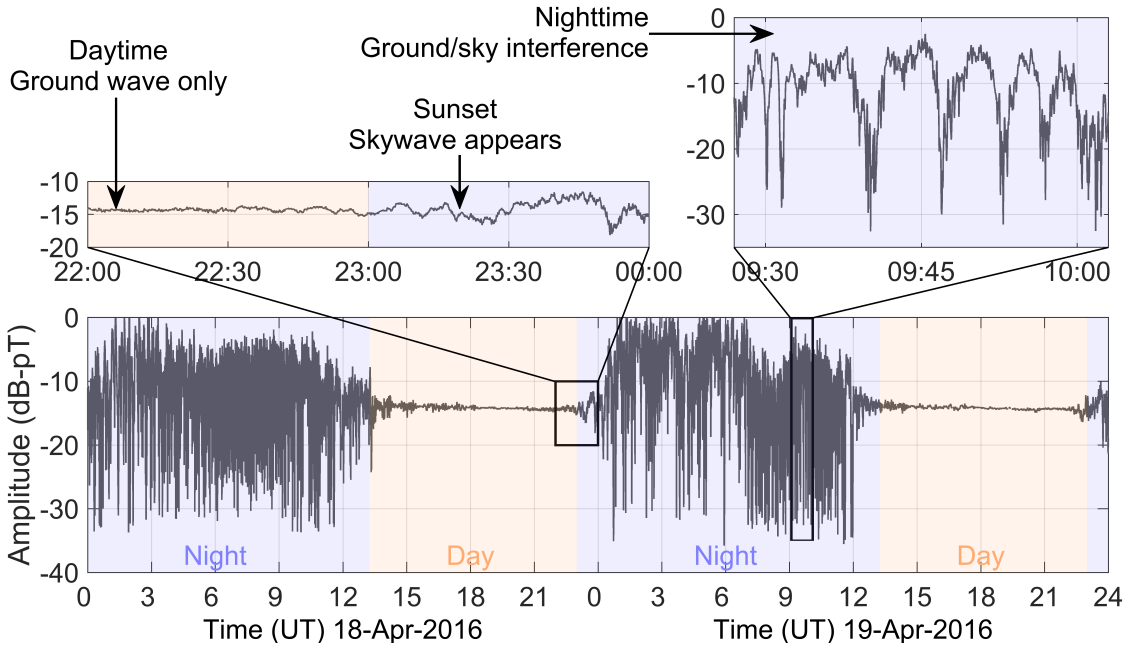

Figure 2.6: Observed diurnal variation of the signal from a NDGPS transmitter. Adapted from *Higginson-Rollins and Cohen* [2017].

48 hours of narrowband data collected by the LF AWESOME receiver located at PARI from the transmitter in Dandridge, Tennessee, located 99 km away from the receiver. The diurnal variation apparent in Figure 2.6 is consistent with other observations, such as *Last and Poppe* [1997]; *Bickel* [1957]. The bottom panel of the figure shows the full 48-hours of amplitude data, with the nighttime and daytime period labeled. The daytime data is very nearly constant with time. As the skywave is heavily attenuated during the day due to a significantly higher collision frequency, the reflection coefficient is approximately two to three orders of magnitude lower *Bickel* [1957], hence the daytime signal for this particular transmitter-receiver link is dominated by the ground wave, which does not change with time. However, as the top left panel shows, as the sun sets the attenuation of the skywave decreases and a fading pattern appears. The steadily intensifying oscillations result from phase interference caused by constructive and destructive interference between the ground wave and the steadily strengthening (and phase-varying) skywave. The top right panel shows the interference pattern in the deep nighttime hours. It is evident that at night the signal is highly variable with approximately a 30-dB variation in the amplitude of the depicted signal. This type of fading pattern is consistent with a small number of

components, likely one skywave and one ground wave, since many rays are unlikely to produce such perfect cancellation as often as observed in this 48-hour period at nighttime. Since there appears to be only two dominant components to the nighttime signal, it is in principle possible to mathematically separate the two components using the amplitude and phase of the transmitter signal at the receiver. Extracting the phase requires demodulation of the minimum-shift-key modulation imposed on the NDGPS beacons and a coherent and phase-stable source or a method of mitigating source-phase instabilities.

2.2.3 Seasonal Variations of the Skywave

The D-region of the ionosphere, as discussed in Section 1.4, is strongly influenced by solar effects. Section 2.2.2 discusses the diurnal effect of the Sun on the D-region – as the sunrises and sets, the ionization in the D-region increases during the day and decreases at night. In addition to this diurnal variation there is also a seasonal variation in the D-region, *Šulić et al.* [2016b]. This is most readily observed by the changing length of days throughout the year. Figure 2.7 and Figure 2.8 show this change in the length of day for two different paths. In both figures, the top panel is the N/S channel amplitude and the bottom panel is the E/W channel amplitude. The color reflects the amplitude in units of decibel dB-pT, where blue is lower and yellow is higher. Effectively, this means that daytime is blue, and nighttime is yellow. The vertical axis is the UTC hour during each day and the horizontal axis is the day of the year, starting with January 1 and ending in December 31. The data for both figures is for 2018. Figure 2.7 is for a predominantly east-west path, so the change in the length of day is more subtle and visible as the slight curve in the daytime starting at around 12 UTC rising to about 10 UTC and then returning back to 12 UTC. This trend occurs during summer, where days grow longer and so the blue area, i.e. daytime, grows and shrinks as summer passes. Figure 2.8 shows the same data but for a predominantly north-south path. However, this figure also shows the effect of winter, i.e. the days getting significantly shorter, as seen in the months of January to April by the yellow area (nighttime) growing.

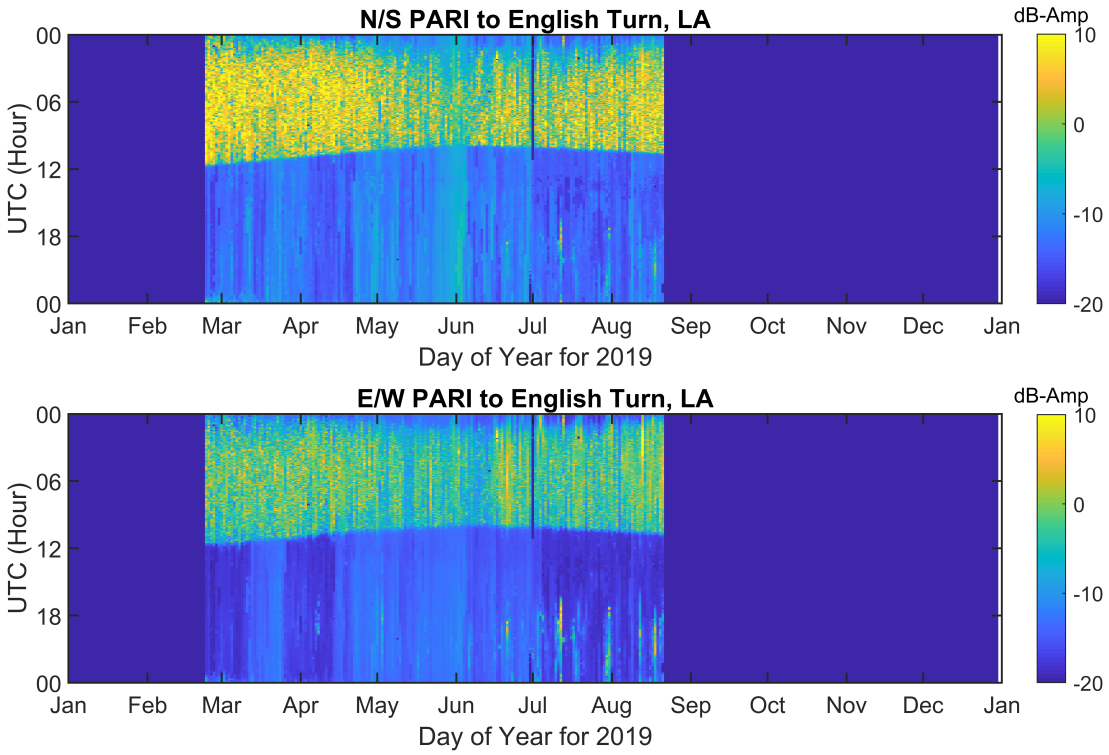

Figure 2.7: Amplitude, in dB-pT, of the N/S and E/W channels of the PARI receiver examining an NDGPS transmitter in English Turn, Louisiana, with a frequency of 293 kHz over the course of several months.

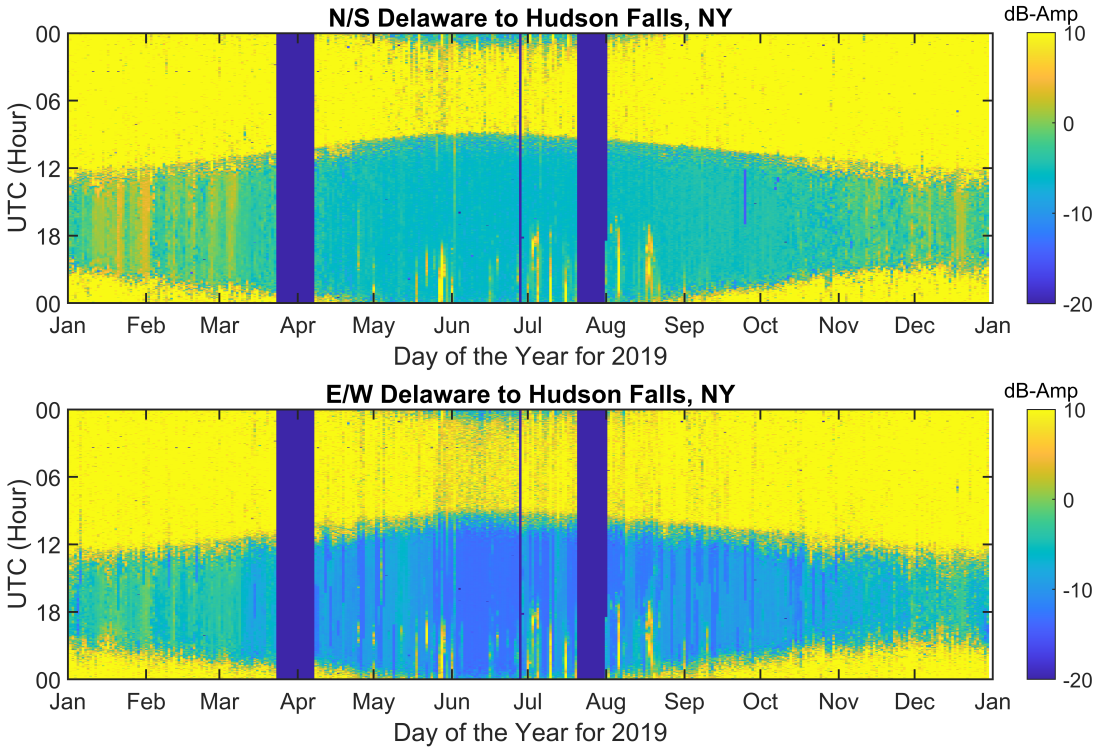

Figure 2.8: Amplitude, in dB-pT, of the N/S and E/W channels of the Delaware receiver examining an NDGPS transmitter in Hudson Falls, New York, with a frequency of 324 kHz over the course of several months.

2.2.4 Early/Fast Events

"Early/Fast" events are prompt onset (< 20 ms) nighttime D-region perturbations that occur simultaneously (< 20 ms) to a lightning discharge in a localized vicinity and typically recover in about 10s to 100s of seconds *Johnson et al.* [1999] and have been the subject of an abundance of research [e.g. *Inan et al.*, 1996a,b, 2010, and references therein]. Using Vaisala's National Lightning Detection Network (NLDN) *Cummins and Murphy* [2009], we were able to detect all lightning strokes that occurred near the great circle path of a receiver in Baxley (Georgia) and the NDGPS transmitter in New Bern (North Carolina). Figure 2.9 shows the amplitude data from one channel at the Baxley receiver. The data has the characteristic features of an "Early/Fast" event: a very sudden onset and a much more gradual recovery. In this case, a positive cloud-to-ground lightning stroke with peak current 98 kA occurred within 18 km of the New Bern, North Carolina, to Baxley, Georgia,

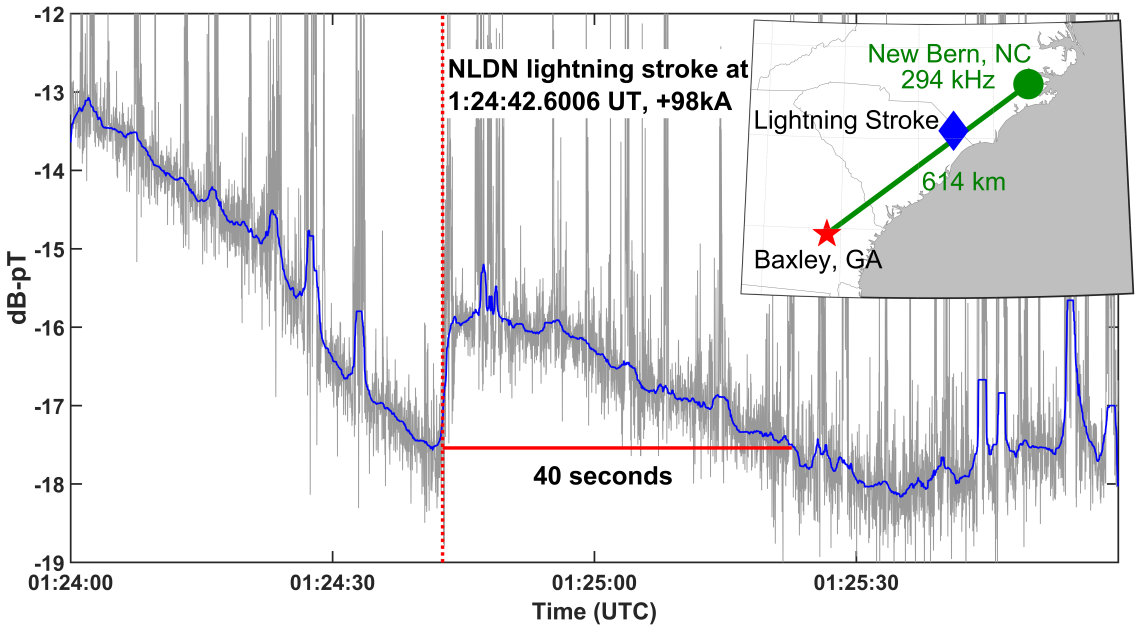

Figure 2.9: Detected Early/Fast event coinciding with a lightning stroke over South Carolina. Adapted from *Higginson-Rollins and Cohen* [2017].

path, near the midpoint of the path. When observed with VLF transmitter-receiver paths, Early/fast events typically occur when the causative lightning is within 50−200 km of the path *Johnson et al.* [1999]; *Salut et al.* [2013]. This is one of a few Early/Fast events observed on this path and day alone and demonstrates potential usefulness of LF/MF signals from NDGPS transmitters as a diagnostic tool for geophysical phenomena associated with the D-region of the ionosphere. LF/MF waves interact with the ionosphere differently than VLF waves, such as reflecting at higher altitudes, and future work will focus on examining Early/Fast events at these frequencies.

CHAPTER 3
MODELING LF/MF WAVES

3.1 Numerical Modeling Methods

This section will briefly discuss two different methods for modeling LF/MF propagation in the Earth-Ionosphere waveguide: 1) the full-wave method (FWM) and 2) the finite-difference time-domain (FDTD) method. The descriptions here are by no means exhaustive, but rather serve to summarize their implementation and application to the research outlined in this thesis.

3.1.1 The Full-Wave Method

The full-wave method (FWM) has been extensively used in literature to study Very-Low Frequency (VLF; 3-30 kHz) wave propagation *Budden* [1955a], *Budden* [1955b], *Lehtinen and Inan* [2008], *Lehtinen and Inan* [2009], *Lehtinen et al.* [2010], and *Cohen et al.* [2012]. Very generally, the FWM first stratifies the ionosphere into horizontal slabs. The thickness of the slabs is dependent on the frequency of interest where a general rule of thumb could be a thickness of $\approx 1/10\lambda$, where λ is the wavelength. Next, the susceptibility matrix ($\mathbf{M}$) and wave components (H_x, H_y, E_x, E_y) are solved simultaneously for all slabs. Then, starting at an altitude past the reflection point of the wave where only the two up going waves are propagating and a unique solution exists, a downward integration is done on the wave components until reaching below the bottom boundary of the ionosphere where the reflection coefficients are calculated. The reflection coefficient matrix, as in Figure 3.1, is a two by two matrix that defines the reflection of the transverse magnetic (TM), transverse electric (TE), and mode coupling components. Moving clockwise and starting at the top left position, the reflection coefficients are ${}_{||}R_{||}$, ${}_{||}R_{\perp}$, ${}_{\perp}R_{||}$, and ${}_{\perp}R_{\perp}$, where "TM" is the parallel ($||$) and "TE" is the perpendicular ($\perp$)). The mode coupling terms are the off diagonal elements. The presence of a magnetic field in the D-region makes it anisotropic and causes some of the TM wave to couple into the TE component and vice versa.

$$\underline{\underline{R}} = \begin{pmatrix} {}_{\parallel}R_{\parallel} & {}_{\parallel}R_{\perp} \\ {}_{\perp}R_{\parallel} & {}_{\perp}R_{\perp} \end{pmatrix}$$

Figure 3.1: A typical 2 by 2 reflection coefficient matrix that defines reflection from an anistropic media.

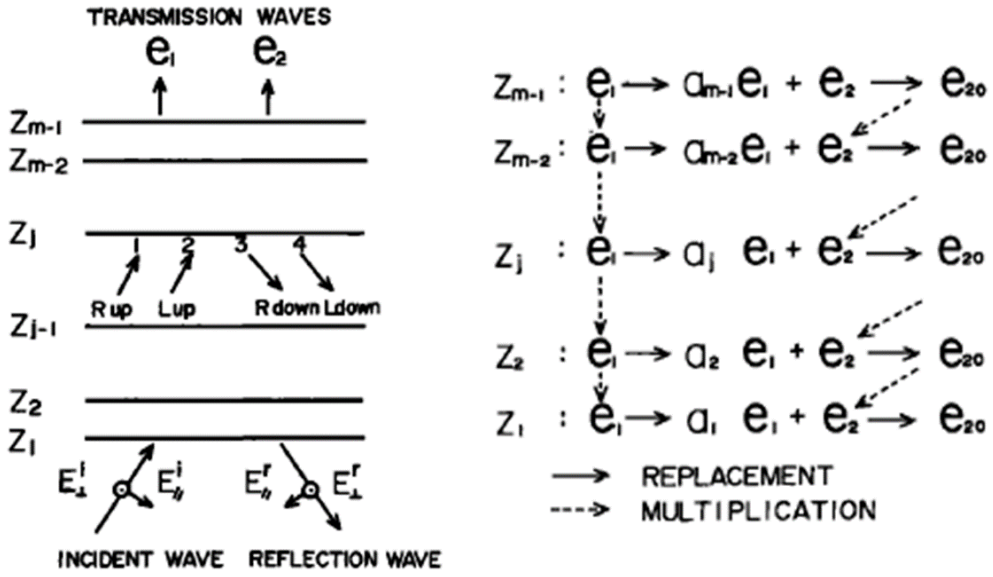

Figure 3.2: The left panel shows the discretization scheme of an Full Wave Model used to study the D-region. The right panel shows the downward integration scheme used. Note that e_1 and e_2 show the upward and downward wave components and a_n is an orthogonalization factor used to mitigate numerical "swamping". Figure adapted from *Nagano et al.* [1975].

This process is illustrated in Figure 3.2. The left panel shows the discretization of the D-region. Each slab is denoted as "z_n". Within each slab there exists an up-going (e_1) and down-going (e_2) component. The variables in the left panel correspond to those in the right panel. The right panel shows the downward integration scheme, where e_{20} is a scaled value. In general, there are many different integration schemes that can be used, typically the 4th order *Runge-Kutta* integration (RK4), e.g. *Budden* [1955a]. Earlier works dealing with the full-wave solution were heavily limited due to the numerical instability of the evanescent wave, known as "numerical swamping". The large imaginary component of the vertical wave number would swamp the waves of interest because effectively a small

number would be added to a very large number. Early works attempted to mitigate this problem [e.g. *Pitteway* [1959] and *Nagano et al.* [1975]]. In the case of the right panel of Figure 3.2, there is the addition of a orthogonalization coefficient, a_n. This coefficient is the result of the *Gram-Schmidth Orthogonalization* and is used to prevent the transfer of error from e_1 to e_{20} and prevent swamping. This is allowable since any linear combination of solutions for the linear equations is a solution, *Nagano et al.* [1975]. In contrast, the method used by *Lehtinen et al.* [2010], and previous works, uses a recursive calculation for both the reflection coefficients and wave amplitudes, where the direction of recursion is important in providing stability against numerical swamping. Code from Nikolai Lehtinen, which uses this method, was used for this research [*Lehtinen et al.*, 2010].

Lehtinen's FWM was ran for a North-South propagating wave at 300 kHz for daytime and nighttime conditions. The daytime data is shown in Figure 3.3. The figure shows the absolute value of the reflection coefficient on the y-axis and the angle of incidence in degrees, Θ, on the x-axis. Each line is an element from the reflection coefficient matrix, see Figure 3.1. Three typical features which are expected are that: 1) at $\Theta = 0°$, the absolute value of each reflection coefficient is equal, 2) as Θ approaches 90°, ${}_{||}R_{||}$ and ${}_{\perp}R_{\perp}$ approach 1, and 3) as Θ approaches 90°, ${}_{||}R_{\perp}$ and ${}_{||}R_{\perp}$ approach 0. These characteristics are also seen in Figure 3.4 and are typical for low frequency waves, which have reflections, in the Earth-Ionosphere Waveguide. For NDGPS signals propagating, the dominant reflection coefficient that drives the amplitude of the first skywave is ${}_{||}R_{||}$. Between Figure 3.3 and Figure 3.4, there is a significant difference in ${}_{||}R_{||}$. Between $\Theta = 40°$ and $\Theta = 70°$ there is a difference in $|{}_{||}R_{||}|$ of ≈ 0.5 or a factor of $\approx 10\times$. This difference between the daytime and nighttime skywave reflection coefficient is in line with literature, such as the analysis done by *Bickel* [1957] for a 135.6 kHz wave.

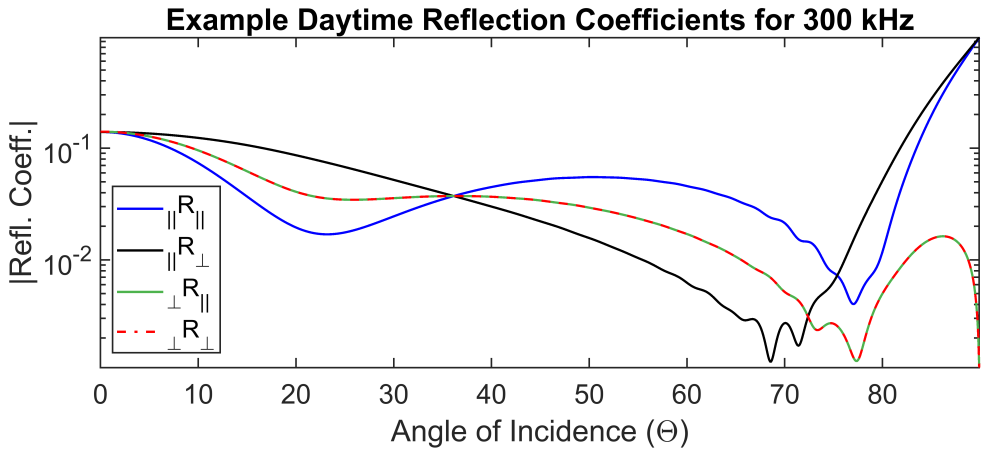

Figure 3.3: FWM reflection coefficients for a 300 kHz wave on a North-South path during daytime.

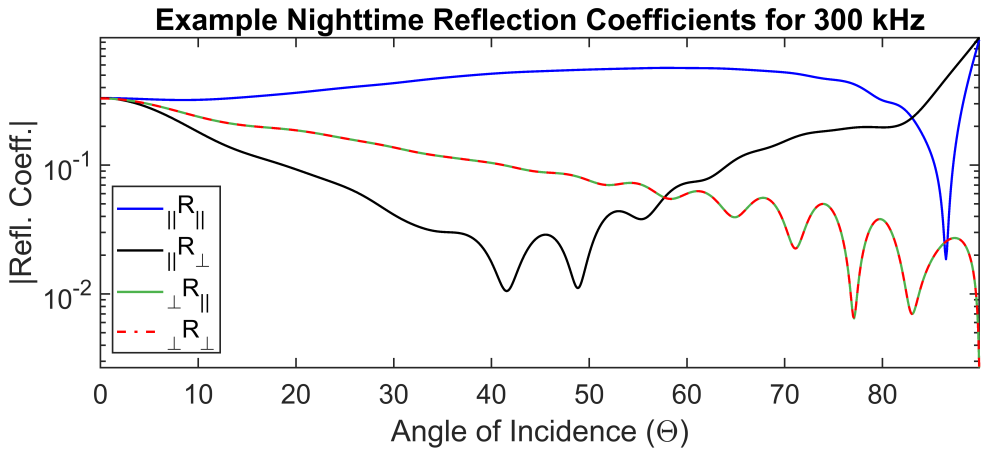

Figure 3.4: FWM reflection coefficients for a 300 kHz wave on a North-South path during nighttime.

The strength of this method is that it is computational fast and uses a relatively small amount of computing resources. However, the weakness of this method, related to LF/MF propagation, is that numerical errors appear in the reflection coefficients when they get smaller than $\approx< 10^{-3}$ and the method doesn't allow for a spatially varying ionosphere. Specifically, because of the first and third weaknesses, the FDTD method was used instead, which is discussed in the next section.

3.1.2 The Finite-Difference Time-Domain Method

The second method discussed is the finite-difference time-domain method (FDTD). This method has recently become popular in the field of VLF propagation, e.g. *Lee and Kalluri* [1999], *Cummer* [2000], and *Marshall* [2012], with the advent of faster computers and supercomputer clusters since it is a very computational intensive method. The basic premise of an FDTD model is that space and time are discretized into a grid, appropriate boundary conditions are implemented, and then time is incremented, and the grid space is updated until the model converges to a solution.

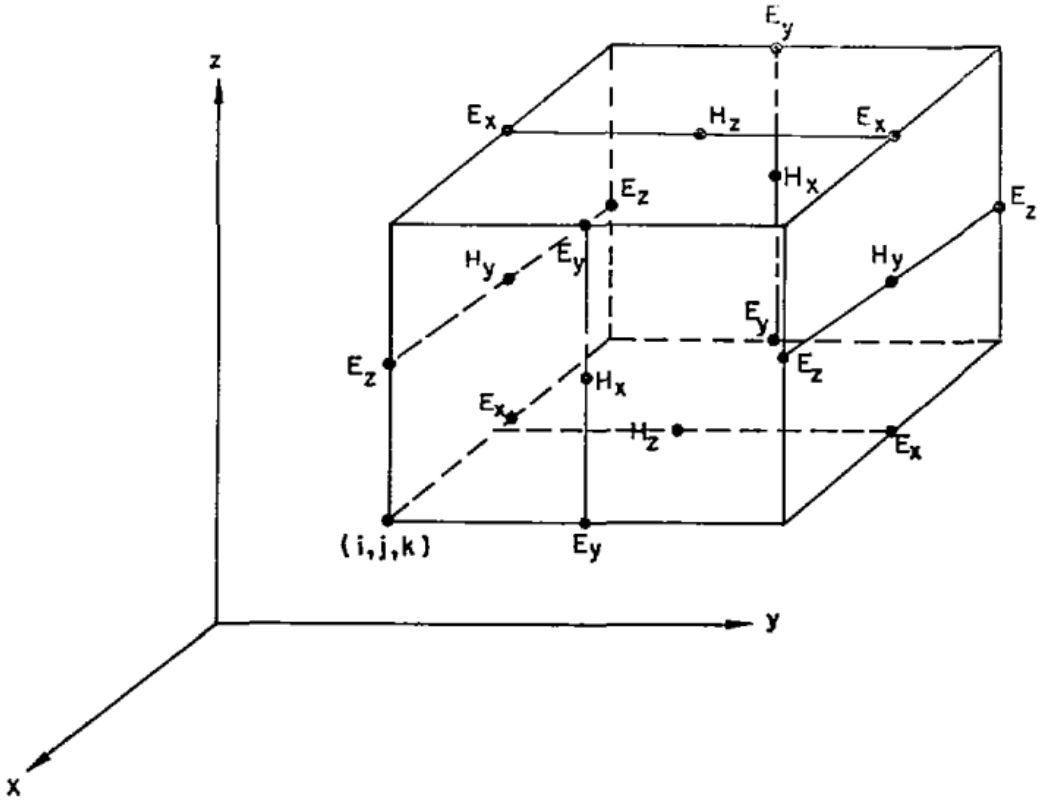

Figure 3.5: Example three dimensional Yee grid, adapted from *Yee* [1966].

A widely used grid method used is called the "Yee grid" after *Yee* [1966], also known as the "Yee lattice". Figure 3.5 depicts an example of a three dimensional Yee grid. The figure shows the position of the various components of the E and H components. The E components lie on the middle of the edges of the cells, while the H components are on the faces of the cells. The Yee grid can be thought of as two separate grids, one composed of E

components and the other of H components, which are superimposed on each other with an offset of half a cell. To update the grid, a "leap frog" method is employed in which the field components (E,H) exist, and are updated, at half a time step apart, $0.5\Delta t$. Figure 3.6 demonstrates the "Leapfrog" technique in a 1D example. Where t indicates the current time, n is some integer, and Δt is the time step. In the spatial domain, the k is some integer and Δx is the spatial step size. Effectively, each line represents a new point in time, whereas each line represents points in the spatial domain. In Figure 3.6, each row of a certain wave component is half a time step from the two rows above and below it and it must leap over the other wave component to be updated. Note that the figure reads from the top to bottom, with each row being an update to the grid space. The exact update equations used are not listed, but are widely available from literature (e.g. *Yee* [1966]) or derived from first principles. The spatial and temporal step sized used is critical for simulation stability. This relationship can be examined through the "Courant-Friedrichs-Lewy" (CFL) condition. *Yee* [1966] discusses this stability criterion, shown in Equation 3.1. Where Δx, Δy, and Δz are the spatial step sizes for the grid used, c_{max} is the maximum light velocity, and Δt is the temporal step size. The three spatial step sizes are only used in the case of a 3D grid. For reduced dimensionality, the unused grid steps are simply set to zero. When this inequality is true, the FDTD grid will be stable. The FDTD model used in this work for modeling the skywave was provided by Dr. Robert Marshall at the University of Colorado at Boulder, *Marshall* [2012]. This will be discussed in greater detail in Section 3.3.

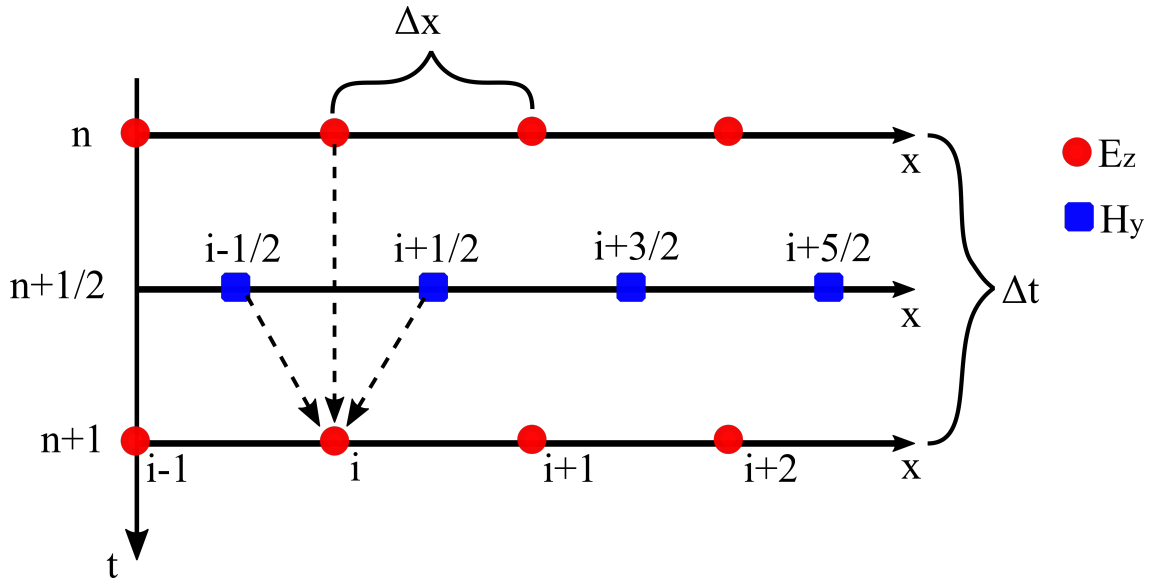

Figure 3.6: Graphical depiction of the leapfrog technique in a 1D Yee grid. From *Singletary* [2020].

$$\sqrt{(\Delta x)^2 + (\Delta y)^2 + (\Delta z)^2} > c_{max}\Delta t\,, \tag{3.1}$$

3.1.3 Summary of Methods

Two methods for modeling propagation in the Earth-Ionosphere Waveguide have been discussed: 1) the FWM, 2) the FDTD. Table 3.1 summarizes the strengths and weaknesses of both methods discussed in the previous two sections. The primary strength of the FWM is its computational speed and efficiency compared to the FDTD method. However, the major flaw, which makes it unusable for the purpose of this research, is that the D-region electron density can't spatially be varied to simulate a small-scale roughness. This can be done in an FDTD model, which is ultimately why an FDTD model was used for this research. This weakness and strength is highlighted respectively as *red* and *green* in Table 3.1.

Table 3.1: Summary of the strengths and weaknesses of the FWM and FDTD methods for modeling a wave propagating in the Earth-Ionosphere Waveguide.

Summary of Propagation Modeling Methods		
Model	Strengths	Weaknesses
Full-Wave Model	• Computationally fast • Low memory requirements	• Numerical errors when reflection coefficients become very small • Propagation is difficult to visual • Cannot spatially vary the D-region electron density
Finite-Difference Time-Domain	• Can easily "customize" the grid of the model (i.e. spatially vary the electron density) • Time domain problem allows for different frequencies to be simultaneously calculated	• Computationally intensive • Grid size is limited by the "Courant condition"

3.2 Groundwave

With VLF signals, the Earth can be approximated to be perfectly smooth, since the wavelength of the signals (10−100 km) are usually significantly larger than any terrain obstacles (such as mountains or buildings). However, at LF/MF, the wavelength (∼1 km) is comparable in size to medium size mountains or even skyscrapers. Hence, the flat-terrain approximation is no longer valid and existing VLF propagation models, such as the Long Wave Propagation Capability (LWPC), *Ferguson* [1998], cannot be reliably used in many situations.

As an example, we consider the propagation of a LF/MF signal across a mountain range, as is the case for a NDGPS transmitter near, Gustavus (Alaska), detected at the receiver in Juneau (Alaska). Figure 3.7 shows the diurnal variation of the amplitude for this scenario. The propagation path is 50 km and nearly in a west-to-east direction, divided in the middle by a north-south mountain range with some peaks reaching well over one kilometer in height, or more than a wavelength tall. The nighttime period is approximately between 5−15 UT and is distinguishable by the greater variability in the signal. The diurnal variation demonstrated here is markedly different from that shown in Figure 2.6. Typically, at such short distances we would expect the amplitude to be relatively flat since the groundwave isn't affected by ionospheric conditions. We hypothesize that this difference is due to the attenuation and shadowing caused by the mountain range changing the balance between the groundwave and very faint first skywave.

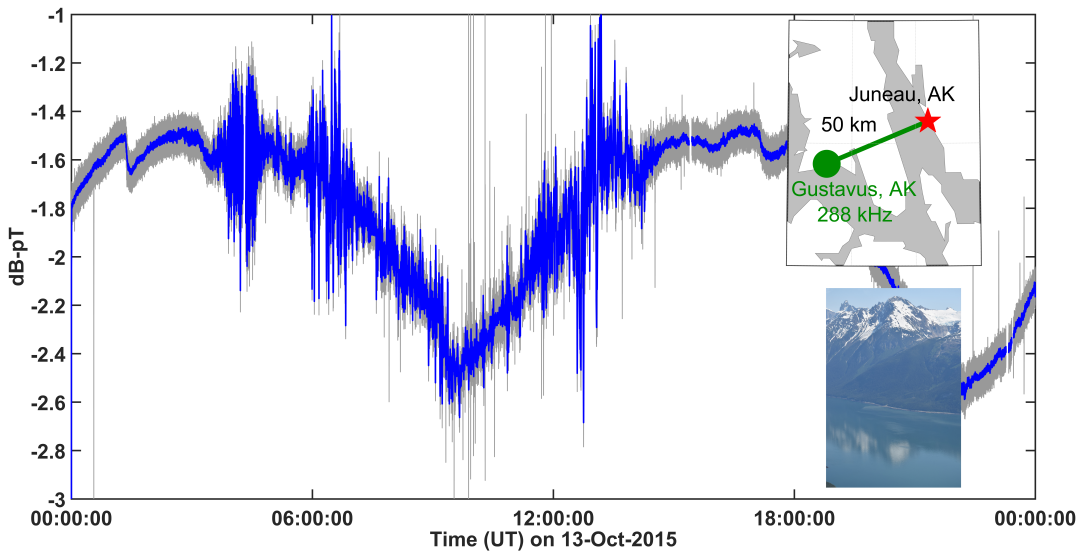

Figure 3.7: Observed amplitude diurnal variation in Juneau, AK, from a nearby NDGPS beacon. The top right sub-figure shows a map of the transmitter-receiver geometry and the bottom right sub-figure shows an image of the mountain range.

.

To model the ground wave attenuation for various propagation paths, a finite difference time domain (FDTD) code was custom built and run. Topographic profiles of the Earth were acquired using the NASA/METI ASTER GDEM data set, a product of NASA and METI. Conductivity and permittivity parameters of the Earth were acquired from look-up tables and inferred for the ground *ITU-R* [2017]. In the case of the propagation from Gustavus to Juneau, the path is only about 50 km and so the curvature of the Earth is neglected. Figure 3.8 shows the results from the FDTD model. The top panel of this figure shows the difference between the magnetic field for a simulation with the terrain profile and one with no terrain, i.e. propagating over saltwater. The transmitter is located at the bottom left, which causes the feature at around 1 km, and the receiver is located at the bottom right. The color indicates the extra path loss, in decibels, due to the realistic terrain, additional resistivity, and other effects inherent to the FDTD method, such as geometric dilution. The bottom panel shows this path loss along the profile of the terrain border with realistic conductivity values. Near the receiver, the effect of the terrain and higher resistivity, or the difference in the two simulations, is about $15-20$ dB. This level of attenuation is quite significant for such a short path and would otherwise have been

neglected with a simple flat earth approximation. More importantly, it means that the ground wave is sufficiently attenuated so that the balance between the ground wave and the first hop skywave is significantly altered. This scenario represents a more extreme case of groundwave attenuation. However, over much longer propagation paths (≈>600 km), which is the primary interest of this work, the groundwave is already sufficiently attenuated such that the skywave is the dominant mode, which is less susceptible to terrain effects and thus modeling the groundwave as precisely becomes unnecessary.

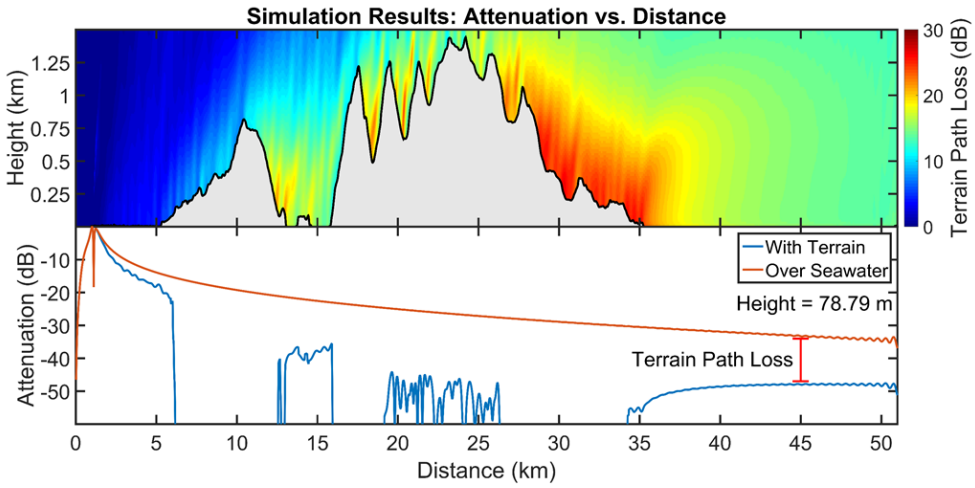

Figure 3.8: Top: Difference in dB between FDTD simulations with terrain and without. The terrain used is overlaid. Bottom: "Horizontal slice" of the top panel with the two separate path losses shown.

3.3 Skywave

The skywave, or wave that reflects from the ionosphere, is much more difficult to model. VLF (3−30 kHz) propagation modeling can leverage several simplifying assumptions, such as the flat-Earth approximation, and legacy code, namely LWPC. However, LWPC does not work well at 300 kHz. Thus, an FDTD model must be leveraged for this work. The FDTD model used in this work for modeling the skywave was provided by Dr. Robert Marshall at the University of Colorado at Boulder, *Marshall* [2012]. The model can use a 1D, 2D, or 3D grid. Figure 3.9 shows the grid space of model. The model runs in spherical coordinates, and the 2D grid, the second image from the left, is centered at the "north pole", i.e. at $\theta = 0°$. For modeling waves near a frequency of 300 kHz, a spatial step size of about 100 meters

is used. When modeling propagation paths on the order of 1000 km, this can generate quite a large simulation space to run. To overcome this computational burden, the Georgia Institute of Technology's Partnership for an Advanced Computing Environment (PACE) cluster is used to run the model. The code uses a "Convolutional Perfectly Matched Layer" (CPML) as a boundary condition, see *Roden and Gedney* [2000] and *Berenger* [1994] for a more thorough description of the formulation.

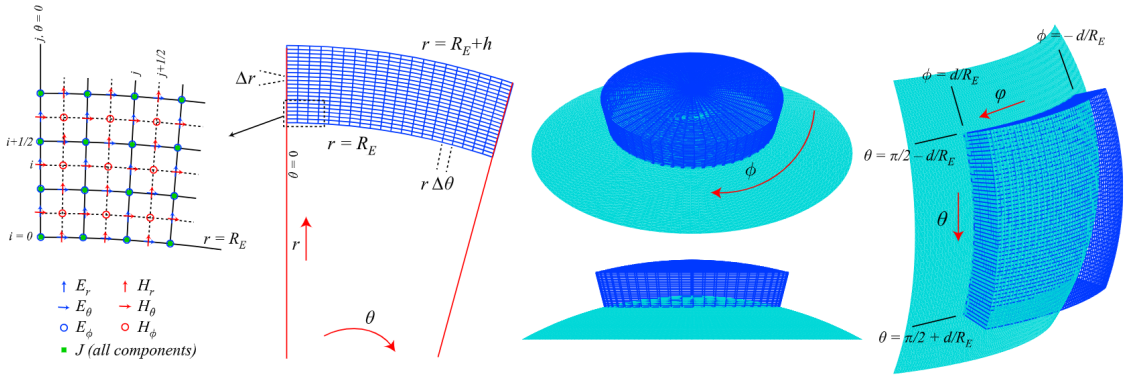

Figure 3.9: Grid space of the FDTD model used, adapted from *Marshall* [2012].

The underlying theory of FDTD modeling is not discussed here, but there are an abundance of sources that cover this topic in great deal, e.g. *Berenger* [1994]; *Lee and Kalluri* [1999] and citations within, or refer to Section 3.1.2. The difficulty in modeling transionospheric radio propagation, such as in the "Earth-Ionosphere Waveguide", is in modeling a magnetized plasma, an anisotropic medium, especially in the boundary conditions. Many sources exist that address this problem, e.g. *Hu and Cummer* [2006].

Two example runs from this model are highlighted in this section. Figure 3.10 shows the ground interference pattern for a 300 kHz source for a typical daytime D-region profile. Three regions are label. The red panel on the left is the region dominated by the groundwave. The middle green panel is the region dominated by the interference between the groundwave and the first skywave. The blue panel on the right is the region dominated by the first skywave. Figure 3.11 shows the same figure but for a typical nighttime D-region profile. Both figures reinforce results from earlier authors that suggest only 1-3 detectable modes propagate near this frequency, *Bickel* [1957]. Note that the nighttime result has a first skywave that is approximately 25 dB stronger than the daytime condition, which

greatly changes the structure of the interference region between the groundwave and first skywave. If we compare the two figures, a sanity check can be done by comparing the amplitudes. At around 800 km, the difference in the magnetic field amplitude is about 25 dB-pT, which compared to the top panel of Figure 2.1 in Chapter 4.2.1 is approximately the same difference between the nighttime amplitude and daytime amplitude.

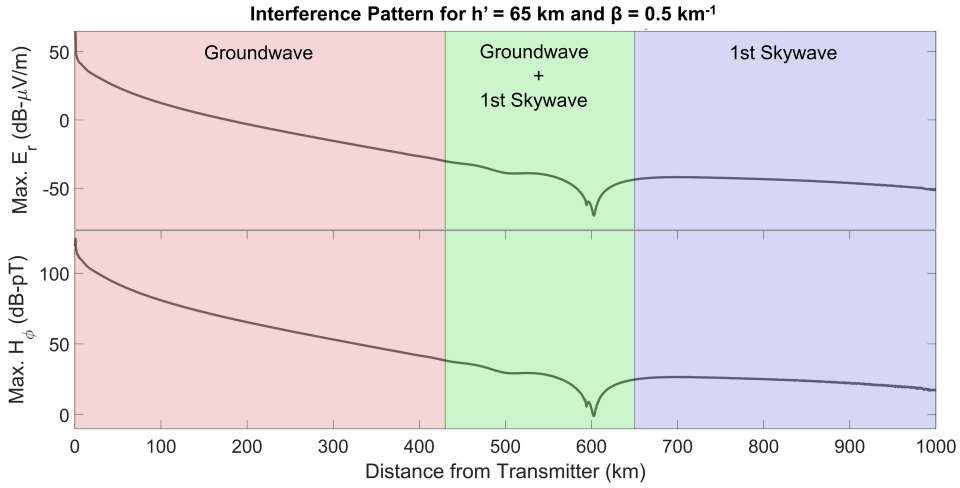

Figure 3.10: Ground interference pattern of a 300 kHz source with a typical daytime profile. Three approximate regions are labeled indicating the dominant mode(s).

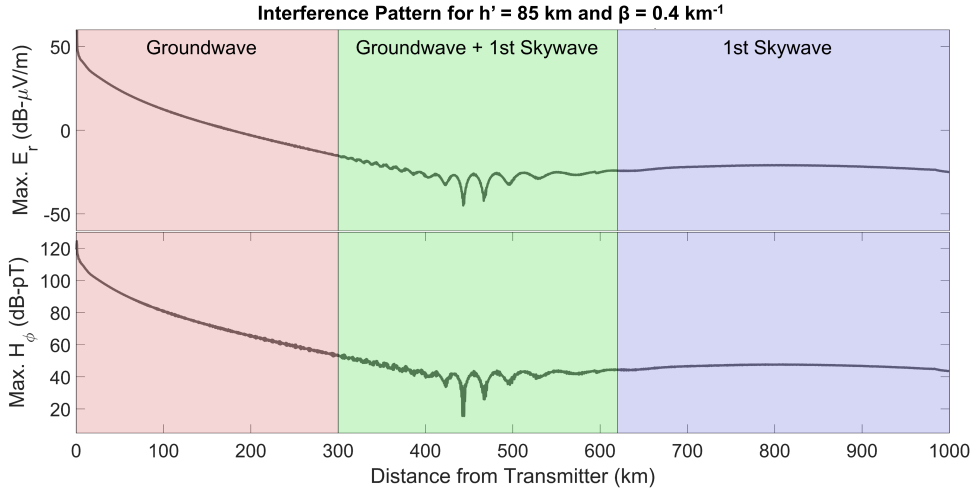

Figure 3.11: Ground interference pattern of a 300 kHz source with a typical nighttime profile. Three approximate regions are labeled indicating the dominant mode(s).

CHAPTER 4
SOLAR ECLIPSE CASE STUDY

In this chapter a case study will be presented to demonstrate the ideas and techniques described in the preceding chapters. First, previous and concurrent research of using lower frequency waves to measure the effect of solar eclipses on the D-region will be outlined, Section 4.1. Second, observations of the solar eclipse using NDGPS transmitters will be shown and described, Section 4.2. Thirdly, back scattering will be examined and modeled using the FDTD method. Finally, the "settling rate" of the D-region will be estimated using the modeled back scattering results, Section 4.3.

4.1 Background

Extensive research exists that examines the effect of a total solar eclipse on the D-region primarily by inferring changes using VLF transmitters, especially over long propagation paths. A few of those works will now be described briefly. *Sears* [1965] studied the 30-May-1965 solar eclipse by combining riometer, or relative ionospheric opacity meter, measurements at 20, 30, and 60 MHz and VLF measurements at 18 kHz from NLK in Jim Creek, Washington, near the totality path on the Cook Islands. A depression in the VLF phase of about 20% was observed. *Kaufmann and Schaal* [1968] studied the 12-November-1966 solar eclipse in South America using the VLF transmitter in Hawaii, NPM, at 26.1 kHz and observed a phase delay of 12.3 μsec from the totality spot as it crossed the propagation path. *Hoy* [1969] studied the 22-September-1968 solar eclipse over Asia using the GBR VLF transmitter in the United Kingdom, 16 kHz, received at Canberra, Australia, and found a phase delay of 3.3 μsec. *Schaal et al.* [1970] observed the 7-March-1970 solar eclipse by comparing the phase between three VLF transmitters detected by two co-located receivers in Brazil: 1) NLK in Washington at 18.6 kHz, 2) NAA in Maine at 17.8 kHz, and 3) the Omega transmitter in Haiku, Hawaii, at 10.2 kHz. *Lynn* [1981] studied the 23-October-1976 solar eclipse using four VLF transmitters detected by a receiver in Melbourne, Australia, and found that

the VLF phase response is a non-linear function of solar obscuration. The apparent time constant of ionospheric response was found to be 4 minutes and to be independent of the ionospheric reflection height.

Fewer papers have looked at LF/MF signals that investigate the ionospheric changes due to solar eclipses. The work done by *Sprenger et al.* [1962] examined the effect of two solar eclipses (30 June 1954 and 15 February 1961) on the D-region using frequencies between 191−1178 kHz. This work examined reflection heights and signal absorption for multiple transmitter-receiver paths during both events and found approximate values for the attachment and detachment processes during the event.

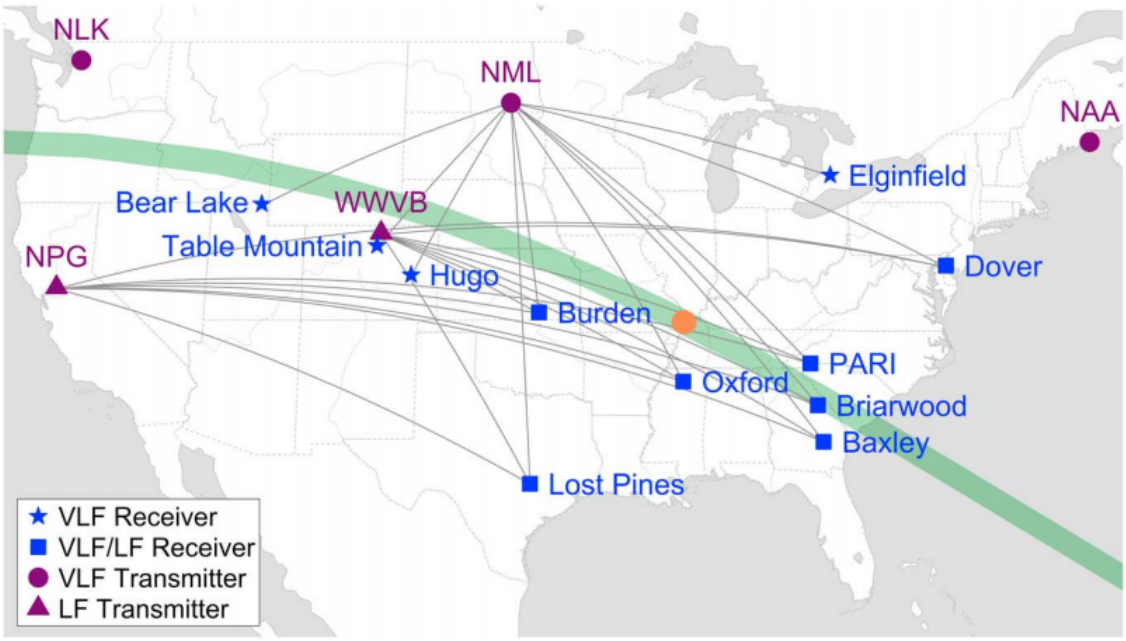

Figure 4.1: Map of transmitter-receiver observation configurations during the 21-August-2017 solar eclipse. Very low frequency (VLF) transmitters are shown as purple circles and low frequency (LF) transmitters are shown as purple triangles. VLF receivers are shown as blue stars and VLF/LF receivers are shown as blue squares. The green swath shows the path of the eclipse totality spot (from northwest to southeast) at an 80-km altitude. The orange spot is the location with the longest totality duration (2 min, 41 s), which occurred at 18:21:49 UT. The gray lines show the great circle paths for transmitter-receiver pairs that were recorded. From *Cohen et al.* [2018a].

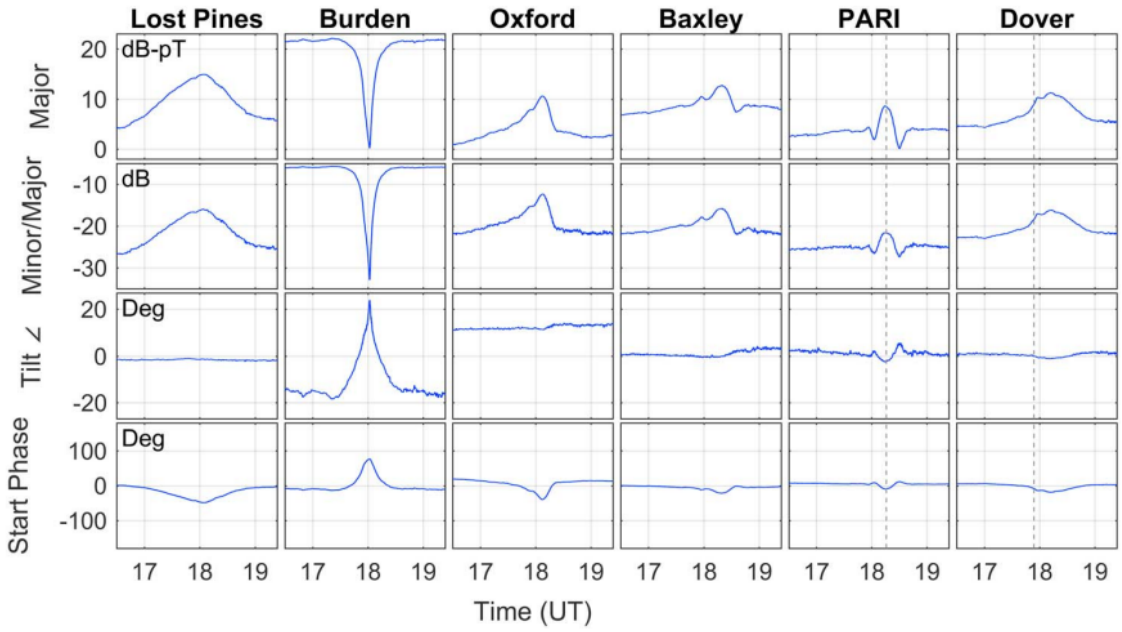

Figure 4.2: LF receiver polarization observations for the WWVB transmitter signal at 60 kHz during the eclipse. From *Cohen et al.* [2018a].

The "Great American Solar Eclipse" traversed the continental United States (CONUS) on August 21, 2017. Data from several receivers were collected simultaneously and the results for the VLF and low LF band were published *Cohen et al.* [2018a]. Figure 4.1 shows the transmitter-receiver path geometry of the data campaign. During this campaign, there were two types of receivers, the Georgia Tech LF AWESOME receiver, *Cohen et al.* [2018b], and the Stanford VLF AWESOME receiver, *Cohen et al.* [2010], detecting two types of transmitters: VLF naval transmitters and LF transmitters. Note that the NAA, in Maine, and NLK, in Washington, naval transmitters were not operational during the solar eclipse. Figure 4.2 shows the observations from the WWVB LF transmitter during the eclipse. The data from WWVB to Burden, second column of Figure 4.2, is particularly interesting since the eclipse totality spot is moving parallel to the path of propagation. The sharp minimum suggests destructive interference from the scattering off the eclipse spot. These figures are taken directly from the publication, *Cohen et al.* [2018a], and a more detailed analysis and discussion can be found therein. The polarization ellipse analysis described in Section 2.1.2 is used and depicted for seven LF transmitters, *Gross et al.* [2018]. Recall that the major axis length serves as a proxy for H_ϕ and the minor axis length as one for H_θ.

4.2 NDGPS Observations

In conjunction with the data collected in *Cohen et al.* [2018a], data from the NDGPS transmitters was also collected. The observations from the NDGPS transmitters will be discussed in the proceeding sections. Select observations will be segmented and discussed by the direction of scattering: 1) forward scattering and 2) back scattering. The data presented will utilize the polarization ellipse method, [*Gross et al.*, 2018], and focus on major axis length and minor axis length.

4.2.1 Forward Scattering

In the context of D-region remote sensing using VLF, LF, or MF transmitters, forward scattering refers to scattering from a perturbation located between the transmitter and receiver. Thus, the scattered signal propagates "forward" and is detected by the receiver, [e.g. *Johnson et al.*, 1999]. Figure 4.3 shows two examples of forward scattering from NDGPS transmitters during the 21-August-2017 solar eclipse. The leftmost panel shows a map of the two propagation paths being observed: 1) New Bern, NC, [35.175° N, 77.049° W] to Baxley, GA, [31.877° N, 82.534° W] at 294 kHz, and 2) Bobo, MS, [34.115° N, 90.691° W] to Pisgah Astronomical Research Institute, NC, [35.2° N, 82.872° W] at 297 kHz. The respective path lengths are 627.1 km and 726.6 km. The two center panels show the amplitude data for the transmitter in New Bern, NC, to Baxley, GA. The top panel shows the data for the major axis length and the bottom panel shows the data for the minor axis length, both are in units of decibel picoTesla, dB-pT. The right panels show the same data for the Bobo, MS, to PARI, NC, transmitter-receive path. The four vertical lines in each data panel, labeled T1−T4, correspond to the position of the totality spot in the map.

As the eclipse totality spot moves from northwest to southeast across both transmitter-receive paths there is a clear modification to the data plots in all four panels. There are some clearly similarities between the results in Figure 4.3 and Figure 4.2, namely a sharp rise or fall in the major or minor axis. Due to the higher frequency of the NDGPS transmitters, specifically 294 kHz or 297 kHz for the data presented, the phase interference observed in the major/minor axis length varies more rapidly, as seen in both cases. This is primarily

due to: 1) the shorter wavelength of 1 km and 2) the fewer propagating modes, as discussed in Chapter . This is most apparent when comparing the fifth column of Figure 4.2, the path from WWVB to PARI, and the third column of Figure 4.3, the path from Bobo to PARI. The minor axis length between both observations are comparable, with the modification in the NDGPS case lasting only about 20-minutes, while the modification in Figure 4.2 lasts about 40-minutes. The major axis trend is different between the two plots, the NDGPS transmitter major axis length increases and then decreases as the eclipse totality spot moves across the propagation path with a fading pattern, peaks and nulls from phase interference, superimposed on top of it. The middle column showing propagation from New Bern, NC, to Baxley, GA, shows a more pronounced case of phase interference. As the eclipse spot moves across the path, both the major axis and minor axis have two peaks and a null from the phase interference, though the minor axis has a much broader peak than the major axis.

4.2.2 Back Scattering

As opposed to forward scattering, back scattering occurs when the perturbation is "behind" the receiver. Thus, waves scattering off the perturbation propagate in the "backwards" direction and are detected by the receiver. Figure 4.4 shows an example of back scattering from NDGPS transmitters during the 21-August-2017 solar eclipse. The leftmost panel shows a map of the propagation path being observed: Tampa, FL, [27.8502° N, 82.5325° W] to Baxley, GA, [31.877° N, 82.534° W] at 312 kHz. The respective path length is 446.64 km. The two panels in the right column show the major and minor axis lengths in units of decibels of picoTesla, dB-pT, for this propagation path. The four vertical lines in both data panels, labeled T1−T4, correspond to the position of the totality spot in the map on the left.

As the eclipse spot moves from northwest to southeast, the top right panel showing the major axis length appears to trend downward until it reaches T3, when a fading pattern appears. At T3 there is an enhancement in the major axis, i.e. a peak, followed by a null just before T4, at around 18:47 UTC. It's important to note that the eclipse totality patch does not cross the propagation path, as seen in the map on the left. Thus, it appears that this modification is caused by back scattering from the eclipse spot. The bottom right panel

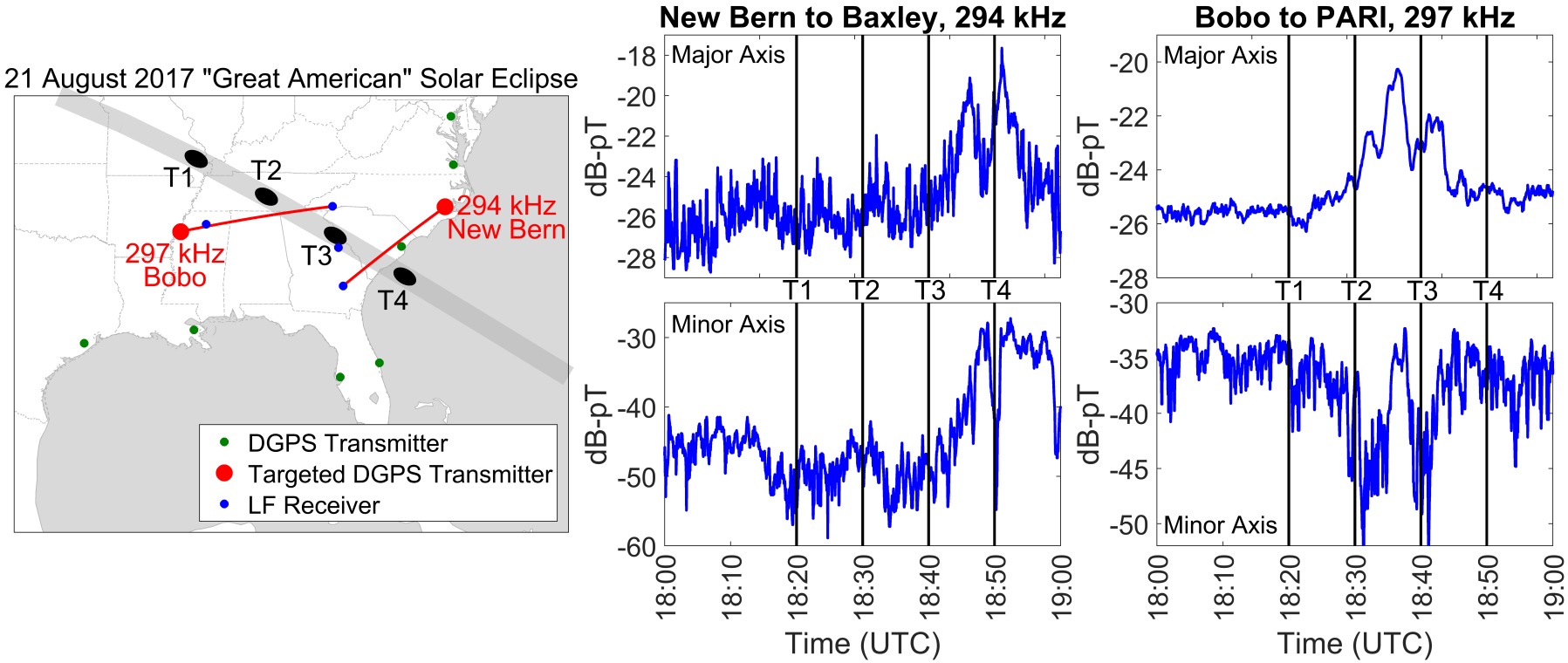

Figure 4.3: Map depicting the totality path of the eclipse (gray swath), the NDGPS transmitters (red and green), and the LF radio receivers (blue). The two red lines in the map are highlighted propagation paths shown in the center and right columns. The four black ellipses labeled T1-T4 are four highlighted positions of the eclipse totality spot. The times of these positions are shown in the two right columns and labeled accordingly.

showing the minor axis appears to be relatively flat with no clear modification caused by back scatter from the eclipse totality spot.

An important consideration for any observations during the 21-August-2017 solar eclipse is that a solar flare occurred at approximately the same time. Thus, care must be taken to ensure that the effect of the solar flare on the solar eclipse is accounted for. The top panel of Figure 4.5 shows the major axis length for 21-August-2017, blue line, and the previous day for reference, red line. The bottom panel shows the GOES-14 X-Ray Flux data for 21-August-2017. There is a rise in the X-Ray flux beginning at around 17:45 UTC that peaks at approximately 17:56 UTC. The onset of the X-Ray flux appears to correspond with the decreasing trend of the major axis length, blue line, as it departs from the quiet day, red line. This downward trend seen in the blue line appears well before the eclipse totality spot passes behind the Baxley, GA, receiver, which suggests that it is the effect of the solar flare on the major axis length.

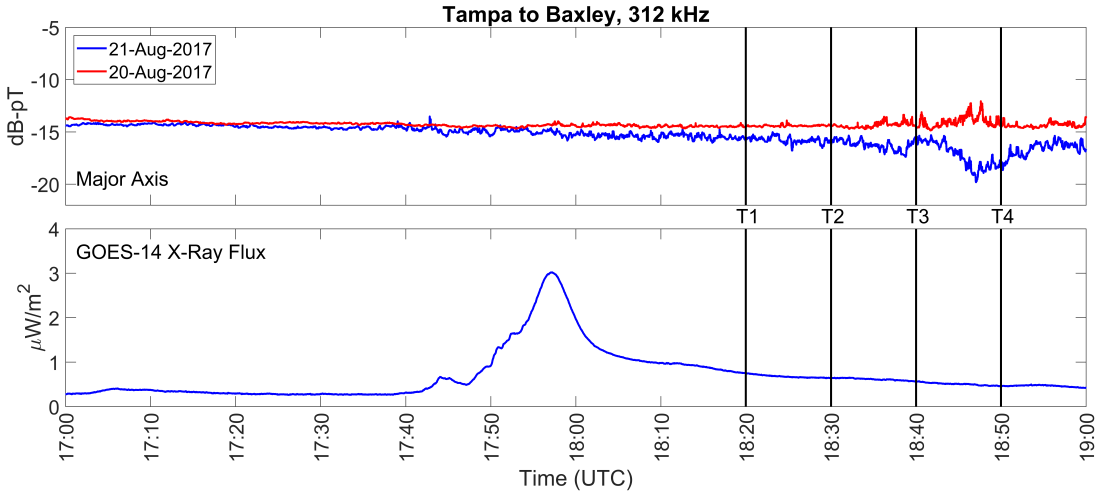

Figure 4.5: Impact of a solar flare on the data from the 21-August-2017 solar eclipse for the NDGPS transmitter in Tampa, FL, detected by a receiver in Baxley, GA, at 312 kHz. Top panel: Data from 21-August-2017, blue line, compared with the previous day, a quiet day, red line. Bottom panel: The GOES-14 X-Ray flux for 21-August-2017.

Now that the effect of the solar flare on the major axis length has been identified, it should be normalized in order to determine the contribution of the back scattering from the eclipse totality spot. Figure 4.6 shows how the data is normalized to account for the solar flare. The top panel once more shows the major axis length of the data from the Tampa,

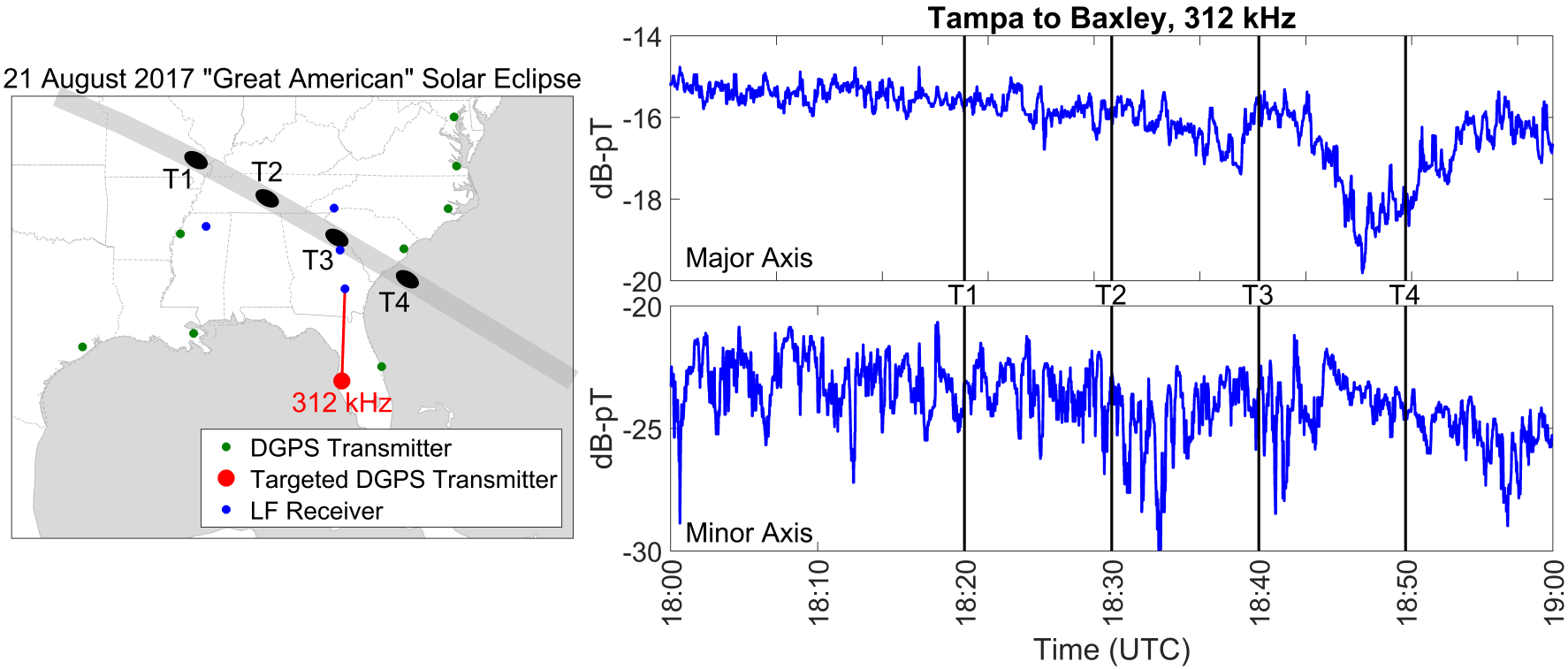

Figure 4.4: Map depicting the totality path of the eclipse (gray swath), the NDGPS transmitters (red and green), and the LF radio receivers (blue). The red line in the map is the highlighted propagation paths shown in the right columns. The four black ellipses labeled T1-T4 are four highlighted positions of the eclipse totality spot. The times of these positions are shown in the right column and labeled accordingly.

FL, NDGPS transmitter received in Baxley, GA, as the blue line. The red line is a linear fit to the downward trend that appears before the fading pattern, which is extrapolated to continue through the peak of the modification from the solar eclipse. The bottom panel shows the major axis length, blue from the top panel, with the best fit trend, red from the top panel, subtracted. The two dashed horizontal black lines show approximate values for the major axis length from the "quiet" D-region, bottom line, and from the perturbed D-region, top line. The difference between these two lines, labeled on the panel, is about 0.5 dB-pT, which is the enhancement to the major axis length resulting from the back scatter, with the effect of the solar flare removed. The 0.5 dB-pT enhancement near "T3" is assumed to be the back scattering from the solar eclipse totality spot because it is the time when the totality spot is located immediately behind the receiver, which is a requirement for the two-dimensional model in Section 4.3.

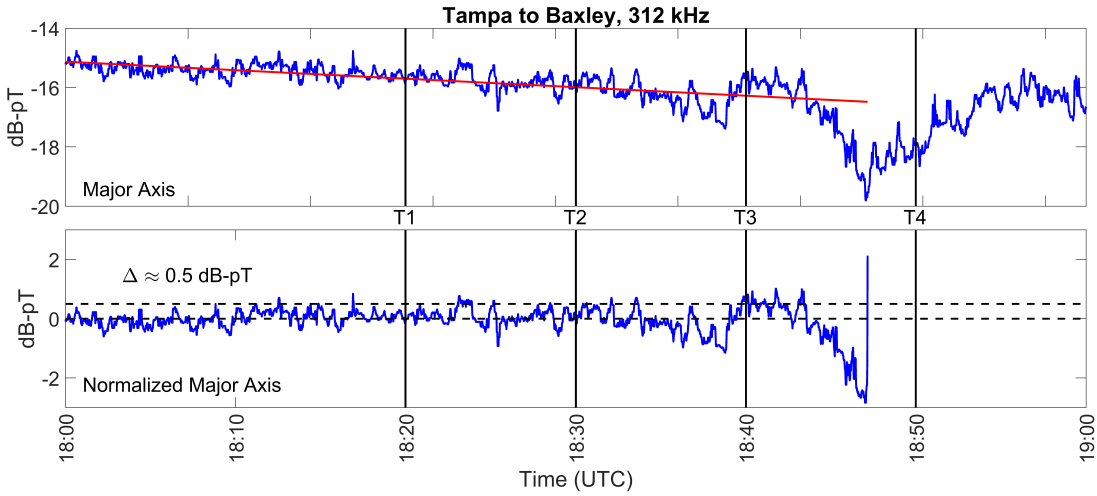

Figure 4.6: Normalizing the major axis length data from the 21-August-2017 solar eclipse to account for the effect of a solar flare. Top panel: The major axis length, blue line, of the Tampa NDGPS transmitter detected in Baxley, GA. A linear best fit to the steady downward trend is shown as a red line. Bottom panel: The major axis length normalized by the linear best fit of the downward trend caused by the solar flare. The two dashed black lines show the estimated "quiet" major axis length, bottom, and the back scattered major axis length, top line. The difference between the two lines is the back scattered major axis length and is found to be 0.5 dB-pT.

4.3 Numerical Modeling

We now investigate the back scattering described in Section 4.2.2 using the FDTD code described in Section 3.1.2 and Section 3.3. Figure 4.7 shows a cartoon diagram of the two-dimensional FDTD layout used to model the back scattering from the eclipse totality patch. The D-region electron density is effectively split into three regions, going from left to right: 1) typical daytime, 2) eclipse patch, and 3) typical daytime again. The "Wait and Spies Two Parameter Model", Equation 1.3, will be used to parameterize the D-region electron density. The daytime parameters, shown in a box at the top center-left of the figure, are $h' = 71$ km and $\beta = 0.43$ km^{-1}, from *Clilverd et al.* [2001] and *Thomson* [1993]. The distance from the NDGPS transmitter in Tampa, FL, to the receiver in Baxley, GA, is $d_1 \approx 446.6$ km. The distance from the NDGPS transmitter to the edge of the patch is $d_2 \approx 640.3$ km, or about 675.3 km to the center of the patch. The width of the patch, assuming a sharp boundary, is $d_3 \approx 70$ km. In Section 4.3.1, the eclipse path parameters will be varied to find a solution that matches the result in Figure 4.6. In Section 4.3.2, the selected h' and β will then be used to estimate the width of the transition region of the eclipse totality patch. This width estimate will then be used to estimate the settling rate of the D-region during the solar eclipse.

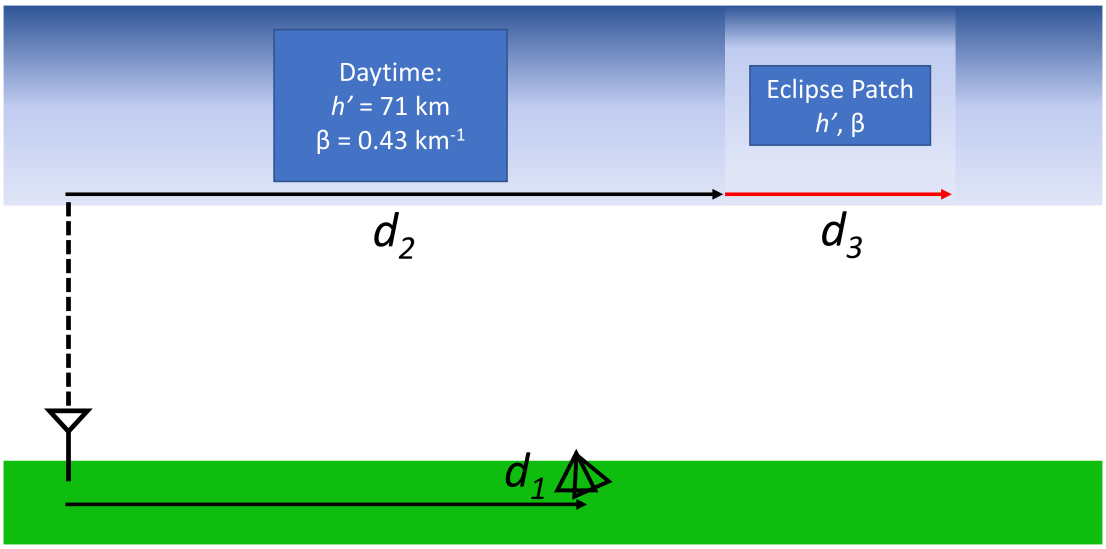

Figure 4.7: Grid layout for the two-dimensional FDTD model used to investigate back scatter from the eclipse totality patch. The daytime electron density parameters used are $h' = 71$ km and $\beta = 0.43$ km^{-1} and the eclipse patch electron density parameters will be varied.

4.3.1 Estimating Eclipse Patch Parameters

The back scattering mechanism of the Tampa-to-Baxley propagation path will first be investigated using the FDTD model described in Figure 4.7. There are three levers that can be used to vary the eclipse totality spot: 1) the h' of the eclipse totality spot, 2) the β of the eclipse totality spot, and 3) the transition width of the totality spot. As stated above, the daytime D-region electron density is assumed to be homogeneous and constant, with a $h' = 71$ km and $\beta = 0.43$ km^{-1}. The eclipse totality spot will be modified with combinations of h' from 77 km to 92 km and β from 0.5 km^{-1} to 0.9 km^{-1}. The third lever, the transition width of the totality spot, is modified by applying a moving average smoothing window on the h' and β arrays, which contain three segments: 1) daytime values, 2) eclipse spot values, and 3) daytime values. The variable that describes this parameter is the number of cells, or window width, used. Figure 4.8 depicts four cases of the D-region electron density. In each panel, the y-axis is the altitude range in kilometers and the x-axis is the distance from the transmitter in kilometers. The color of the image is the log-scale electron density in units of m^{-3}. The eclipse totality spot is located at around 675.3 km.

The top left panel shows the eclipse spot with no smoothing, the case with the sharpest boundary. In the top right panel, the smoothing window is increased to 2.5 km and the edges of the totality spot are no longer as sharp and a clear slope emerges. In the two bottom panels, the smoothing window is increased again, and the boundaries become much smoother.

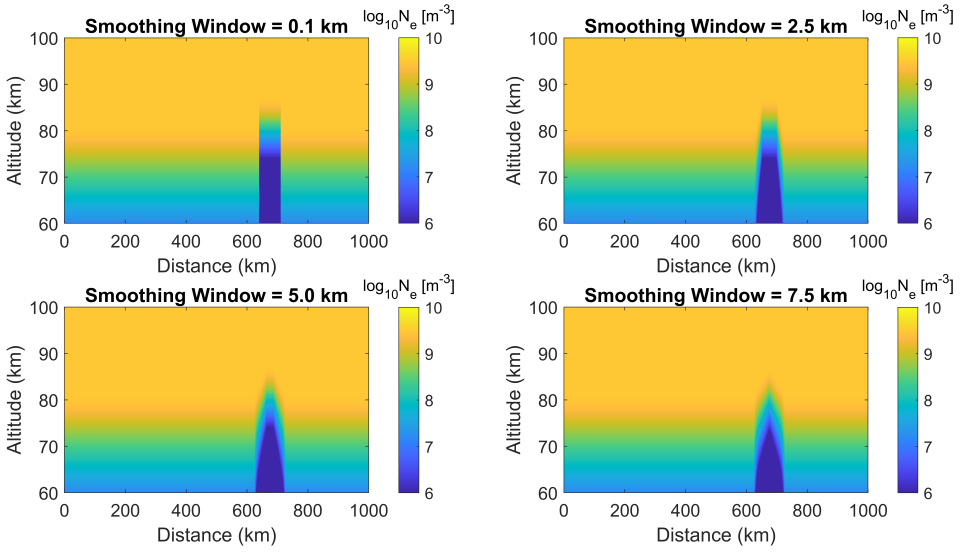

Figure 4.8: Examples of how the D-region electron density of the solar eclipse totality patch changes with varying smoothing window sizes. Top left to bottom right the smoothing window changes from 0.1 km to 7.5 km. Note that 0.1 km corresponds to a single cell and thus is effectively the same as having no smoothing window.

The modeled three-parameter space will use the h' and β ranges described above in combination with smoothing window sizes of 0 km, 2.5 km, 5.0 km, and 7.5 km. Figure 4.9 summarizes the resulting three-parameter space using the FDTD method. Each panel corresponds to a smoothing window size. Within each panel, the x-axis is the h' value and the y-axis is the β value. The color represents the ΔH_ϕ, which is calculated as the absolute value of the difference between the a "typical daytime" D-region electron density and the respective eclipse totality spot run in units of dB-pT, or decibels of picoTesla. A typical daytime D-region electron density uses a homogeneous ionosphere with $h' = 71$ km and $\beta = 0.43$ km^{-1}. Note that H_ϕ corresponds to the major axis length from the observations. The only panel with any detectable variation is the top left corresponding to a smoothing window of 0 km. This suggests that a very sharp boundary is needed to produce any detectable back

scatter from the solar eclipse totality spot. Using no smoothing, i.e. an instantaneously sharp boundary, the optimal solution is found by finding the configuration of the parameters that produces a back scattered ΔH_ϕ of about 0.5 dB-pT. As previously stated, the 0.5 dB-pT enhancement is assumed to be the back scattering from the solar eclipse totality spot because it allows for the use of a two-dimensional FDTD model. The optimal configuration of the three-parameters is found to be $h' = 80 \pm 3$ km, $\beta = 0.9 \pm 0.1$ km^{-1}. The error bars for h' and β are the parameter step sizes used.

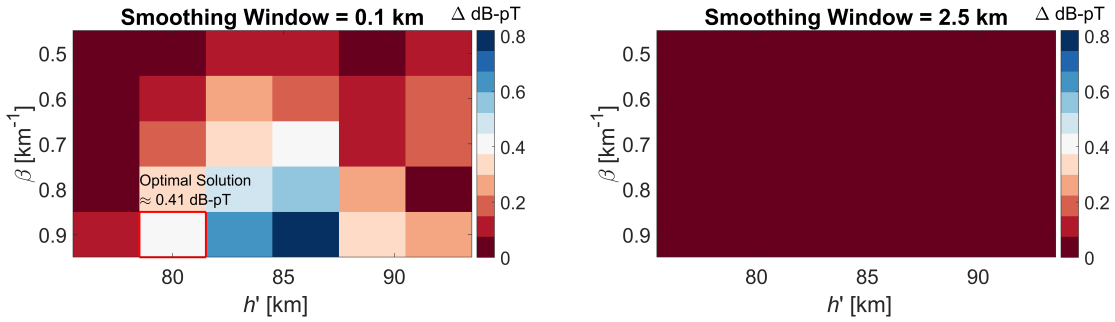

Figure 4.9: Summary of the resulting simulation voxel of the three-parameters used to vary the solar eclipse totality spot: h', β, and the smoothing window size. The color is the absolute value of the difference between a baseline case, i.e. typical daytime propagation, and the back scattered major axis length, H_ϕ.

Clilverd et al. [2001], studying the 11-August-1999 solar eclipse over Europe using VLF transmitters, estimated that the totality had a $h' = 79 \pm 1$ km and a $\beta = 0.5 \pm 0.01$ km^{-1} for very short paths, $\leq$600 km. This corresponds to a difference of $\Delta h' \approx 1$ km and $\Delta\beta \approx 0.4$ km^{-1} when compared to the results determined from the back scattering using an NDGPS transmitter, which can be attributed to three main factors. First, the work done by *Clilverd et al.* [2001] utilized VLF transmitters, 16−23.4 kHz, rather than NDGPS transmitters, 314 kHz. It is well known that the properties of a wave reflecting from the ionosphere vary with frequency, thus it is possible that some of the difference in h' and β are due to this characteristic. Second, the precision of the estimated parameters using the FDTD modeling described above is limited by the step size of the parameters. The values of h' are increments in 3-km steps and the β values are incremented in 0.1-km^{-1} steps. Thus, the precision, and possibly the agreement with the results from *Clilverd et al.* [2001], could be improved by using a finer sampling interval. Finally, in *Clilverd et al.* [2001] the

Long Wave Propagation Capability (LWPC) code is used for modeling. The reference D-region electron density is modeled identically to the work above with homogeneous values of $h' = 71$ km and $\beta = 0.43$ km^{-1}. However, for very short paths, $\leq$600 km, the totality of the eclipse is modeled using a single h' and β for the entire path. This effectively "averages" the perturbation over the entire propagation path. In contrast, the back scatter from the NDGPS transmitter is more akin to a point measurement rather than a path average. Thus, by using FDTD modeling for eclipse totality spot, the h' and β values determined are for the "true" eclipse totality spot and not for a path average.

Using the optimal parameters for the totality spot, the contribution of each "edge" of the spot to the total back scattered wave can be investigated. In the work above, a smoothing window was applied to the entire eclipse patch. Now, the smoothing window is only applied to half of the spot. This is meant to simulate the totality patch as it moves over the CONUS – the "soft" edge corresponds to the day-to-shadow side of the spot, i.e. the "front" of it, while the "sharp" edge corresponds to the shadow-to-day side of the spot, i.e. the "back" of it. The main assumption here is that the ionization caused by the Sun is almost an instantaneous process, while a shadow slows the ionization, but isn't instantaneous. Figure 4.10 shows the four possible configurations. The "near edge" indicates the edge of the totality spot closest to the transmitter/receiver, while the "far edge" is the edge away from them. The sloped edge corresponds to a "soft" edge, while the instantaneous edge corresponds to a sharp edge. The four cases are: 1) two sharp edges, 2) a sharp edge on the far edge and soft edge on the near edge, 3) a soft edge on the far edge and a sharp edge on the near edge, and 4) two soft edges.

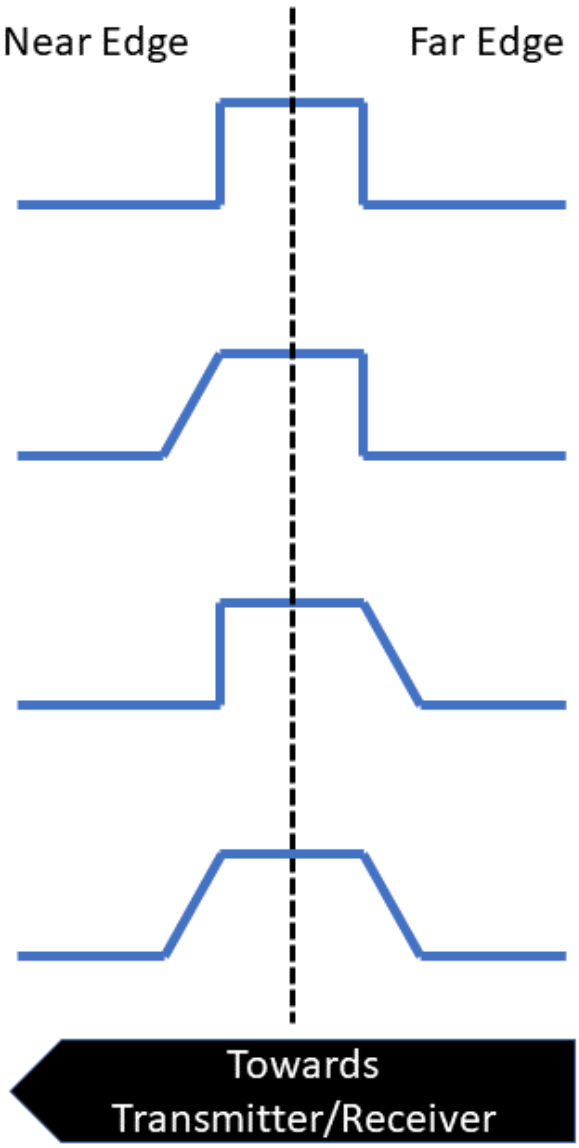

Figure 4.10: Cartoon depicting the geometry of the eclipse totality edge investigation. The "near edge" indicates the side closer to the transmitter/receiver, while the "far edge" is away from the transmitter.

Table 4.1 summarizes the results from the four cases. No smoothing window is used for a sharp edge and a smoothing window of 2.5 km is used for the soft edge. The greatest amount of back scatter is modeled when using two sharp edges for the totality spot, followed by using a soft near edge and sharp far edge. Negligible back scatter is detected in the two other cases. The case with the second most back scatter detected, the soft near edge and sharp

far edge, is most like the totality spot moving northwest-to-southeast across the CONUS. Since the totality spot is moving "diagonally" relatively to the predominantly north-south transmitter-to-receiver propagation path, the near edge of the spot would be a day-to-night transition and thus a soft edge, while the far edge would be a night-to-day transition and thus a sharp edge. This trend in the back scatter further assures that the detected signal is in fact back scatter from the eclipse totality spot. The discrepancy in detected back scatter between the two strongest cases, the top two rows of Table 4.1, can be explained by the error introduced by using a two-dimensional model to explain a three-dimensional phenomenon and by using a stationary model to explain a non-stationary process. The latter is especially meaningful, since, from examining the overall trend of each interference pattern, varying one edge from sharp to soft changes the direction of the back scatter. Thus, in the case of a soft near edge and sharp far edge, back scatter of about 0.41 dB-pT can be detected closer towards the transmitter. Thus, in a three-dimensional simulation space, as this totality spot moves to the southeast stronger back scatter would be detected by the receiver, such as in the case of the two sharp edges and as detected from observations.

Table 4.1: Summary from investigating the effect of each edge of the totality spot on the received back scatter using varying smoothing window sizes. The eclipse totality spot parameters used were $h' = 80$ km and $\beta = 0.9$ km^{-1}.

Near Edge Smoothing Window	Far Edge Smoothing Window	$\lvert\Delta H_\phi\rvert$
0.1 km	0.1 km	0.41 dB-pT
2.5 km	0.1 km	0.18 dB-pT
0.1 km	2.5 km	0.03 dB-pT
2.5 km	2.5 km	0.02 dB-pT

4.3.2 Estimating the Settling Rate

When the D-region is temporarily perturbed, the "steady-state" electron density, collision frequency, and other parameters and processes are disrupted for some period of time, e.g. *Rodger et al.* [2002]. The time it takes for the D-region to return to "normal" or recover from the perturbation is called the *settling rate*. Specifically, the settling rate described in this section refers to the rate that the D-region "changes" which allows for back scattering

to occur. During the 21-August-2017 solar eclipse, the totality spot traversing the CONUS created a "known" perturbation, a very rare occasion in geophysics, and useful for estimating the settling rate. Equation 4.1 describes how the settling rate, $T_{settling}$, will be calculated. The two unknowns that must be determined are: 1) the velocity of the totality, $V_{totality}$, and 2) the width of the transition region of the totality, $W_{totality}$.

$$T_{settling} = \frac{V_{totality}}{W_{totality}} \tag{4.1}$$

Coster et al. [2017] studied the impact of the 21-August-2017 eclipse on the total electron content (TEC) of the ionosphere and found that the "depletion" in the TEC caused by the eclipse moved at approximately the same speed as the totality. The first unknown, the velocity of the totality, is thus simply the velocity of the totality shadow moving along the ground. Thus, the totality spot velocity is assumed to be $V_{totality} \approx 0.65 \ \frac{\text{km}}{\text{s}}$.

The second unknown is the width of the transition region of the totality spot. Figure 4.11 shows the absolute value of the back scattered major axis length, $|\Delta H_\phi|$, as a function of the smoothing window size using an eclipse patch with the parameters $h' = 80$ km and $\beta = 0.9$ km^{-1}. At a smoothing window size of about 500 meters, the back scattered amplitude approaches zero. The width of this curve is the width of the transition region of the totality spot, thus $W_{totality} = 500$km.

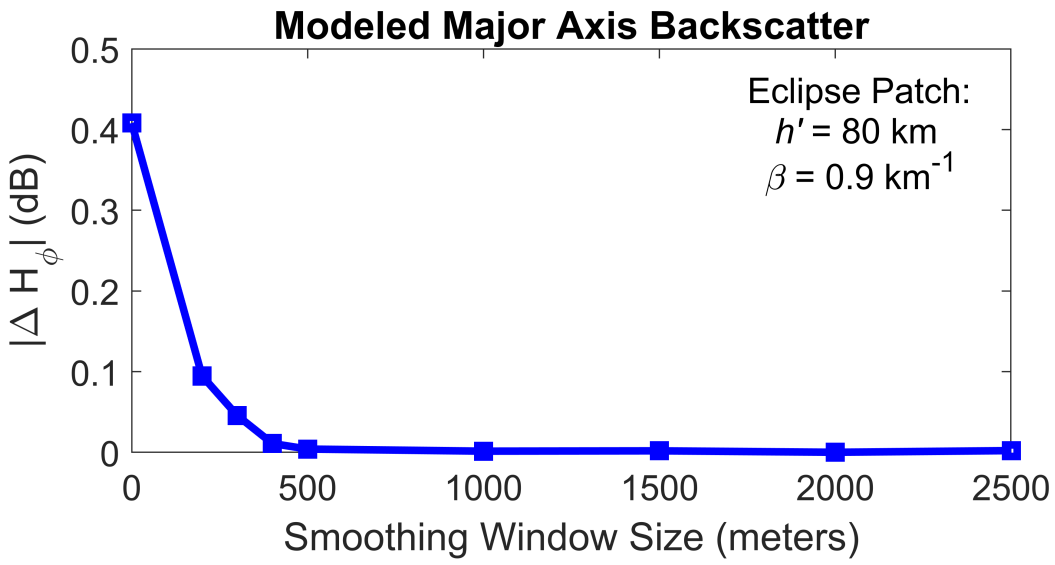

Figure 4.11: Absolute value of the back scattered major axis length, $|\Delta H_\phi|$, (blue line) as a function of the smoothing window size using an eclipse patch with parameters the $h' = 80$ km and $\beta = 0.9$ km^{-1}.

The two variables, $V_{totality}$ and $W_{totality}$, are now combined and the settling rate is calculated as in Equation 4.2. Thus, during the 21-August-2017 solar eclipse, the totality spot moving had a settling rate of 1.31s^{-1}. Referring back to Table 4.1, this settling rate describes a sharp edge. If the second case from the table, soft near edge and sharp far edge, is assumed to be the real case, then this settling rate describes the required rate of the far edge of the totality spot needed to allow back scatter.

$$T_{settling} = \frac{V_{totality}}{W_{totality}} = \frac{0.65 \ \frac{\text{km}}{\text{s}}}{0.5 \text{ km}} = 1.31 \text{ s}^{-1} \tag{4.2}$$

CHAPTER 5
CHARACTERIZING D-REGION ROUGHNESS

This chapter outlines two fundamental concepts needed to understand electromagnetic roughness: 1) the concept of what is a rough surface (Section 5.1) and 2) the idea of the "Fresnel zone" (Section 5.2). These two concepts are then used to derive two key metrics that will be used to measure the roughness of the D-region electron density in terms of the vertical, differential phase height (Section 5.3), and horizontal roughness, correlation length scale (Section 5.4). Finally, the method used for modeling the D-region electron density will be discussed, Section 5.5. A Monte Carlo Method is employed using dozens of Finite-Difference Time-Domain (FDTD) runs with randomized electron densities to deduce the associated amplitude variation. The amplitude variation is a function of space and time and cross-correlations between different distances are used to calculate a modeled, or estimated, correlation length scale that will later be used to connect the measured correlation length scale, or horizontal roughness, from field campaigns to a metric that describes the electron density roughness.

5.1 Rough Surfaces and the Rayleigh Criterion

What distinguishes a "smooth" surface from a "rough" surface? The early work done by Rayleigh, *Strutt* [2011] (later summarized by *P. Beckmann and A. Spizzichino* [1963] and *Ogilvy* [1991]), sought to answer this question by developing a criteria for simple physical interpretation of a surface, specifically to distinguish between smooth and rough surfaces, which will be briefly described. First, consider a monochromatic wave reflecting from a rough surface at some incidence angle, θ_1, such as in Figure 5.1.

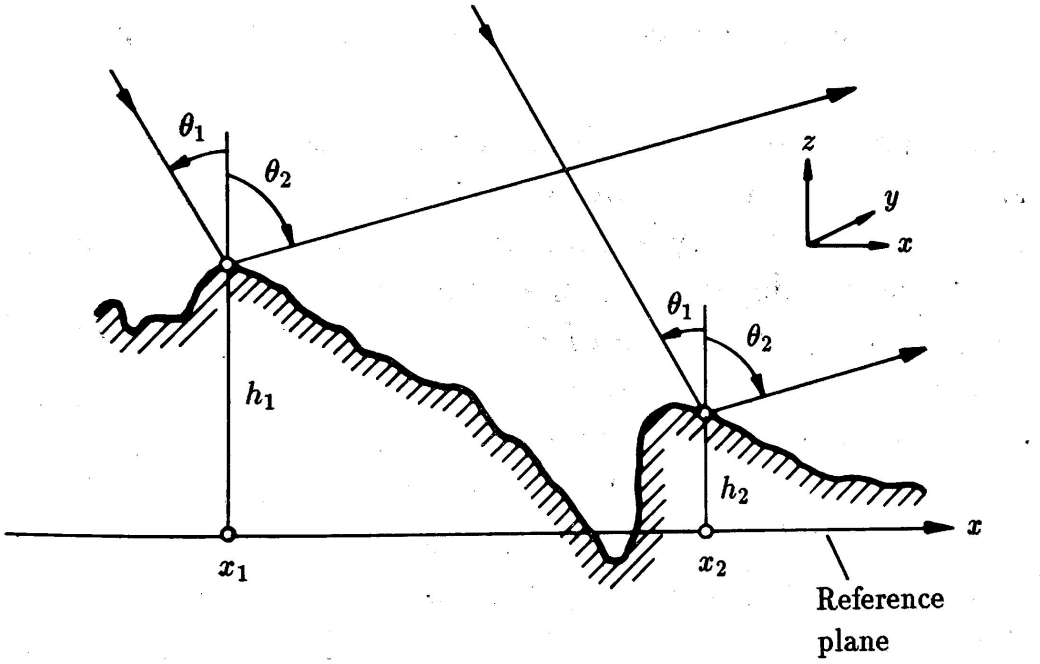

Figure 5.1: Diagram depicting two parallel rays scattered from different points on a rough surface. Adapted from *Ogilvy* [1991].

For a waves scattering in the $x - z$ plane, i.e. a two dimensional problem, with some angle, θ_2, the phase difference between two rays can be calculated using Equation 5.1. The scattering points are located at x_1 and x_2, k is the wavenumber defined as $\frac{2\pi}{\lambda}$, λ is the wavelength of the wave, and h_1 and h_2 are the heights of the reflection points from some reference plane. In the case of a "specular" reflection, when $\theta_1 = \theta_2$, the phase difference can be simplified into Equation 5.2, where $\Delta h = h_1 - h_2$.

$$\Delta\phi = k\left[(h_1 - h_2)(\cos\theta_1 + \cos\theta_2) + (x_1 - x_2)(\sin\theta_1 - \sin\theta_2)\right] \tag{5.1}$$

$$\Delta\phi = 2k\Delta h\cos\theta_1 = \frac{4\pi}{\lambda}\Delta h\cos\theta_1 \tag{5.2}$$

Equation 5.2 describes the difference in phase between the two waves as a function of: 1) difference in reflection height, 2) angle of incidence, and 3) wavelength. Assume that λ and θ_1 are held constant and Δh, the difference in reflection height, is increased from 0. At $\Delta h = 0$ the phase difference, $\Delta\phi$, will constructively interfere perfectly in the specular direction. However, as Δh increases, $\Delta\phi$ approaches π, which causes the rays to destructively interfere and thus provide no contribution in the specular direction. The *Rayleigh criterion* simply states that a surface with $\Delta\phi < \frac{\pi}{2}$ is considered a smooth surface and is otherwise considered rough. Equation 5.2 can be modified to express the Rayleigh criterion in terms of the height difference in the reflected waves such as in Equation 5.3. This form of the Rayleigh criterion allows for a physical interpretation of what is considered smooth and rough in the properties of the scattering surface.

$$\Delta h < \frac{\lambda}{8\cos\theta} \tag{5.3}$$

It should be noted that $\frac{\pi}{2}$ is an arbitrary choice and many other works have derived different criteria. For example, *Norton and Omberg* [1947] used $\Delta\phi = \frac{\pi}{4}$, thus replacing the factor of 8 in Equation 5.3 with a factor of 16. However, rather than trying to determine the exact point that distinguishes a smooth and rough surface, it is perhaps more useful to determine a measure of effective surface roughness. Re-examining Equation 5.2, it can be concluded that a surface becomes effectively smooth when the two conditions in Equation 5.4 are met. These conditions qualitatively show that a surface may appear smooth in three situations: 1) the difference in reflection height between two points approaches 0, 2) the wavelength becomes significantly large, and 3) the angle of incidence becomes very oblique.

$$\frac{\Delta h}{\lambda} \to 0 \text{ or } \theta \to \frac{\pi}{2} \tag{5.4}$$

The above description of the Rayleigh criterion and the qualitative assessment of an effectively smooth surface is meant to highlight an important concept: the roughness of a scattering surface is not an intrinsic property of the surface, but rather a property of the wave being reflected from the surface and is a function of wavelength and angle of incidence. Thus, it is important to think of the scale of roughness in relations to the wavelength of

the incident wave. A common notation used to demonstrate the scale of roughness is to normalize values by the wavelength of the incident wave or by the wavenumber of the incidence wave.

When a scattering surface is not deterministic and is generated by some random process, such as the surface of the ocean or the D-region of the ionosphere, it becomes necessary to determine statistical measures for characterizing the surface. Two classic parameters for statistically characterizing surface roughness are the *RMS (Root-Mean-Squared) height* and *correlation length*, e.g. *Manninen* [1997]. Imagine a propagation scheme where an incident radio wave is being scattered by the surface of the ocean. The RMS height may be thought of as the "vertical roughness" of the surface and the correlation length as the "horizontal roughness". These metrics will be covered in more detail in the proceeding sections.

5.2 The Fresnel Zone

To determine the location and size of an active scattering region contributing to the total field at a receiving point from a surface illuminated by a source the commonly accepted answer is the *Fresnel zones*, specifically the first Fresnel zone. At oblique incidence angles, such as in the case of a radio wave reflection from the lower ionosphere, this answer becomes less rigorous, but has been used in other works in this context, such as in *Lay and Shao* [2011a] and *Lay and Shao* [2011b].

Imagine a surface, such as the blue surface at the top of Figure 5.2, illuminated by a transmitter, such as on the left side of the figure, that in turn reflects radio waves, which are detected by a receiver at some distance, d, as seen on the right side of the figure. The locus of all points on the reflecting surface that generate a reflection that arrives at the receiver with a constant phase difference, δ, with respect to the direct radiation along d is given by Equation 5.5. In Equation 5.5, R_1 and R_2 are the distances of the up going and down going rays and δ is the constant phase difference. If δ is incremented in steps of $\frac{\lambda}{2}$, concentric ellipses with phase differences of π will arise. This effectively creates rings of alternating constructive and destructive phase interference, seen as the ellipses at the top of Figure 5.2, where the first Fresnel zone will be defined as the area inside the first ellipse

where the locus of all points will constructively interfere with a phase of π. In general, the first Fresnel zone, or the first ellipse on the surface, has the greatest contribution to the received signal because of the following reasons: 1) the concentric ellipses, after the first Fresnel zone, have a decreasing area and thus decreasing contribution to the received signal, 2) the alternating concentric ellipses of constructive and destructive interference, though not identical in size, approximately cancel out. For a thorough reference text on Fresnel zones and related topics refer to *P. Beckmann and A. Spizzichino* [1963].

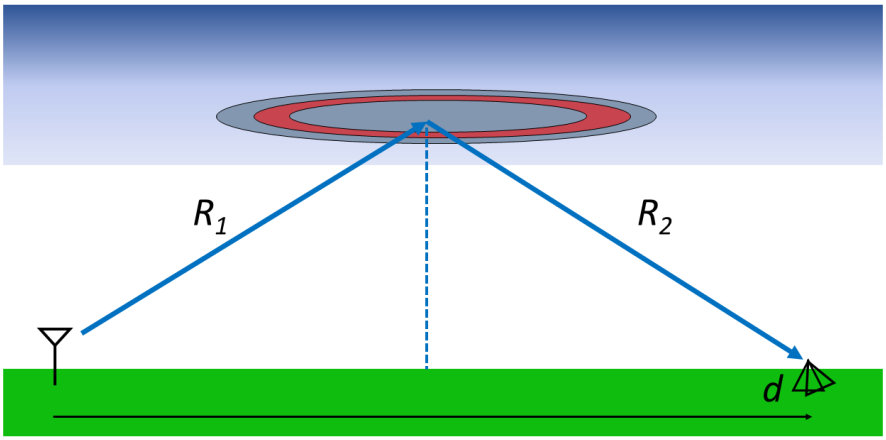

Figure 5.2: Depiction of the first three Fresnel ellipses in context of the propagation scheme of interest: low frequency waves reflecting off the lower ionosphere and detected by a receiver, right, at some distance, d, from a transmitter, left.

$$R_1 + R_2 - d = \delta \tag{5.5}$$

In the case of a receiver detecting the signal from an LF/MF transmitter, such as an NDGPS transmitter, at oblique incidences, the first Fresnel ellipse will appear as an ellipse that becomes more elongated as the distance between the transmitter and receiver increases. The direction along the path of propagation, or rather the direction towards the receiver from the transmitter, is called the *radial* direction. The direction perpendicular to the direction of propagation is called the *transverse* direction. Table 5.1 shows estimated values for the radial radii and transverse radii for varying propagation distances. The frequency of the propagating wave has a frequency of 300 kHz and a reflection height of 90 km in all

scenarios. The table shows a clear increasing trend as the distance of propagation increases. The radial radius, which is along the path of propagation, increases much more dramatically than the transverse direction. This table shows that the active scattering region, i.e. the Fresnel zone, can become quite large at longer distances, reaching an area of about 6318.9 km^2 at 1200 km. However, it should also be noted that, at distances of about $700 - 1200$ km, the first skywave is the dominant mode. This means that, at these distances, the first Fresnel zone is effectively a "patch" of the D-region that is being probed by the LF/MF waves with minimal contributions from higher order modes. The metrics discussed in the next sections will focus on describing the "vertical" and "horizontal" roughness of the D-region by exploiting this concept, specifically that the patch of the D-region being probed is more or less equivalent to the Fresnel zone at the center of the propagation path between the transmitter and receiver.

Table 5.1: Estimated radial and transverse radii for the first Fresnel ellipse of different propagation path lengths using a frequency of 300 kHz and reflection height of 90 km.

Propagation Distance (km)	Radial Radius (km)	Transverse Radius (km)
300	18.11	9.36
600	43.18	12.53
900	76.22	15.16
1200	115.33	17.44

5.3 Vertical Roughness

As previously stated, one of the key metrics for characterizing the "roughness" of a media is the vertical roughness, or its vertical variability. Unfortunately, deriving precise reflection heights of low frequency waves reflection from the D-region ionosphere is a difficult problem. Often times, the h' metric from the "Wait and Spies Two Parameter Model" is mistakenly referred to as the reflection height, e.g. *McRae and Thomson* [2000] and *Thomson et al.* [2007], but rather describes a variable that is similar to a "y-intercept" in the model that fits to an electron density profile. As an alternative, an array of methods which describe

a "virtual" or "phase" reflection height have been developed. These methods attempt to exploit some underlying physical assumption of the propagation problem to create a proxy for reflection height, or change in reflection height, of a propagating wave. A summary of these methods will be described below.

5.3.1 Wavelength Change Method

An early method was developed by E. V. Appleton, *Appleton* [1928], to study the nighttime interference fading observed in Medium Frequency (e.g. $\lambda = 385$ meters) signals is called the *wavelength change method*. Figure 5.3 depicts an example of the nighttime interference amplitude pattern that Appleton studied in his paper. The propagation scheme for Figure 5.3 is depicted in Figure 5.4. In this scenario, there are two ray paths: 1) the "groundwave" that propagates via *TO* and 2) the "skywave" (or down coming wave) that propagates via *TBO*.

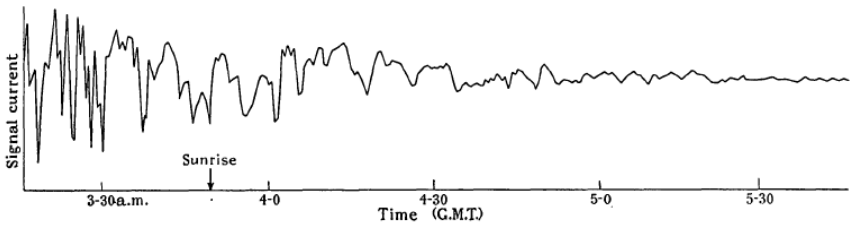

Figure 5.3: Example amplitude fading of a $\lambda = 385$ meter signal captured by a receiver in Peterborough from transmitter in Manchester on 1 July 1927. From *Appleton* [1928].

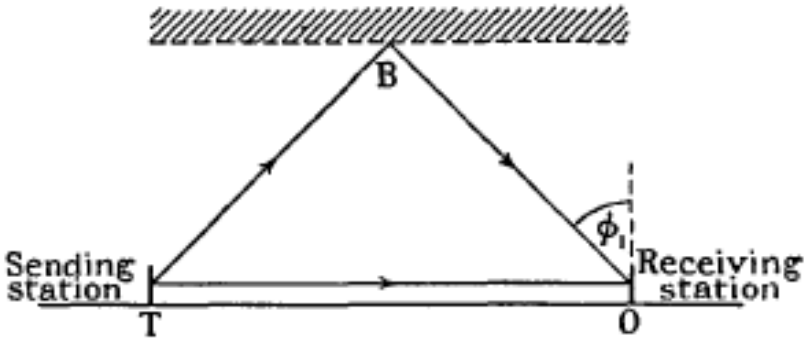

Figure 5.4: Propagation geometry assumed for the Manchester-Peterborough path in Figure 5.3. Adapted from *Appleton* [1928].

Two critical assumptions made by this work are: 1) the interference generated by the

skywave (TBO) and groundwave (TO) is due to a change in phase, θ from Equation 5.6, which can be interpreted as a small change in *wavelength*, λ, (hence "wavelength change method"), and 2) for a small change in wavelength, λ, the equivalent path difference between the two propagating rays, D from Equation 5.6, is constant. Note that in Equation 5.6, the units of D and λ should cancel and so the resulting phase, θ, is in units of radians. Using these two assumptions, the paper outlines a method for studying: 1) the relative change in amplitude between the skywave and groundwave, 2) a method of calculating the *angle of incidence* of the down coming skywave, ϕ, and 3) a method for measuring the change in effective reflection height.

$$\theta = -\frac{\omega D}{c} = -\frac{2\pi D}{\lambda} \tag{5.6}$$

The first metric of interest to Appleton was determining the relative strength of the skywave, H_1, to the groundwave, H_0. Imagine that the wavelength, λ, of the signal is gradually increasing, then the phase, θ, will eventually alter by 2π and pass through a signal amplitude maximum and minimum. The number, n, of maximums, or minimums, can be calculated using Equation 5.7. In that equation, θ is defined by Equation 5.6, which can be used to simplify Equation 5.7 into the form on the right-hand-side.

$$n = \frac{\theta_1 - \theta_2}{2\pi} = \frac{D}{\lambda_1} - \frac{D}{\lambda_2} \tag{5.7}$$

Assuming that D remains approximately constant for small changes in wavelength and without knowledge of the day-time value of the signal, i.e. the groundwave, the relative strengths of the skywave and groundwave can be calculated using Equation 5.8. Where H_1 is the skywave, H_0 is the groundwave, M is the signal maximum that indicates that θ is an even integer of π (e.g. 0, 2π, 4π, etc.), and m is the signal minimum that indicates that θ is an odd integer of π (e.g. π, 3π, 5π, etc.).

$$\frac{2H_1}{H_0} = \frac{\sqrt{M/m} - 1}{\sqrt{M/m} + 1} \tag{5.8}$$

The second metric of interest is the angle of incidence, ϕ_1. Imagine a scenario where

there are two simultaneous receivers collecting data: 1) an aerial antenna, 2) a loop antenna on the ground. In the same fashion as deriving Equation 5.8, two equations can be derived: one for the aerial antenna above the loop antenna, Equation 5.9, and one for the loop antenna on the ground, Equation 5.10.

$$\frac{2E_1 \sin\phi_1}{E_0} = \left[\frac{\sqrt{M/m}-1}{\sqrt{M/m}+1}\right]_{Aerial} \tag{5.9}$$

$$\frac{2H_1}{H_0} = \left[\frac{\sqrt{M/m}-1}{\sqrt{M/m}+1}\right]_{Loop} \tag{5.10}$$

Since H_1/H_0 is equal to E_1/E_0, we can solve for the angle of incidence using Equation 5.11.

$$\sin\phi_1 = \frac{\left[\frac{\sqrt{M/m}-1}{\sqrt{M/m}+1}\right]_{Aerial}}{\left[\frac{\sqrt{M/m}-1}{\sqrt{M/m}+1}\right]_{Loop}} \tag{5.11}$$

The third metric of interest is a method for estimating the equivalent reflection height. Calculating $\delta n/\delta\lambda$, or the number of fringes per meter of wavelength change, yields a quantity that is proportional to the path difference, D, between the groundwave and skywave. Thus, an increase in $\delta n/\delta\lambda$ would indicate an increase in the equivalent reflection height. Figure 5.5 shows an example of determining the change in equivalent reflection height using this method during the June 29th, 1929, solar eclipse in the United Kingdom. The left y-axis shows the values of $\delta n/\delta\lambda$ while the right y-axis shows the estimated equivalent reflection height. The left side of the plot shows the nighttime data, with the sunrise occurring just before 4 GMT, indicated by an arrow. The equivalent reflection height is high, at around $100-110$ km, during the night and gradually decreases, which is expected since as the sun rises the ionization in the D-region increases, causing lower frequency waves to reflect at lower altitudes. During the eclipse totality, indicated by an arrow around 5:30 GMT, the equivalent reflection height once again increases due to the decrease in D-region ionization.

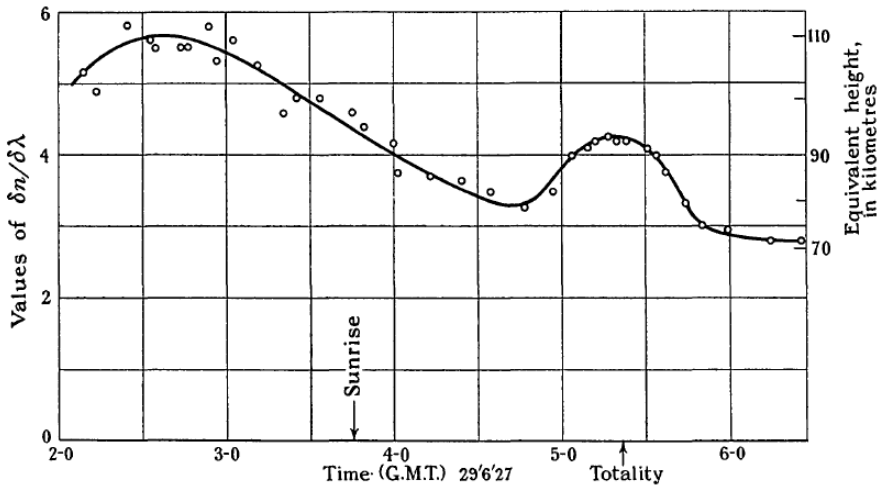

Figure 5.5: Estimated change in equivalent reflection height using the wavelength change method for the June 29th, 1927, solar eclipse at $\lambda = 491$ meters. Adapted from *Appleton* [1928].

The strength of the method outlined by Appleton in *Appleton* [1928] is that it only requires the amplitude intensity measurement of two antennas with no knowledge of the groundwave. However, the weakness of this method is that it requires access to a transmitter in which the frequency can be varied. Unfortunately, due to the constraint of using a signal of opportunity, the weakness of this method makes it unusable.

5.3.2 Phase Height

As mentioned in the previous section, using the wavelength change method requires a transmitter that can vary the frequency of the transmitted signal. However, by using a signal of opportunity, such as the NDGPS transmitters, the frequency is assumed to be constant and invariant, atleast within the bounds of MSK modulation. Thus, the propagating wave is "monochromatic" and a method that determines the effective reflection height of a monochromatic wave must be utilized. A series of two papers by *Pitteway* [1965] and *Piggott et al.* [1965] describe the numerical calculation of wave fields, reflection coefficients, and polarization from low frequency waves reflecting from the lower ionosphere. Specifically, *Piggott et al.* [1965] has a section that describes three methods of estimating reflection height that all use phase. These methods will be briefly discussed.

The first method described in *Piggott et al.* [1965] is called the *phase height* method and

is described by h_1 in Equation 5.12, where λ is the wavelength, I is the angle of incidence from the vertical plane pointed from the ground to the ionosphere, θ_g is the phase difference between the upgoing and downcoming waves observed at the ground, and M is simply an arbitrary integer. It is import to note, that the solution of Equation 5.12 is not unique and is dependent on the choice of M.

$$\frac{-4\pi h_1}{\lambda}\cos I = (2M+1)\pi + \theta_g \tag{5.12}$$

The second method is called the *triangulation height* and is described by h_2 in Equation 5.13. The triangulation height is defined as the reference height which makes $\delta\theta/\delta I = 0$. As I tends to normal incidence ($I = 0°$), the solution tends to infinity, unless it happens that $\delta\theta/\delta I = 0$ in rare circumstances.

$$h_2 = \frac{\lambda}{4\pi \sin I}\frac{\delta\theta_g}{\delta I} \tag{5.13}$$

The final reflection height method described in *Piggott et al.* [1965] is the *virtual height* method described by h_3 in Equation 5.14, where c is the speed of light. The virtual height is defined as the reference height which makes $\delta\theta/\delta f = 0$.

$$h_3 = -\frac{c}{4\pi \cos I}\frac{\delta\theta_g}{\delta f} \tag{5.14}$$

In general, it is important to note that $h_1 \neq h_2 \neq h_3$ and the author suggests the use of the mean of all three methods. However, since the angle of incidence and frequency are invariant, the phase height method, h_1, will be adapted to solve for an effective reflection height in the next section. In the following section, an adaptation of the *phase height* method will be discussed.

5.3.3 Differential Phase Height

As discussed in Section , the NDGPS transmitters being used as a signal of opportunity suffer from clock instabilities that cause ramping in the phase data. This is problematic since the possible equivalent reflection height techniques discussed above in Section 5.3.2

are all reliant on phase data. To cope with this problem, a modification has been made to the *phase height* technique described in Equation 5.12. First, envision a propagation scheme, like the one depicted in Figure 5.6, where a transmitter, left, is detected by two receivers, right, at some distance d_1 and d_2 away. Each wave, depicted in the figure as a ray, propagates in a similar path and reflects off the D-region, seen as the blue region above, at some height, h_1 and h_2 respectively, with some angle of incidence, θ_1 and θ_2. An important assumption made here is that the receivers are placed sufficiently far from the transmitter, e.g. approximately 700 km to 1200 km, in order to ensure that only one skywave is propagating.

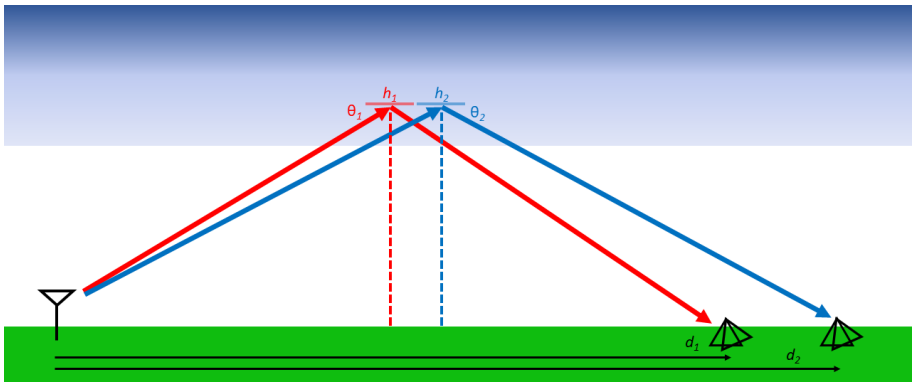

Figure 5.6: Example propagation scheme of a transmitter (left) and two closely spaced receivers (right) with the waves reflecting off of the D-region.

With two receivers, there are now phase measurements at two different locations. This will be the key difference between the *phase height* method described in Equation 5.12 and what will now be called the *differential phase height*. Equation 5.15 describes what happens when the two phase values at each receiver, ϕ_1 and ϕ_2, are subtracted from each other. Each phase value can be broken into three parts: 1) the contribution of the transmitter source ($\phi_{n,source}$), 2) the ionospheric and path contribution ($\phi_{n,ionosphere}$), and 3) the contribution from nearby scattering ($\phi_{n,site}$). Between the two receivers, the contribution from the transmitter source should be identical and thus, when subtracted, should cancel completely, which effectively eliminates the "phase ramping" described above. The remaining phase elements are described in Equation 5.16, where $\phi_{\Delta,ionosphere}$ is the difference in the ionospheric, and path, contribution, ϕ_{noise} is the contribution of any time varying noise

(e.g. receiver noise), and ϕ_{bias} is the contribution of any "constant bias", such as nearby scattering from geographical features or buildings.

$$\phi_\Delta = \phi_1 - \phi_2 = \phi_{1,source} + \phi_{1,ionosphere} + \phi_{1,site} - \phi_{2,source} + \phi_{2,ionosphere} + \phi_{2,site} \quad (5.15)$$

$$\phi_\Delta = \phi_{\Delta,ionosphere} + \phi_{noise} + \phi_{bias} \quad (5.16)$$

In Equation 5.12, the right-hand side can be encased into a variable, such as Equation 5.17. Given the right selection of M, the phase values from Equation 5.16 and Equation 5.17 will be equal, $\phi_\Delta = \phi'_\Delta$.

$$\phi'_\Delta = (2M + 1)\pi + \theta_g \quad (5.17)$$

Thus, we can then substitute Equation 5.16 into Equation 5.12 and solve for the equivalent reflection height, yielding Equation 5.18. Where λ is the wavelength, θ_i is the angle of incidence (in radians), and ϕ_Δ is the phase from Equation 5.16.

$$H = -\frac{\phi_\Delta \lambda}{4\pi \cos\theta_i} \quad (5.18)$$

Next, the metric we are interested in is a *relative change* in phase height, rather than an absolute metric. Thus, the mean phase height, $\bar{H}$, is subtracted, which yields a normalized relative phase height, Δh, as in Equation 5.19. It should be noted that because of this normalization, the integer choice, M, from Equation 5.17 becomes irrelevant. This normalized, differential phase height is the final metric of interest. However, to measure its variation, the *root-mean-squared* of a subset time series of normalized differential phase height values is calculated, using Equation 5.20, to measure the vertical variation in the D-region.

$$\Delta h = H - \bar{H} \quad (5.19)$$

$$\sigma_{RMS} = \sqrt{\frac{1}{N}\sum_{n=1}^{N} |\Delta h|^2} \tag{5.20}$$

The values for the wavelength, λ, and phase, ϕ_Δ, are known, however, the angle of incidence, θ_i, is still an unknown. Assuming a spherical Earth, a formula for the angle of incidence based on the geometry of the problem can easily be solved using Equation 5.21, where R_e is the radius of the earth in meters, h_n is the reflection height in meters, and d_n is the distance from the transmitter to the receiver in meters. The subscript n indicates the receiver number. The resulting angle of incidence, $\theta_{i,n}$, is in radians. The formula on the right hand side is the angle from the vertical axis, the complementary angle of the angle of interest. Thus, the angle is subtracted from $\frac{\pi}{2}$, which yields an angle of incidence that can be used in Equation 5.18.

$$\theta_{i,n} = \frac{\pi}{2} - \arctan \frac{R_e \sin \frac{d_n}{2R_e}}{h_n + R_e(1 - \cos \frac{d_n}{2R_e})} \tag{5.21}$$

In Equation 5.21, there is still one unknown: the reflection height, h_n. However, only the *relative change* in this variable is of interest. Thus, a best guess value for h_n is used and left constant. This approximation results in a small error that decreases as propagation distance increases. For example, if the reflection height is assumed to be 90 km with a nighttime range of reflection heights of $85 - 95$ km for a wave at 300 kHz. For a propagation range of 900 km the error, that is the difference between the chosen value and the bounds, is $\theta_{error,i} \approx \pm 0.6°$.

An additional consideration for the use of Equation 5.18 is that, although there is only one angle of incidence in the formula, there are actually two angles of incidence for the two receivers being used. Two possible solutions to this problem are: 1) to take the mean value of the two angles of incidence, 2) to pick one angle of incidence and use it. In the context of this problem, the receiver spacing is often quite small, $< 10\lambda$, and if it's chosen to be closer to $\approx \lambda$, then the error in the angle of incidence, if only a fixed value is used, drops drastically. At a propagation distance of 900 km, the difference between two receivers spaced one wavelength apart, with identical reflection heights, is only $\theta_{error,i} \approx 0.01°$. Thus,

this error becomes negligible under the right circumstances.

In conclusion, to measure the vertical roughness, or variability, of the D-region the *differential phase height* method described above will be used to track the relative change in phase height. Equation 5.18 is used to calculate the differential phase height using a fixed value of angle of incidence, calculated using Equation 5.21, where an initial reflection height of 90 km is used and kept constant. The resulting value is normalized using Equation 5.19 and then the root-mean-squared value is calculated form a subset of the time series using Equation 5.20. The final metric describes the variability in the vertical phase height between two "patches", Fresnel zones, reflecting off the D-region.

5.4 Horizontal Roughness

The second component of characterizing the electromagnetic roughness of a surface is determining the "horizontal roughness". A common technique for characterizing spatial variability, which can be applied to this problem, is called *cross-correlation analysis*. Variants of this method are widely used to solve problems in different remote sensing fields. The work by *Doviak et al.* [1994], and citations within, used spaced receiver models and cross-correlation analysis to study atmospheric turbulence and wind parameters. A paper by E. N. Bramley, *Bramley* [1951], similar to the paper by *Briggs et al.* [1950], summarizes the use of a cross-correlation analysis technique on the reception of radio waves from the ionosphere for two closely spaced aerial antennas, such as two antennas on an airplane, for various conditions, such as whether there is a steady signal present or not. This work was expanded on by *Lindner* [1975a] and *Lindner* [1975b] to, using the partial reflection technique, understand the angular spread of down coming reflected waves, the coherence ratio, and the scale/size of reflecting ionospheric irregularities. The work by *Wernik et al.* [1983] used spaced receivers to study turbulent ionospheric irregularities, specifically the mean drift velocity and direction, the characteristic random velocity, the spatial scales of the irregularities, and the orientation of the irregularities. Cross-correlation analysis has been successfully used in similar remote sensing fields and can be applied to measure the spatial roughness of the D-region electron density.

The primary metric derived from cross-correlation analysis is the *correlation length scale*. The correlation length scale is a statistical measure that describes the spatial variance of a surface. In the context of this work, the correlation length scale will be used to measure the spatial variance in the amplitude of a wave reflecting from the ionosphere.

It is well established in literature that the correlation length scale measured on the ground can be used as a proxy for the scale of a perturbation or to estimate the angular spread of the scattering from a surface, *Ratcliffe* [1956]. Figure 5.7 shows a propagating ray (red arrows) reflecting off the ionosphere (blue medium). When the ionosphere is smooth, such as in the top panel, the reflection will be *specular* and remain a narrow beam. As the roughness increases, middle and bottom panel, the down coming ray becomes more diffuse and becomes a wider "cone" instead of a narrow beam. Thus, as the roughness of the surface increases in relation to the wavelength being used, the measured correlation length scale of should increase as well.

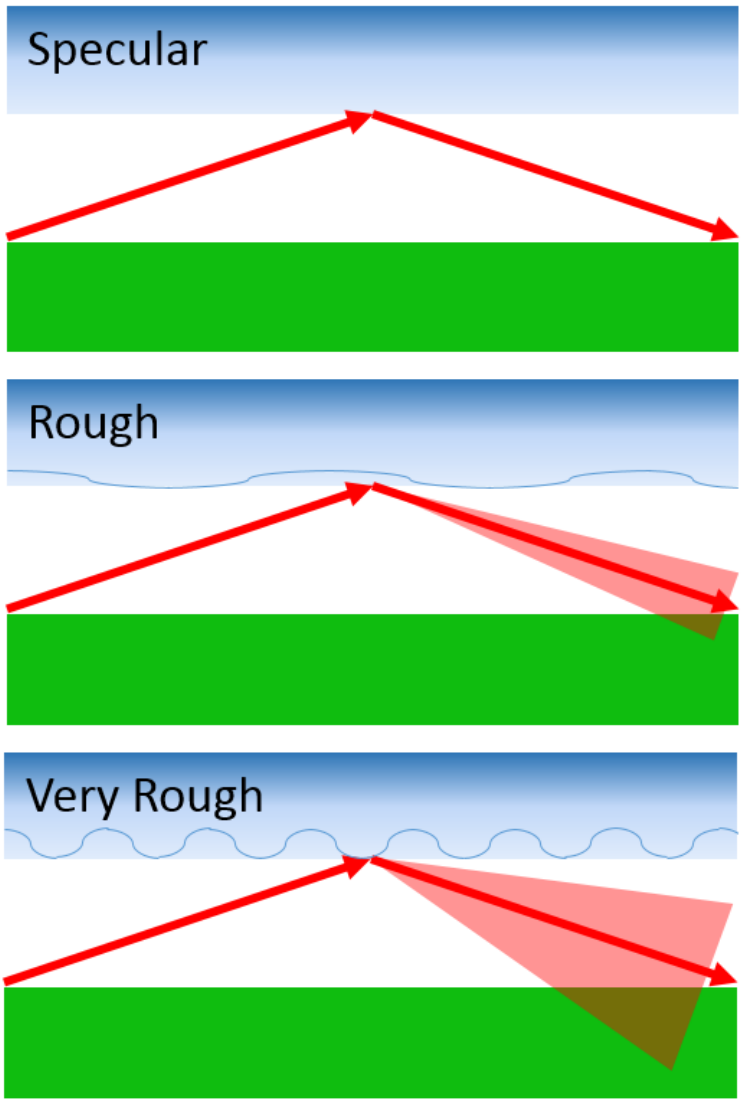

Figure 5.7: Conceptual depiction of the effect of roughness on an electromagnetic wave reflecting from the ionosphere. Top to bottom panel shows smooth to very rough.

The correlation length scale is calculated as follows. First, the simultaneous amplitude data being analyzed (e.g. N/S amplitude, E/W amplitude, major axis length, or minor axis length as per Section 5.3.3) from multiple receivers is aggregated, such as in Equation 5.22, where each variable represents the time series of the metric being analyzed. In this case, the time series may be the complete time series of the data collected during the campaign or a windowed subset of it.

$$\mathbf{x} = [x_1(t), x_2(t), ..., x_d(t)] \tag{5.22}$$

Once the data has been aggregated, the data from each receiver is normalized individually by calculating the *Z-score*, Equation 5.23, where μ_x is the mean and σ_x is the standard deviation.

$$\bar{x} = \frac{x - \mu_x}{\sigma_x} \tag{5.23}$$

Using the normalized values, the cross-correlation is calculated between each pair of receiver metrics using Equation 5.24. Where x_{n+m} is one receiver site metric at time $t = n + m$ and y_m^* is the complex conjugate of the other receiver site metric at time $t = m$. The result from Equation 5.24 is then normalized using Equation 5.25.

$$\hat{R}_{xy}(m) = \begin{cases} \sum_{n=0}^{N-m-1} x_{n+m} y_n^*, & m \geq 0, \\ \hat{R}_{yx}^*(-m), & m < 0. \end{cases} \tag{5.24}$$

$$\hat{R}_{xy,coeff}(m) = \frac{1}{\sqrt{\hat{R}_{xx}(0)\hat{R}_{yy}(0)}} \hat{R}_{xy}(m) \tag{5.25}$$

The result of this calculation is used to find the *maximum* value of the *absolute* value of each receiver pair combination. This results in a diagonal matrix of size $D \times D$ where the diagonal values are equal to approximately 1. Each point in this matrix corresponds to a specific receiver spacing. Figure 5.8 illustrates the receiver spacing configuration for a radial propagation scheme. A transmitter, on the left, is transmitting a wave that reflects off the ionosphere, middle of figure, and is detected by some number of receivers, on the right. The receivers are located at a distance, $d_{1,2,\ldots}$, from the transmitter. The spacing between the receivers can be calculated in two ways: 1) the spacing between the midpoints of the propagation paths, L', or 2) the ground spacing, L. Each element of the calculated diagonal matrix above has an equivalent diagonal matrix with elements corresponding to the spacing using either L' or L. For this work, the ground spacing of the receivers, L, is exclusively used in order to match the simulated results in the next section.

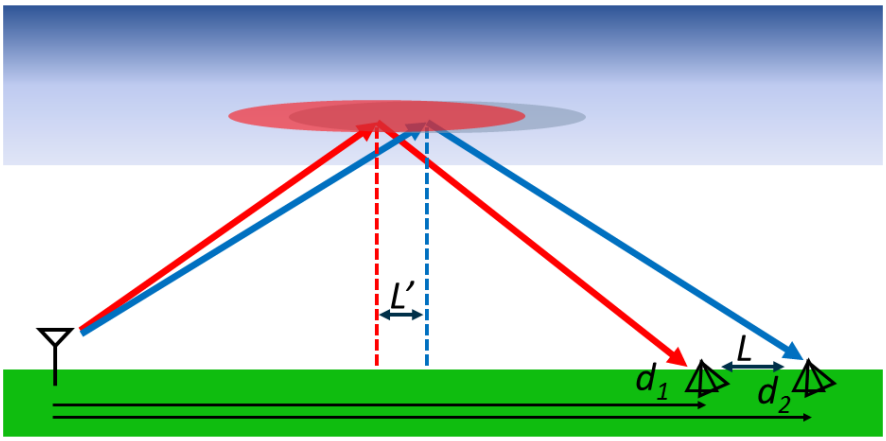

Figure 5.8: Example propagation scheme of a transmitter (left) and two closely spaced receivers (right) with the waves reflecting off of the D-region.

In general, the exact cross-correlation point is not captured, so an exponential fit, like the one in Equation 5.26, is used to approximate it. In Equation 5.26, "A" and "B" are coefficients and generally $A \approx 1$. Figure 5.9 shows an example of this process. The left panel shows the major axis, or H_ϕ, correlation length scale. The blue squares are cross-correlation values each pair of receivers for the entire data set, while the bars are the standard deviation of the windowed data set to highlight the variation. The black line is the exponential fit for the blue squares and the red horizontal line is the e^{-1} point. The point at which these two lines intersect is the correlation length scale. The same plot is shown in the right panel for the minor axis, H_θ.

$$\hat{R}'(x) = A \exp^{Bx} \tag{5.26}$$

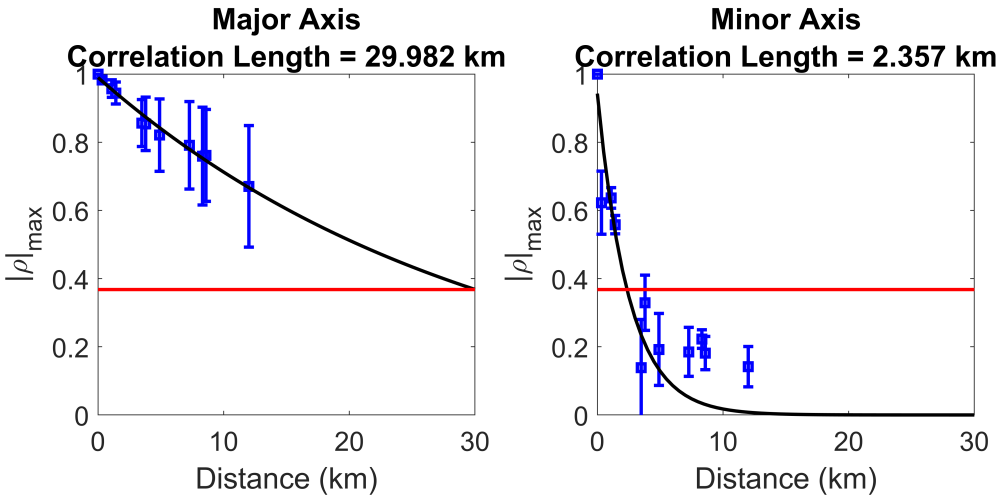

Figure 5.9: Example of estimating the correlation length scale using an exponential fit. The left panel shows the major axis cross-correlation values and the minor axis shows the minor axis values.

A second metric that can be derived from cross-correlation analysis is the *correlation time*. The correlation time, τ, is calculated by finding the lag, or time delay, of the maximum absolute value resulting from the cross correlation between two receivers. From Equation 5.24, this is equivalent to finding the index m corresponding to the maximum absolute value. For a group of D time series, or subsets of the time series, this results in a $D \times D$ diagonal matrix containing the values of the correlation time, where the diagonal values are the correlation time of the auto correlation of each receiver, which should be equal to approximately 0. The correlation time is of less interest than the correlation length scale, however, it could provide insight on the rate of change, or turbulence, in the D-region – a shorter time scale would correspond to a more rapidly changing ionosphere and vice versa.

The work by *Wernik et al.* [1983] used the correlation times and the spacing between receivers to estimate the apparent velocity of plasma irregularities in the ionosphere. An example study from *P. Beckmann and A. Spizzichino* [1963], seen in Figure 5.10, describes using cross-correlation analysis with Medium Frequency (MF, 300 kHz to 3 MHz) and High Frequency (HF, 3 MHz to 30 MHz) waves to study scattering and turbulence in the troposphere. Figure 5.10 depicts the cross-correlation between three sets of receivers spaced at 20 meters, 40 meters, and 60 meters, with the normalized correlation coefficient shown on the y-axis and the lag, τ, shown on the x-axis. There is a decreasing trend in the

maximum correlation between receivers as distance increases, which is expected. As the spacing increases, the correlation time, τ, increases due to winds and turbulence at the altitudes of interest and could be used to deduce some properties about the winds. As a side note, the correlation length scale, as described previously, for this example would occur at approximately 60 meters.

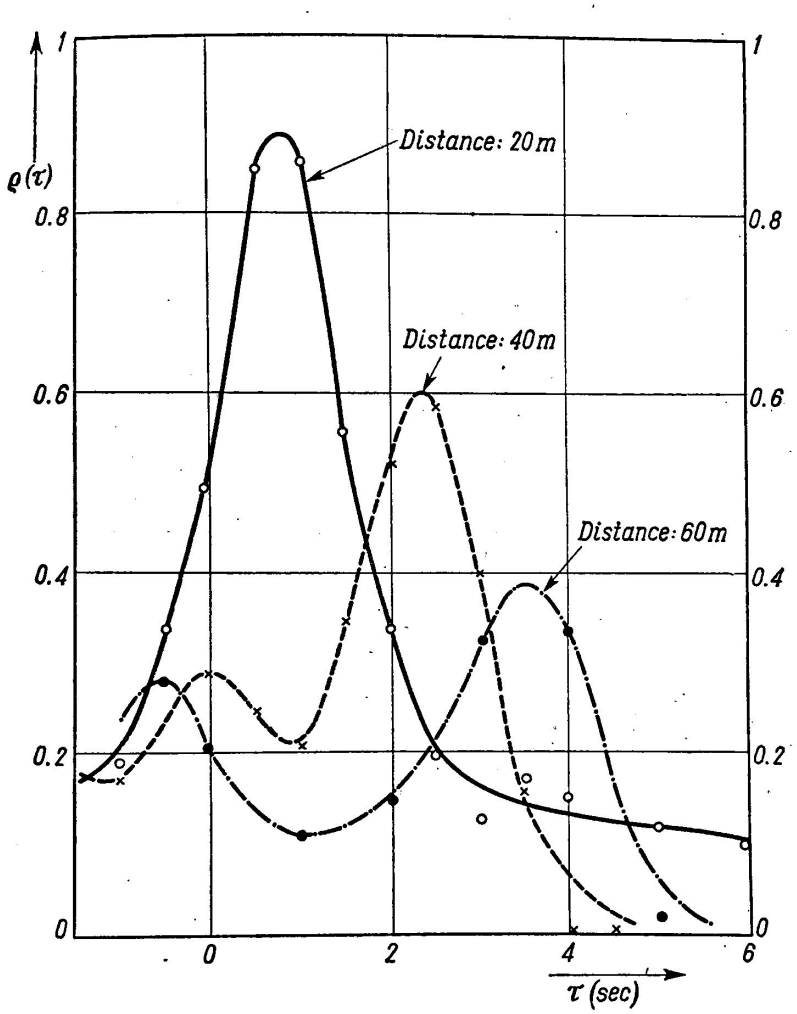

Figure 5.10: Demonstration of the effect of wind on a tropospheric path between four receiving poins. Adapted from *P. Beckmann and A. Spizzichino* [1963].

5.5 Modeling D-Region Roughness

5.5.1 Generating a Rough D-Region

The D-region effectively consists of two levers: 1) electron density, 2) electron-neutral collision frequency. In general, the propagation of LF/MF waves is more heavily impacted by changes in the electron density, so to simplify the problem space only roughness in the electron density will be considered. Using the "Wait and Spies Two Parameter Model", Equation 1.3, the D-region electron density can be parameterized as a function of distance, where roughness is added by varying h' and β using a Gaussian distribution. Figure 5.11 depicts an two-dimensional image of the distribution of h', along the x-axis, and β, along the y-axis, generated for an example rough ionosphere. Both variables were varied using a Gaussian distribution. The h' values were generated with a mean of 85 km and standard deviation of 3 km. The β values were generated with a mean of 0.63 km^{-1} and standard deviation of 0.025 km^{-1}. The color represents the bin count for each pixel, where red is a higher count and blue is a lower count.

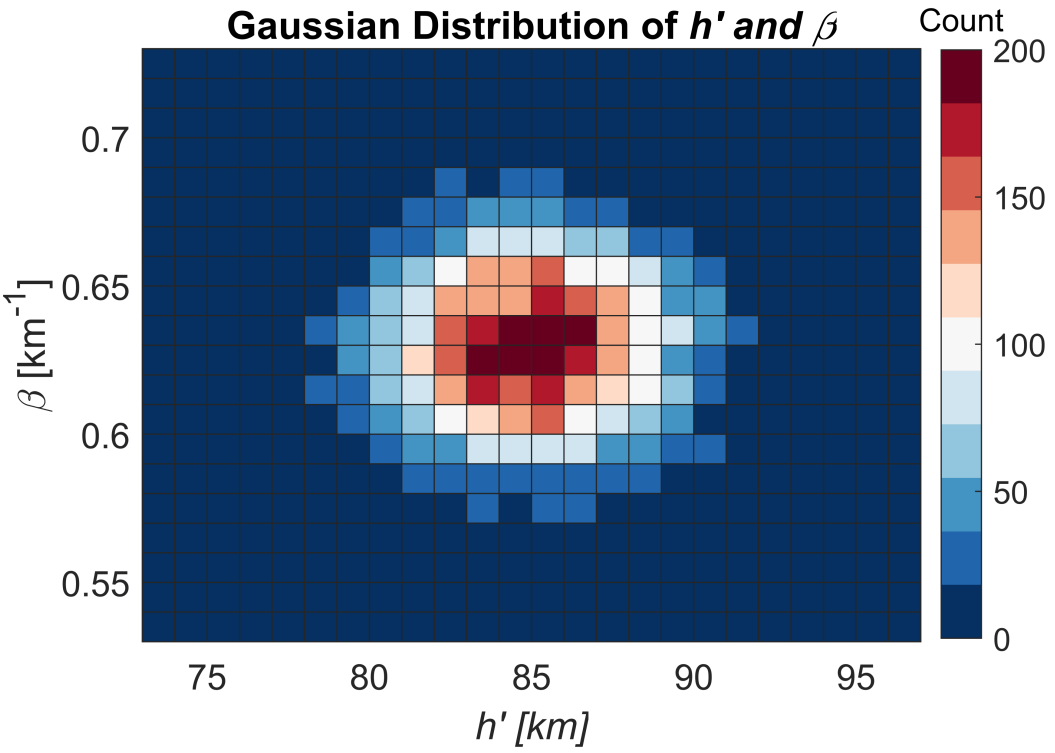

Figure 5.11: Example distribution of h' and β used to generate a randomly rough ionosphere.

This generates a completely random electron density, however, to create varying scales of roughness, an additional parameter must be added. This "roughness parameter", henceforth referred to as the *ionospheric length scale*, is a two-sided exponential smoothing window. One side of the window is generally describe by Equation 5.27 where α is the resulting window, x is the horizontal width of the window in kilometers, and L_{iono} is the ionospheric length scale in kilometers. As L_{iono} increases, the smoothing window width increases, and the fine features of the roughness get flatted. Once the exponential smoothing is done to the original electron density profile, the resulting D-region profile is used in modeling. Figure 5.12 depicts this process. The top panels describe the steps, while the bottom panels graphically depict an example. The bottom left panel shows the completely random electron density profile along some two-dimensional path. The bottom center panel shows the two-sided exponential smoothing widow described by the ionospheric length scale parameter. This exponential window is applied to the bottom left panel to generate the bottom right panel – the electron density profile with a parameterized roughness.

$$\alpha = \exp^{-x/L_{iono}} \tag{5.27}$$

Figure 5.13 depicts four different rough D-region electron densities generated using the method described in Figure 5.12. Each panel of Figure 5.13 is generated using a different ionospheric length scale using Equation 5.27. As the ionospheric length scale increases from 5 km to 30 km, finer perturbations become smoothed and the overall size of the perturbations, in regard to wavelength, increase. Note that each panel uses a different randomly generated D-region electron density with the same statistical characteristics.

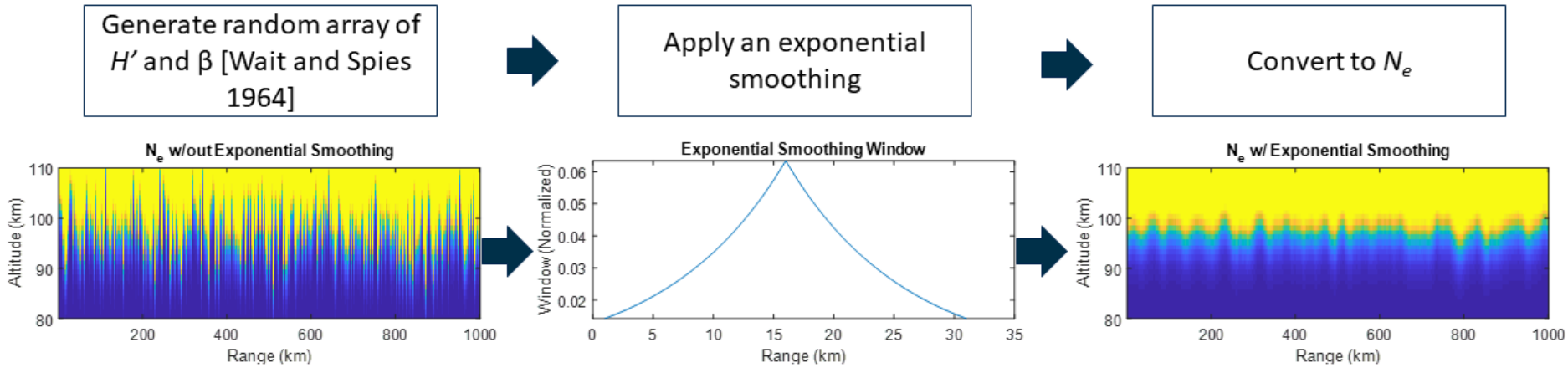

Figure 5.12: Top row: An outline of the process used to generate a two dimensional rough D-region electron density profile with a parameterization for the roughness. Bottom row: Example figures that coincide with the steps in the top row.

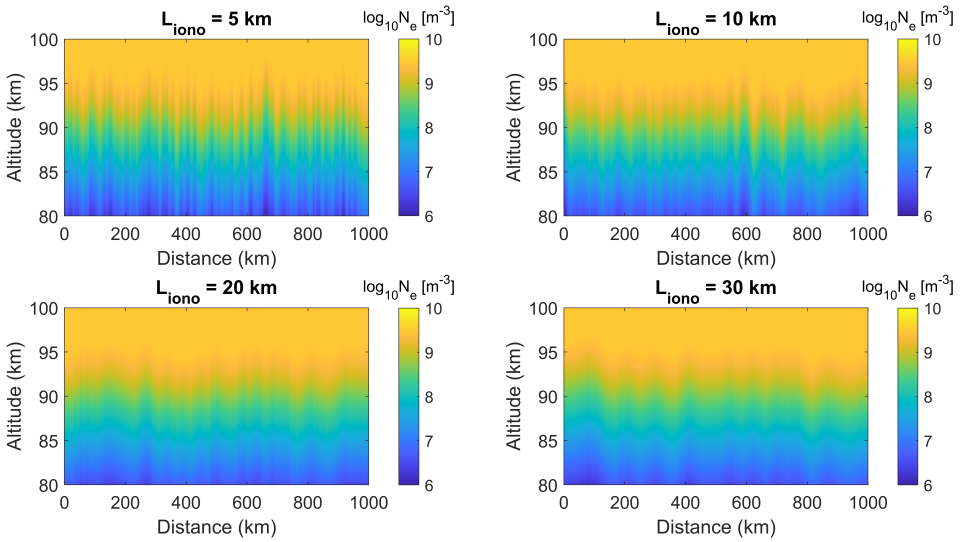

Figure 5.13: Example rough D-region electron density profiles with varying ionospheric length scales, L_{iono}. Each panel is derived from a different randomly generated electron density distribution.

5.5.2 The Monte Carlo Method (MCM)

To model a randomly varying rough D-region, a Monte Carlo Method (MCM) will be employed. This practice, often referred to in literature as "stochastic modeling", is a common tool used to study the scattering from randomly varying surfaces, e.g. *Hastings et al.* [1995]. The motivation for using the MCM is to derive a "direct" measure of the D-region roughness using the correlation length scale measurement.

Figure 5.14: Outline of the Monte Carlo Method used in this work. Starting at 1 and moving to 3. The circle diagram represents that this is an iterative approach.

Figure 5.14 depicts the general flow of the MCM method used. First, the input parameters, in this case the electron density (N_e) of the D-region described by h' and β, is randomly varied for N instances. The rough D-region electron densities are generated as discussed in the previous section and the ionospheric length scale is held constant while generating the N instances. Once all the instances of the rough D-region electron density are generated, the FDTD model is used to model the effect on LF/MF propagation. Figure 5.15 summarizes the FDTD output of a set of runs with $N = 21$ for an ionospheric length scale, L_{iono}, of 10 km. This figure depicts the differential ground interference pattern of the magnetic field, which is calculated by subtracting the mean of all interference patterns from each individual one. This metric is used to highlight the variation between runs caused by varying the D-region roughness. The horizontal axis is the distance from the transmitter in kilometers and the vertical axis is the run number. The color of the figure, defined by the color bar on the right-hand side, is the differential magnetic field amplitude in decibels, dB. There is no noticeable variation in the magnetic field amplitude until around 850 km from the transmitter when the first skywave becomes the dominant mode present. Figure 5.16 shows the same data as Figure 5.15, but zoomed in to highlight the region of variation from 840 km to 1000 km. The pronounced "line" seen at around 860 km is due to a null in the ground interference pattern moving and is the most significant difference between the

runs. However, there is also random variation from 860 km to 1000 km, suggesting that information about the electron density roughness is being captured in the amplitude data.

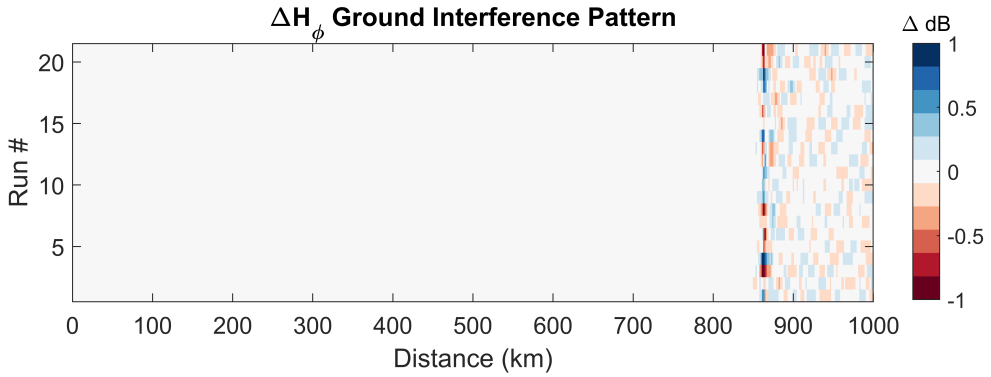

Figure 5.15: Example output from successive FDTD runs using the Monte Carlo Method in units of differential magnetic field amplitude of the H_ϕ component, where $L_{iono} = 10km$ and the transmitter frequency is 293 kHz.

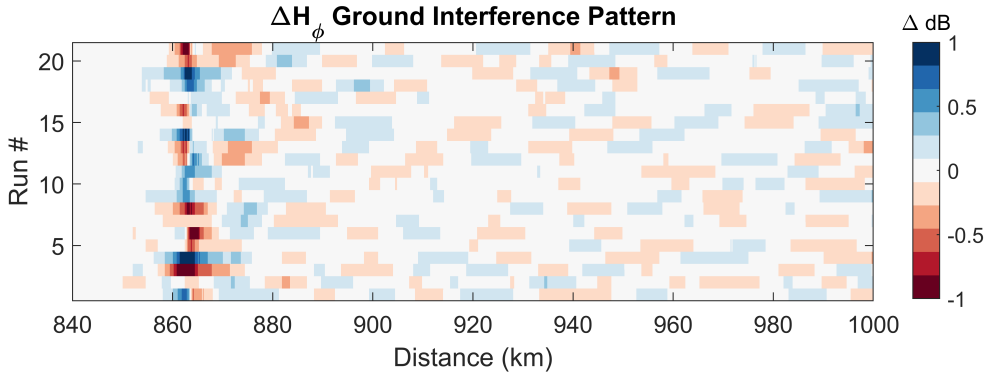

Figure 5.16: Zoomed in example output from successive FDTD runs using the Monte Carlo Method in units of differential magnetic field amplitude of the H_ϕ component, where $L_{iono} = 10km$ and the transmitter frequency is 293 kHz.

Finally, the N runs, such as those shown in Figure 5.15 and Figure 5.16, are aggregated together and the statistics of the problem can be analyzed. Specifically, the correlation length scale is of interest here. As described in Section 5.4, the correlation length scale is calculated by treating a single distance, m, across all N runs as a single time series. Then, "stepping" away from the first distance, m, the cross-correlation is calculated between each "time series". In *MATLAB*, the first step is to normalize the data by calculating the "Z-score" of each time series using Equation 5.28, where μ_x is the mean of the time series x and σ_x is the standard deviation. Next, the cross-correlation is calculated using the

xcorr function in *MATLAB*. This function is described by Equation 5.29, where x_n and y_n are the random processes of interest. A *coefficient normalization*, Equation 5.30, is then applied to Equation 5.29. The use of these equations results in a function that describes the correlation versus distance, which can be carried out until the correlation equals $1/e$, which is the modeled, or estimated, correlation length scale. Figure 5.17 shows an example result from this procedure. The x-axis is the distance. The y-axis is the cross correlation between $m = 840$ km and each successive distance. The dashed red line indicates the $1/e$ lines and the red circle shows the point at which the correlation crosses this line. L_{iono} is the ionospheric length scale as discussed in the previous section. L_{est} is the estimated correlation length scale.

$$\bar{x} = \frac{x - \mu_x}{\sigma_x} \tag{5.28}$$

$$\hat{R}_{xy}(m) = \begin{cases} \sum_{n=0}^{N-m-1} x_{n+m} y_n^*, & m \geq 0, \\ \hat{R}_{yx}^*(-m), & m < 0. \end{cases} \tag{5.29}$$

$$\hat{R}_{xy,coeff}(m) = \frac{1}{\sqrt{\hat{R}_{xx}(0)\hat{R}_{yy}(0)}} \hat{R}_{xy}(m) \tag{5.30}$$

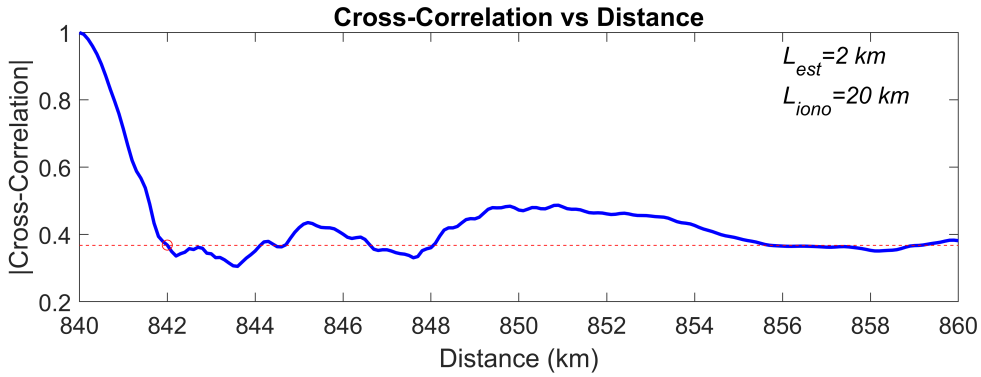

Figure 5.17: Example of calculating the modeled correlation length scale using an $L_{iono} = 20$ km and a frequency of 293 kHz.

To generate meaningful results, the process in Figure 5.14 must be repeated for several ionospheric length scales for the same propagation path. Then the entire M-by-N, where

M is the number of distance bins and N is the number ionospheric length scales, can be treated as a "look-up table" for that specific propagation path, such as that in Figure 5.18. Figure 5.18 serves to connect the measured correlation length scale with the ionospheric length scale as a function of distance and modeled correlation length scale. The left panel shows the full two-dimensional image for some modeled propagation path from 500 km to 900 km, y-axis, for ionospheric length scales ranging from 5 km to 50 km, x-axis. The color represents the estimated correlation length scale using the method described above. The hypothesis is that the modeled correlation length scale can be match with the measured correlation length scale and serve as a proxy for the ionospheric length scale. The right panel shows three "horizontal" slices of the left panel for the distances of 600 km (blue), 700 km (red), and 900 km (black). The x-axis shows the ionospheric length scale and the y-axis shows the estimated correlation length scale. There are two key trends to note from the right panel. First, for each line, or distance, there is an upward trend from left to right in a near $f(x) \propto \sqrt{x}$ fashion. This indicates that as the ionospheric length scale increases, the correlation length scale will also increase and approach some limit. The second trend is that between distances, i.e. the different color lines, the rate of increase and the "limit" reached grows with distance. For example, the black line, 800 km from the transmitter, grows much more rapidly and approaches an estimated correlation length scale of 7 km for an ionospheric length scale of 50 km. While the blue line, 600 km from the transmitter, grow much less rapidly and approaches a correlation length scale of 4 km for an ionospheric length scale of 50 km. A possible reason for the increase in the ionospheric length scale with distance is due to the increasing contribution of the first skywave as the distance increases away from transmitter. As the contribution of the first skywave grows in comparison to the other modes, e.g. the groundwave or high order skywaves, the detected signal variation, i.e. the estimated correlation length scale, will change more drastically from irregularities in the D-region electron density.

5.5.3 Method Validation

In order to validate the outlined method, two things must be determined: 1) what is the minimum number of runs needed to generate stable results, 2) what is the sensitivity of the

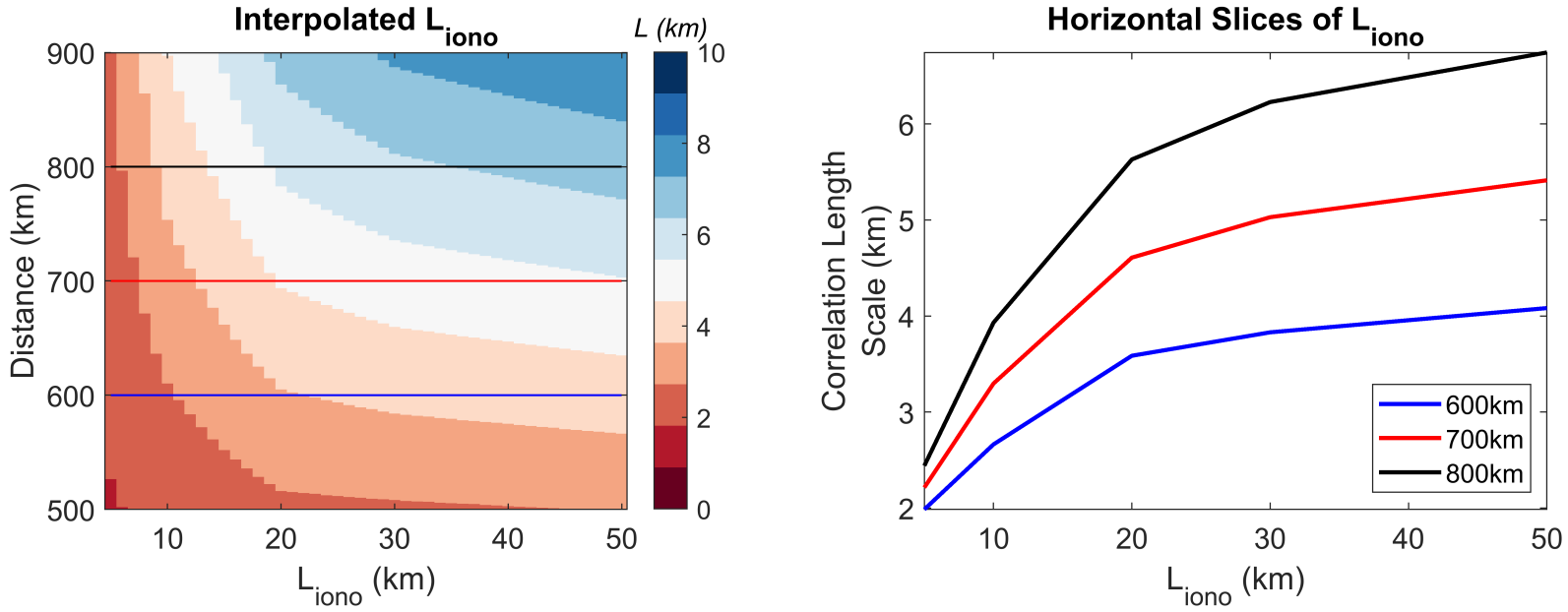

Figure 5.18: Left panel: A two-dimensional image depicting the relationship between the ionospheric length scale, the estimated correlation length scale, and the distance from the transmitter for a 293 kHz source. Right panel: Three horizontal slices of the left panel depicting three individual distances and the relationship between ionospheric length scale and estimated correlation length scale.

method to the mean values of h' and β. The minimum size the "time series" needed in order to find a stable solution was empirically determined to be approximately $N \geq 40$. Figure 5.19 shows the process of how the minimum time series size was empirically determined. The x-axis contains the number of Monte Carlo runs used in the time series to generate the cross-correlation plot, which is shown as the y-axis. The first column was generated using two runs and the final column was generated using 55 MCM runs. The starting point of the cross correlations is at 720 km and extends to 740 km. Each "slice" or column in the figure can be thought of as an individual version of Figure 5.17. The color in the figure represents the correlation, where the correlation length scale is captured at $\frac{1}{e} \approx 0.367$ or the second lightest shade of red. The correlation length scale appears using around 13 runs, however, the features, including the deep null at 730 km, appear to stabilize starting at approximately 40 runs. Specifically, as the number of runs approach 40, the correlation length scale stabilizes, whereas at 14 runs it is at approximately 730 km instead of about 727 km. Thus, $N \geq 40$ was found to be the minimum number of runs needed in order to determine a stable correlation length scale.

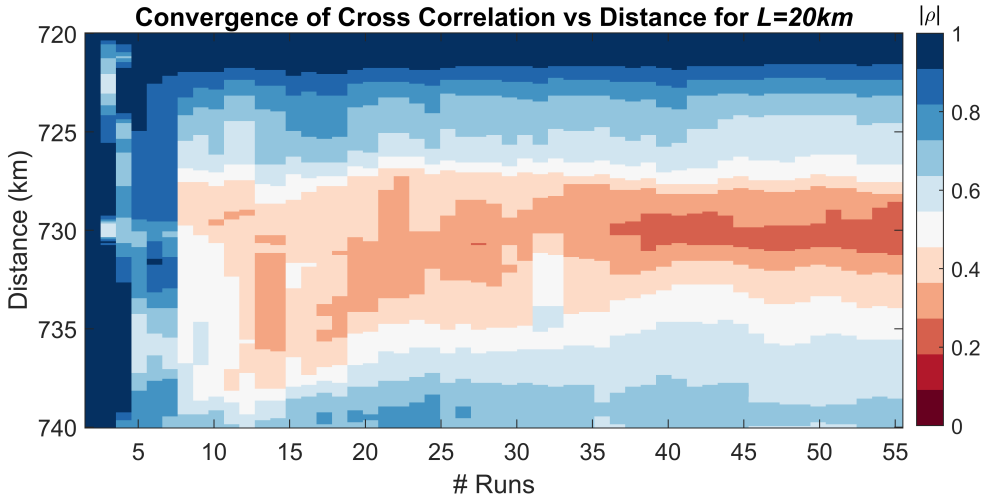

Figure 5.19: Image showing the convergence of the estimated correlation length scale to a stable solution using an ionospheric length scale of 20 km and a frequency of 293 kHz.

The second thing that must be validated is the sensitivity of the modeled correlation length scale to the mean values of h' and β. An assumption critical to simplifying the dimensionality of the problem is that, since the correlation length scale is a "normalized"

or relative metric, it is insensitive to a constant bias in the variables used, namely h' and β. If, however, that is not the case, then two additional dimensions would need to be added to Figure 5.18 – one for the change in the mean value of h' and the other for β. This simplifying assumption was validated empirically. Figure 5.20 summarizes the results of the empirical validation. The figure shows two histograms with varying mean values as indicated by the legend in the top right corner. The blue histogram has a $\bar{h'} = 85$ km and $\bar{\beta} = 0.63$ km^{-1} and the clear histogram has a $\bar{h'} = 80$ km and $\bar{\beta} = 0.5$ km^{-1}. The former being typical nighttime values validated for VLF signals using the LWPC (Long Wave Propagation Capability) Code, *Thomson et al.* [2007]. Each histogram was constructed by using $L_{iono} = 20$ km and calculating the estimated correlation length at each distance from 500 km to 900 km, which generally coincide to the distances of interest. The resulting estimated correlation lengths for both cases were then displayed as a histogram to compare the distribution of the results. From Figure 5.20, it is evident that the two histograms match with minimal deviation from each other. Because there is no drastic difference in the median (4.83 km versus 5.31 km respectively) or standard deviation (3.74 km versus 4.02 km respectively), any slight deviation may be explainable by the randomly generated electron densities. Thus, from this empirical analysis, the simplifying assumption that the mean values of h' and β, at least for the nighttime D-region, can be treated as fixed seems appropriate.

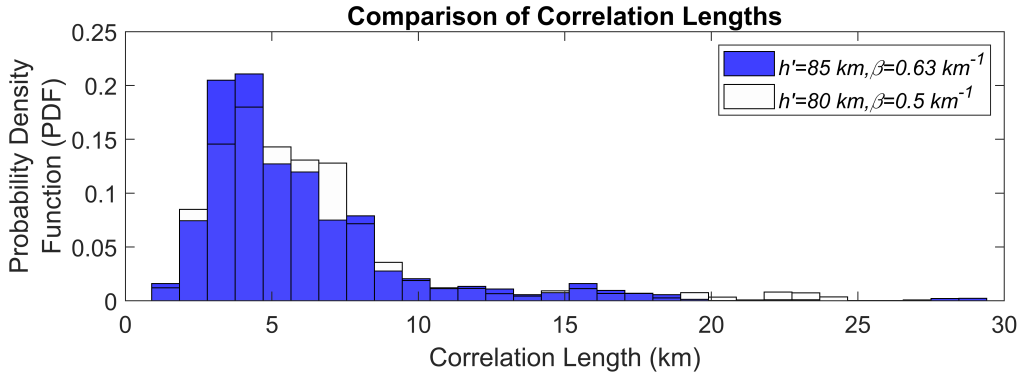

Figure 5.20: Empirical validation of the sensitivity of the correlation length to the mean value of h' and β used to generate randomly rough electron densities. Both distributions use an $L_{iono} = 20$ km and a frequency of 293 kHz.

CHAPTER 6
MEASURING D-REGION ROUGHNESS

This chapter summarizes the field campaign efforts to measure the roughness metrics described in the previous chapter and discusses the results. First, initial, unsuccessful, field campaigns will be described, followed by the data collection improvements and hardware modifications that enabled a series of successful field campaigns. The non-stationarity of the D-region is addressed and an appropriate window size is determined. Next, using the selected window size, the horizontal and vertical roughness metrics from the field campaigns are summarized and discussed. The roughness metrics from an NDGPS and VLF transmitter with similar paths are compared to investigate the variation with frequency. Next, the observed horizontal roughness metrics for two propagation paths are compared to modeled results. Finally, suggestions for future field campaigns are discussed.

6.1 Summary of Field Campaigns

6.1.1 Previous Measurements

Initial attempts done to measure the roughness of the D-region were unsuccessful, but the lessons learned guided future measurements. Two separate data campaigns were attempted: 1) near Delaware [39.9472° N, 75.5813° W] on 23-March-2017, 2) near Juneau [58.5906° N, 134.9041° W] on 27-April-2017. These previous measurements were done by utilizing one permanent receiver site and one mobile site. Data at the mobile site was recorded in 30-minute increments. Although this gave two measurements that could be cross correlated with each other, each set of measurements could not be truly compared to each other because it cannot be assumed that the ionosphere is stationary on the timescale of hours, which prevented an accurate measurement of the correlation length scale. Figure 6.1 depicts this phenomena. The left panel of the figure shows the Fresnel zone, the region of dominant influence for the first skywave, as the gray ellipses for the two sites. The background represents some theoretical total electron density for the D-region. The right panel shows

a second measurement, where the two sites have been moved further away, depicted by the Fresnel zones moving apart, as done in the two experiments in Delaware and Juneau. Since the ionosphere has changed significantly since the previous measurement, it can be assumed that the properties of roughness may have also changed. This implies that, when trying to solve for the correlation length scale, simply doing a cross-correlation between two sites and moving them apart to fit a curve to correlation versus distance would not work since the ionosphere itself is no longer the same. Thus, several measurements need to be done simultaneously to correctly measure the correlation length scale. The second reason that the measurements failed will be discussed in the proceeding section.

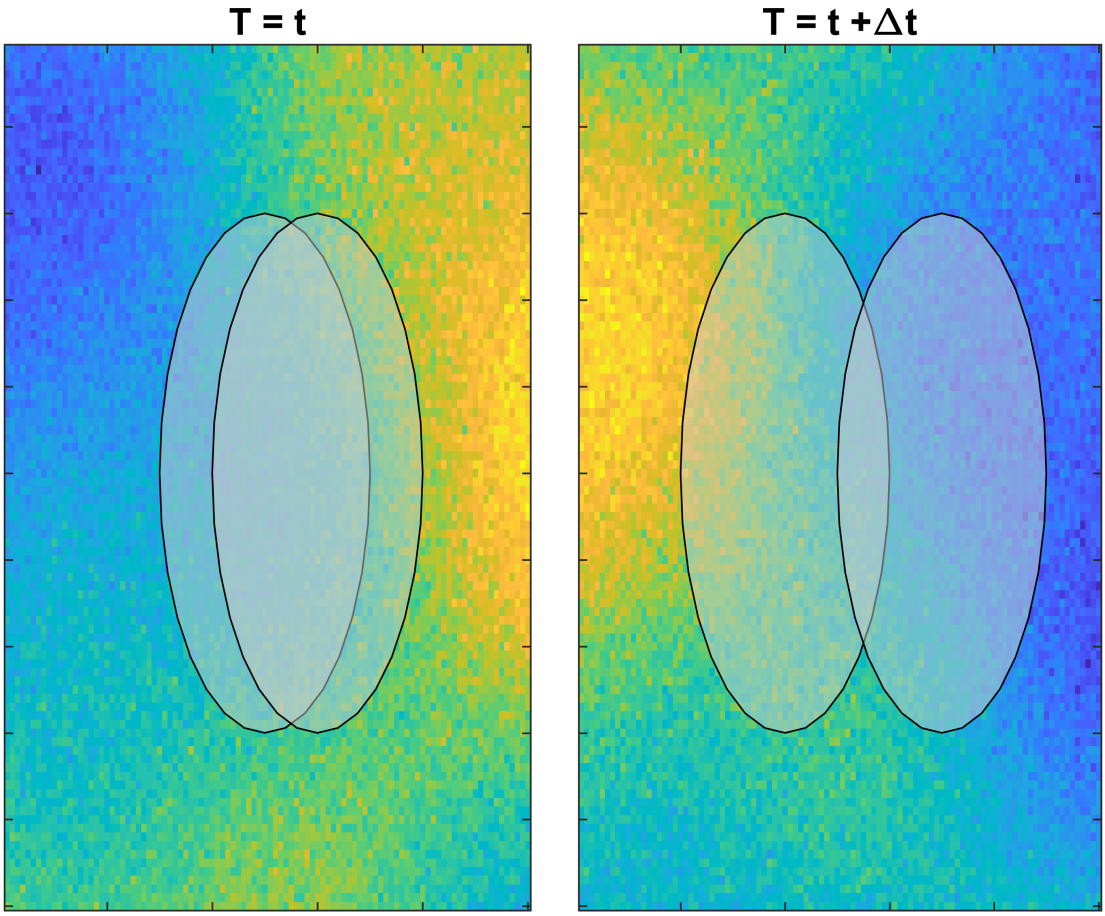

Figure 6.1: Depiction of the first Fresnel zone for two transmitter-receiver paths projected on a synthetic ionosphere shown as the gray ellipses. The background color represents some value for total electron density for the D-region. The left panel shows a measurement for some time, t, and the right panel for a later time, $t + \Delta t$, when the two sites are moved away from each other.

6.1.2 Receiver Hardware Modifications

The LF AWESOME Receiver discussed in Section 1.3 was designed as a stationary, permanent receiver, which proves difficult to use in the field. The initial measurements described in the previous section were done using an off-the-shelf car battery power inverter, such as the one shown in Figure 6.2, which resulted in harmonics saturating the spectrum and severe degradation in the signal-to-noise ratio (SNR). To streamline future field measurements, two objectives need to be accomplished: 1) the receiver needs a low noise, robust DC-to-DC converter, and 2) the receiver system needs to be portable and easy to setup and take down.

Figure 6.2: Example of an off-the-shelf car battery DC-to-AC inverter.

To achieve the first object, a suitable off-the-shelf part was identified – the *PYB30-Q24-D15-H-U* isolated DC-to-DC converted by CUI, Inc. This device has an input DC range

of $9 - 36$ V_{DC} and outputs two channels with ± 15 V_{DC} and 1 Amp of current, which is adequate to power the line receiver. The DC-to-DC converter is mounted on the back of the line receiver chassis (the blue box), as seen in Figure 6.3a, a cabling harness is then used to connect the device to the two power sockets in the line receiver – one on the printed circuit board (PCB) located near the device (seen by the yellow box in Figure 6.3c) and one on the front of the chassis. Figure 6.3b shows the front of the chassis. Two cables are fed through openings. The cable on the left is powering the "NI-DAQ", a National Instruments analog-to-digital converter, and the cable on the right connects to a car battery. Figure 6.3c shows an overview of the modified line receiver connected to a car battery with the lid of the chassis removed. A major benefit of the modified line receiver is its versatility since it can easily be converted back to a wall outlet powered system by swapping the connectors shown in the yellow box of Figure 6.3c.

(a) Mounted DC-to-DC Converter

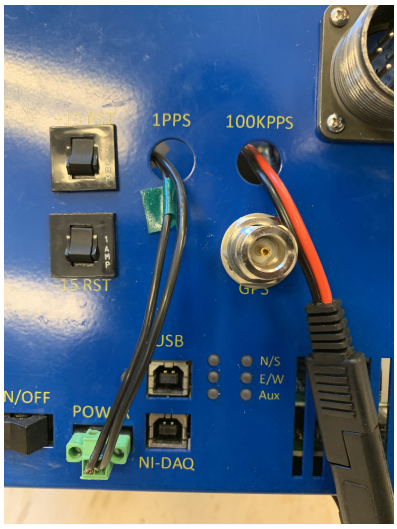

(b) Front Panel

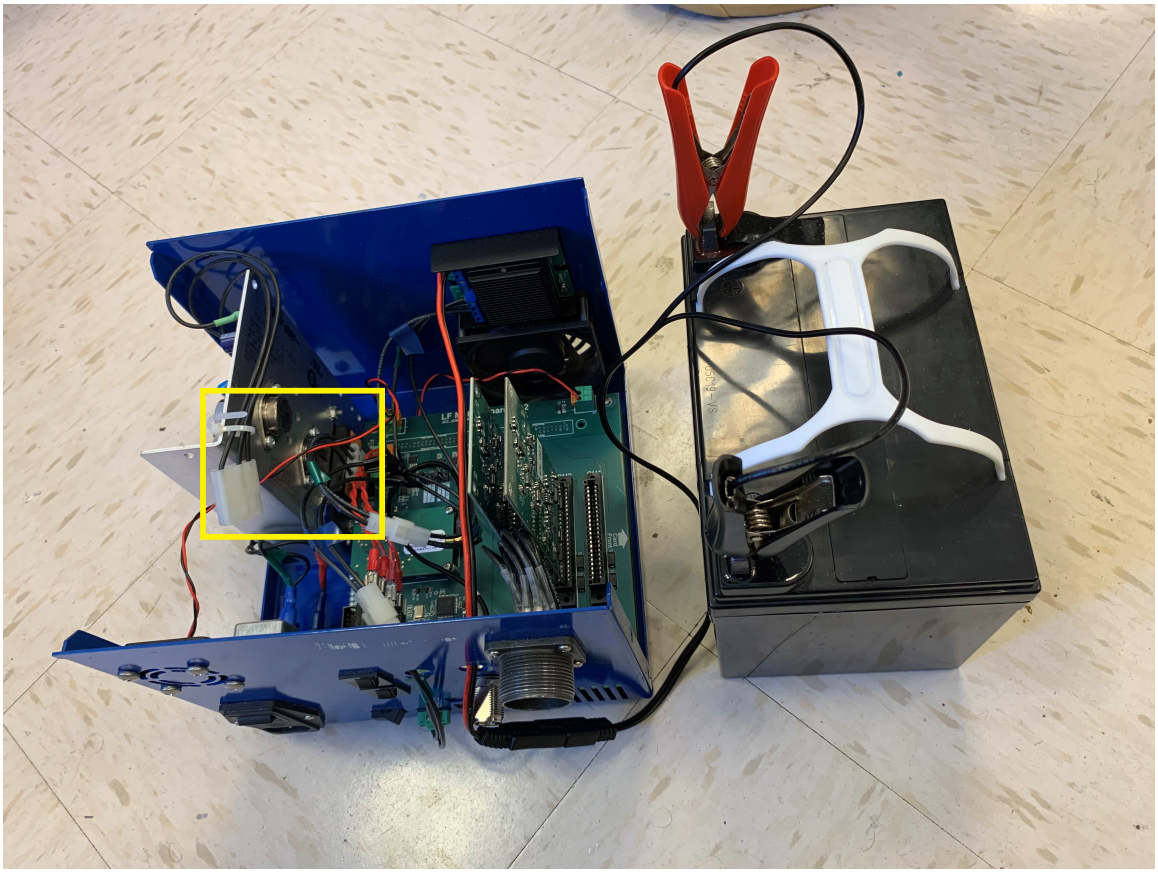

(c) Modified system connected to a car battery

Figure 6.3: The modified LF AWESOME Receiver (line receiver).

Figure 6.4 summarizes the results from a bench top test of the ambient noise from the

three different methods of powering the line receiver. The figure contains four panels, each showing a 10-second spectrogram, in dB-scale, of the full 0-500 kHz frequency range for a modified receiver under different scenarios. The top left panel shows the spectrum for a receiver powered by a wall outlet and serves as a reference for the spectrogram of a quiet power source. The top right panel shows the spectrogram of a receiver plugged into the wall with the powered DC-to-DC converter operating beside the receiver. The bottom left panel shows a modified receiver powered from the DC-to-DC converter. The bottom right panel shows a line receiver powered from an off-the-shelf car battery inverter. A stark difference can be seen between the bottom right, the battery inverter, and the other three panels. The thick red horizontal lines are harmonics generated by the inverter, which greatly degrade the SNR and disrupt the detection of a signal at a frequency near the harmonics. It is evident from this figure that the DC-to-DC converter (bottom left) is lower noise than the car battery inverter (bottom right) and operates at a comparable noise level as a system being powered by a wall outlet (top left).

The second objective is to create a standardized "mobile kit" to enable rapid deployment of the modified LF AWESOME Receiver system in the field. Figure 6.5 shows an example of the mobile kit created to conduct the field campaigns. Each kit is packed in a lightweight Pelican Air and contains the line receiver, a signal cable, a pre-amplifier box, two antennas, a GPS antenna, a GPS cable, a case with assorted cables (e.g. USB cables, battery connectors, etc.), an AGM (absorbent glass mat) deep-cycle lead acid battery, a laptop, and a laptop battery extender. The only equipment needed that can't be packed in the Pelican case is the PVC antenna mast, such as the one shown in Figure 6.6, which is stored disassembled and held together using carrying straps. Since the fully constructed PVC mast cannot fit inside a car or van, the mast is assembled in the field prior to use and disassembled when the measurements are completed. The maximum data collection time for each mobile kit is dependent on the capacity of the laptop battery, the battery extender, and the AGM battery. Empirically, it was found that a 10 Amp-Hour battery lasted about $3-4$ hours. An AGM battery with a 35 Amp-Hour capacity and a laptop battery extender was found to be adequate to collect a full night (about $6-8$ hours) of data. Figure 6.6 shows an example of the mobile receiver system being used in the field to collect data during a field campaign.

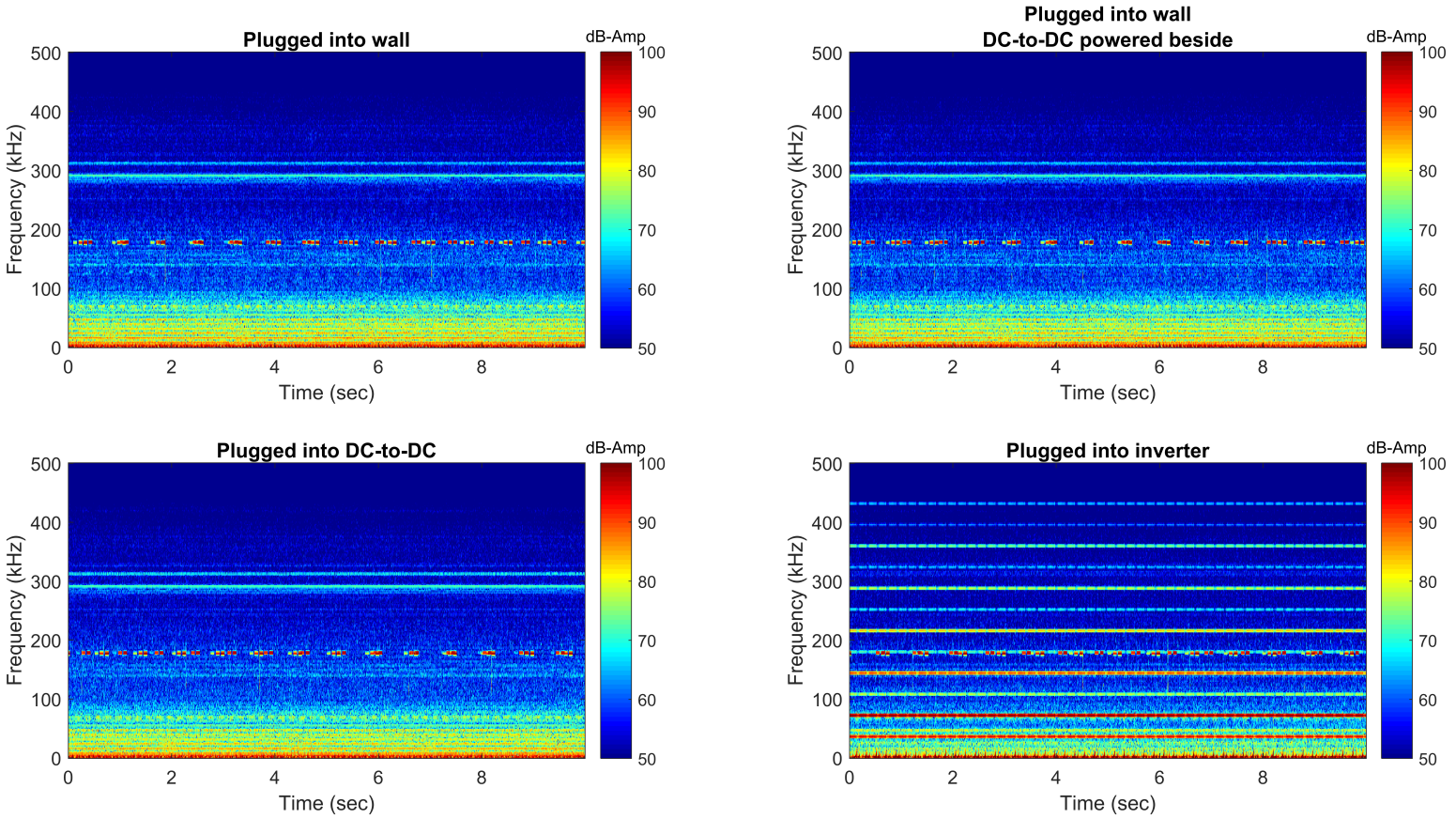

Figure 6.4: Results from bench top test of the ambient noise of three power sources in four configurations.

Figure 6.5: Example of a packed "mobile kit" using a Pelican case, which contains all necessary equipment to deploy a mobile receiver except for the antenna mast.

Figure 6.6: Example of a "mobile kit" being used in the field to collect data.

6.1.3 Field Campaigns

The D-region is non-stationary and fluctuates on a very quick timescale at nighttime, e.g. 5−25 minutes. Early partial reflection measurements had difficulty dealing with this issue when using amplitude statistics to study D-region scattering, *Hocking* [1987]. Thus, receiver spacing and geometry, i.e. simultaneous spatial sampling of the ionosphere, will be critical in accurately measuring the roughness of the D-region. Two primary considerations will have to be taken into account: 1) measurements should be oriented transverse or radial to the propagation path with little deviation, 2) the transmitter-receiver propagation distances should be limited to approximately 600−1200 km to fall in the propagation region dominated by the first skywave, see Chapter 1.4.

Table 6.1: Summary of the field campaigns conducted in 2019 where the spacing from reference is the distance between each receiver site from a fixed reference and the total time refers to the total time of simultaneous data collection.

Date	Number of Receivers	Spacing from Reference (km)	Total Time (Hours)
01/14/19	3	2.5, 5	0.777
01/14/19	3	5, 10	0.540
06/13/19	3	2.5, 5	0.432
06/13/19	3	2.5, 1.4	0.684
08/22/19	4	7.2, 1.4, 4.9	1.504
09/06/19	3	1.4, 4.9	3.983
09/07/19	5	7.3, 8.3, 8.6, 12	5.893

With the above considerations, several field measurements were made over the course of 2019. In each field campaign, some number of mobile receivers were deployed sequentially in a predetermined location, with permission from the property owner, such as a farm, and data was collected for some period. The data collected at each site is truncated to maximize the simultaneous data. Table 6.1 summarizes the completed field campaigns, where spacing from reference indicates the distance from a chosen reference site. All the field campaigns were conducted near the permanent receiver site located at Baxley, Georgia, [31.8767° N, 82.3620° W] indicated by the blue dot in Figure 6.7. This site is located at the "bottom" of what is called the *Southeast Array*, indicated by the black dots in the figure. The red dots in Figure 6.7 indicate the location of each transmitter used for this work. The red lines show the great circle paths (GCP) from the transmitter to the permanent receiver site in Baxley (GA). Table 6.2 summarizes the red transmitter-receiver paths shown in the figure, where the distances listed are from the transmitter to the permanent Baxley (GA) receiver. The receivers were arranged in a predominantly North-South orientation to capture data from several transmitters in a combination of "radial" and "transverse" paths, as depicted in Figure 6.8 where the arrow indicates the direction towards the transmitter being detected. As an example, Figure 6.9 shows the receiver configuration from the 22-August-2019 field campaign where the blue pins indicate the mobile sites and the yellow pin indicates the

permanent receiver site.

Table 6.2: Summary of the transmitters and transmitter-receiver path geometries from the completed field campaigns.

Transmitter	Coordinates	Frequency (kHz)	Distance (km)	Orientation
Detroit (MI)	42.2972°N, 83.0952° W	319	1158.3	Radial
English Turn (LA)	29.8783°N, 89.9417° W	293	757.7	Transverse
Tampa (FL)	27.8502°N, 82.5325° W	312	446.6	Radial
Card Sound (FL)	25.4317°N, 80.4663° W	314	737.9	Radial

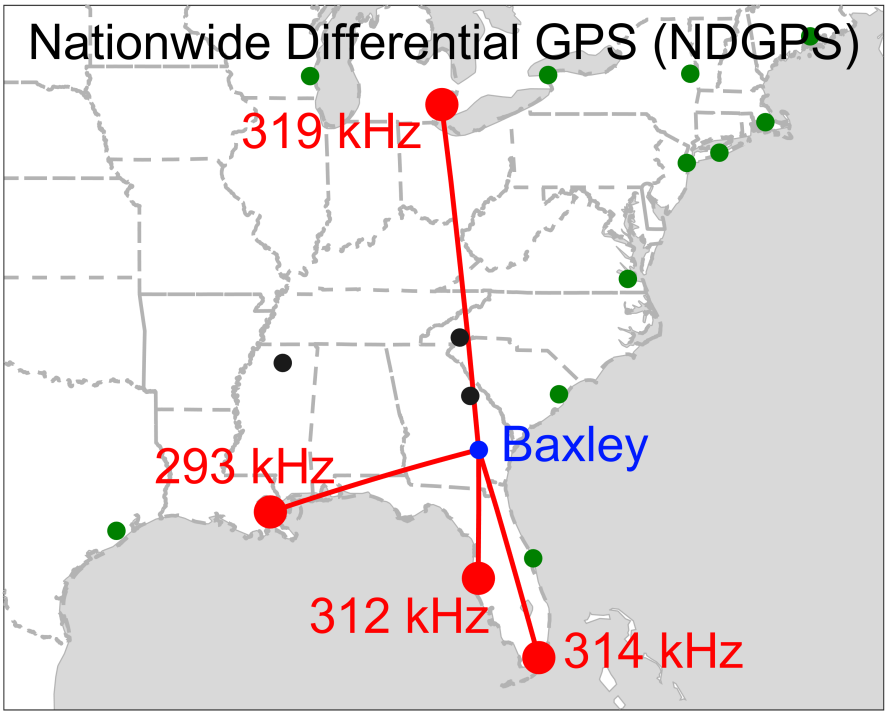

Figure 6.7: Map showing the transmitter-receiver paths for the completed campaigns. The receiver site is indicated by the blue dot and label. The transmitters are shown using the red dots, annotated with the respective transmission frequency.

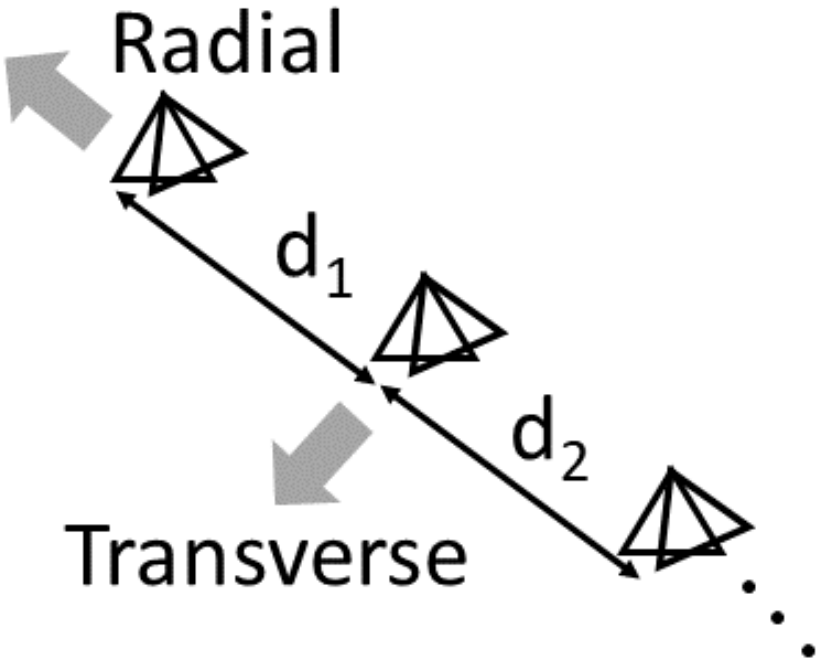

Figure 6.8: Orientation reference for the spaced receivers where the arrow indicates the direction towards the transmitter being detected.

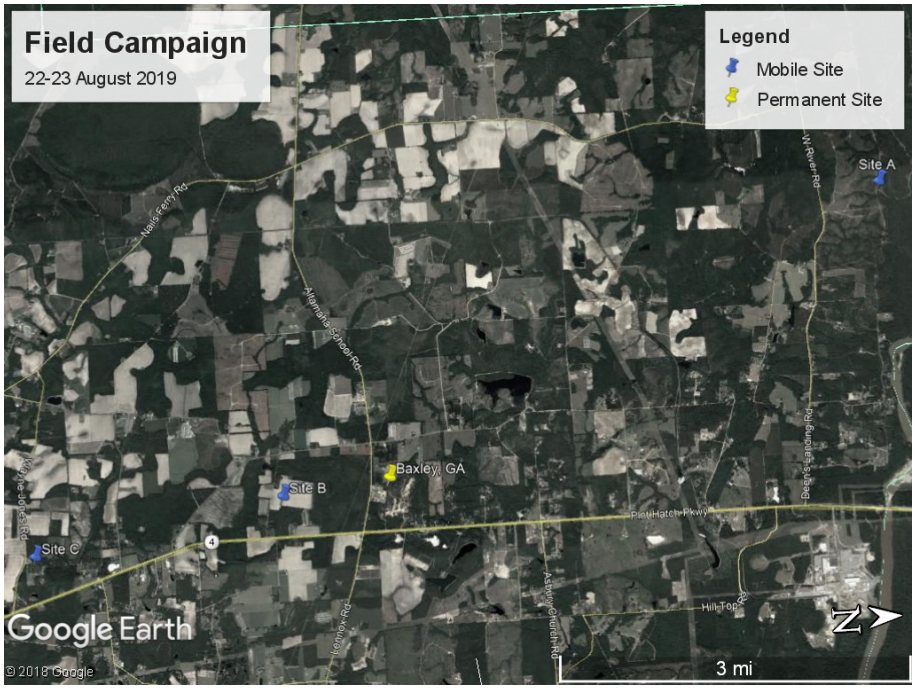

Figure 6.9: Permanent and mobile locations during the 22 August 2019 campaign.

6.2 Analysis from Field Campaigns

6.2.1 Non-Stationarity and Time Series Window Size

In order to discern variations and trends in the measured D-region roughness metrics, the time series of all the data collected must be subsampled into smaller windows to increase the number of available observations. The optimal window size is one that has the smallest possible size, while maintaining stable stochastic properties. The first check is to test the stationarity of the process being detected. Stationarity is often an underlying assumption in time series analysis and enables the use of many simplifications. The two most common types of stationarity are: 1) *Strict-Sense Stationary* (SSS) and 2) *Wide-Sense Stationary* (WSS). An SSS process is a stochastic process that has a unconditional joint probability distribution that doesn't change when shifted in time. Another way of stating this is that, for a stochastic process to be SSS, all orders of its moments must be time invariant, *Durgin* [2002]. The benefit of an SSS stochastic process is that its distribution, if given enough samples, will converge on the stationary distribution. In the context of measuring the roughness in the electron density of the D-region, this would mean that, given enough samples, the distribution of the correlation length scales, and possibly RMS height variation, would converge on a fixed distribution. A WSS process, often called a "weak sense stationary" process, is a "weak" form of SSS that allows a time series to be described in the context of a Hilbert space. For a process to be WSS, the mean value and autocorrelation functions must be time invariant, *Durgin* [2002]. A process that is considered SSS is also WSS, however a process that is WSS isn't necessarily SSS. Thus, the data collected from the field campaigns will first be tested to determine if it is WSS.

In order to test if a stochastic process is wide-sense stationary, two things must be found to be true. First, the mean value must be time invariant, or *mean stationary*. The top panel of Figure 6.10 shows uncalibrated (or raw) amplitude data in dB from the longest consecutive time series taken, the 7-September-2019 campaign, for each receiver site. The middle panel shows the top panel, but with a 25-minute moving average window filter applied to each time series. The bottom panel shows the top panel, but with a 180-minute window moving average filter. As the window size increases, the mean appears to converge towards

a stationary value, but does vary with time and thus is not considered mean stationary.

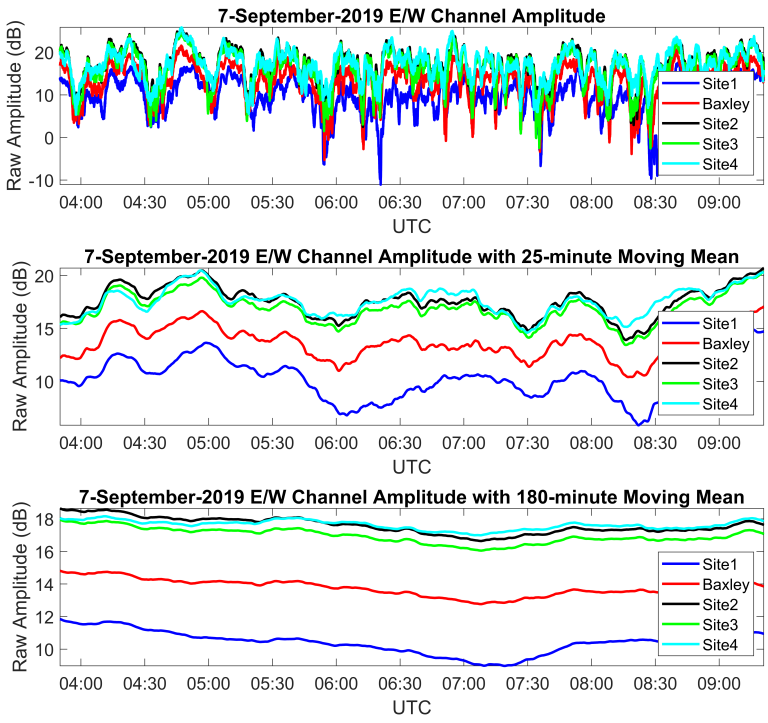

Figure 6.10: East/West channel amplitude data from the NDGPS transmitter in English Turn (LA), transmitting at 293 kHz, captured during the 7-September-2019 field campaign. Top panel: The raw amplitude, in dB, of the E/W channel for each site. Middle panel: A 25-minute moving mean window of the data in the top panel. Bottom panel: A 180-minute moving mean window of the data in the top panel.

The second test for a WSS stochastic process is *autcorrelation stationarity*. Figure 6.11 shows the autocorrelation data for the fixed receiver site in Baxley (GA) for the same data used above, the 7-September-2019 field campaign collecting data from the English Turn (LA) NDGPS transmitter. In this case, the major axis and minor axis are used. The top left panel shows the major axis autocorrelation function for 25-minute windows superimposed on top of each other. It is quite evident from the plot that the autocorrelation function changes with time. The top right panel shows a similar plot for the minor axis length with the same conclusion. Another way of interpreting the data is by using a *autocorrelation length scale* metric, which, like the correlation length scale, is calculated by finding the lag that corresponds to a autocorrelation of $e^{-1} \approx 0.367$. The bottom panel of the figure shows

the autocorrelation length scale of the major axis (blue line) and minor axis (red line), where each point corresponds to one of the 25-minute windows in the two top panels. From this figure, it is quite evident that the autocorrelation function can change quite drastically in the course of a few hours and is not autocorrelation stationary. In addition, as it will become apparent later in this section, the LF/MF reflections from the D-region are not joint WSS either, meaning that their cross-correlation function is not time invariant.

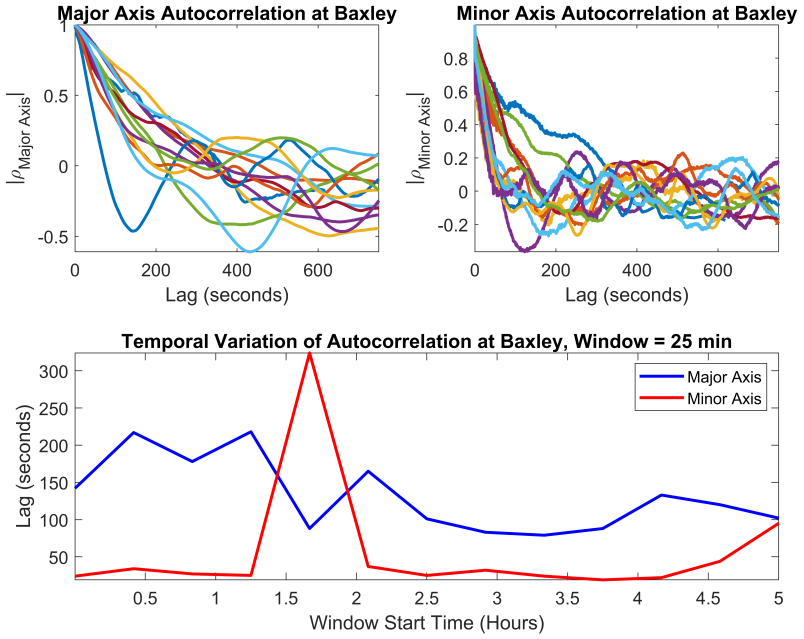

Figure 6.11: Autocorrelation data for the major axis and minor axis from the NDGPS transmitter in English Turn (LA), transmitting at 293 kHz, captured during the 7-September-2019 field campaign. Top left panel: Superimposed autocorrelation functions of 25-minute windows for the major axis length. Top right panel: Superimposed autocorrelation functions of 25-minute windows for the minor axis length. Bottom panel: A time series of the *autocorrelation length scale* for both the major and minor axis length.

Since the data collected from the data campaigns is not WSS, it is also clearly not SSS. Intuitively this makes sense since it is well known in literature that the nighttime D-region is highly erratic, e.g. *Thomson et al.* [2007]. However, a meaningful method is needed to determine an (approximately) optimal window size to use to segment the data collected from the field campaigns. As previously stated, the window size should be chosen to be as long as possible to provide a better estimate of the stochastic process, while being short enough to capture the underlying time variation. The work by *Arikan and Erol* [1998]

discusses methods for determining a proper window size for sliding window statistics where the process will be "locally stationary", specifically in the context of ionospheric remote sensing. An empirical method described in this work is to inspect the data around the calculated sliding window mean, μ, for different window sizes and select the longest window for which most of the data lies within a standard deviation, σ, of the mean. For example, Figure 6.12 shows the major axis data from the 7-September-2019 campaign collected at the permanent Baxley receiver site for the transmitter in English Turn (LA) with two different rolling windows. The top panel shows a 10-minute window, where the blue line is the major axis data, the solid red line is the mean value, and the dashed red lines are the mean plus or minus the standard deviation. The bottom panel shows a similar plot, but with a 20-minute window. The empirical method described in *Arikan and Erol* [1998] suggests that the proper window size to select should be one that is as long as possible, but contains the most points within one standard deviation of the mean, or within the dashed red lines. It is evident that, when comparing the top panel to the bottom panel, with a small window size the solid and dashed red lines tend to follow the major axis amplitude with high sensitivity, thus demonstrating that the window is more sensitive to temporal variations. As the window size increases, the solid and dashed red lines become more "smoothed" and less sensitive to temporal variations.

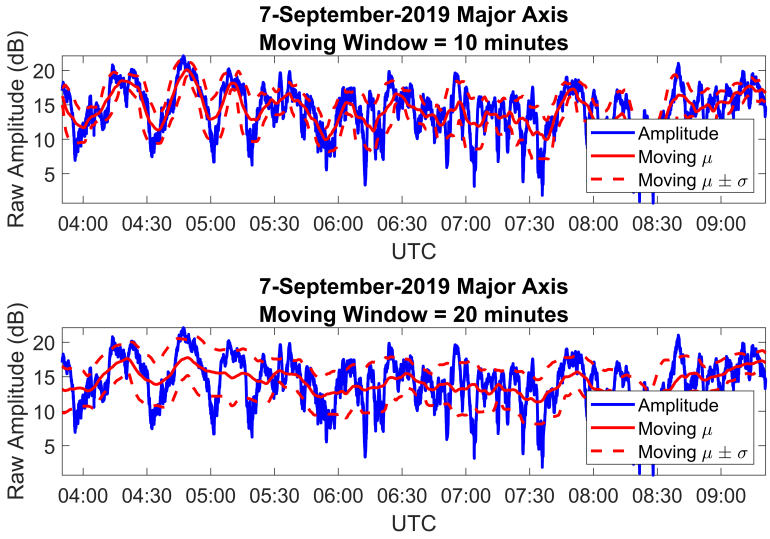

Figure 6.12: Example of the inspection method outlined in *Arikan and Erol* [1998]. A 10-minute window is used in the top panel and a 20-minute window is used in the bottom panel.

Figure 6.13 shows the summary of a test to empirically find an optimal window size using the same data from the 7-September-2019 field campaign as above. The x-axis shows the window size in minutes, ranging from 1 minute to 180 minutes. The y-axis shows the ratio of points outside $\mu \pm \sigma$, or the number of points outside of one standard deviation of the mean, as a percentage of the total number of points. The blue line is the major axis and the red line is the minor axis. In both cases, a "knee" appears around $15-25$ minutes, which indicates an ideal solution. For both the major and minor axis, the 20-minute window values are highlighted using the dashed lines. At this window size, about 30.6% of points in the major axis lie outside of the first standard deviation from the mean and 23.1% for the minor axis.

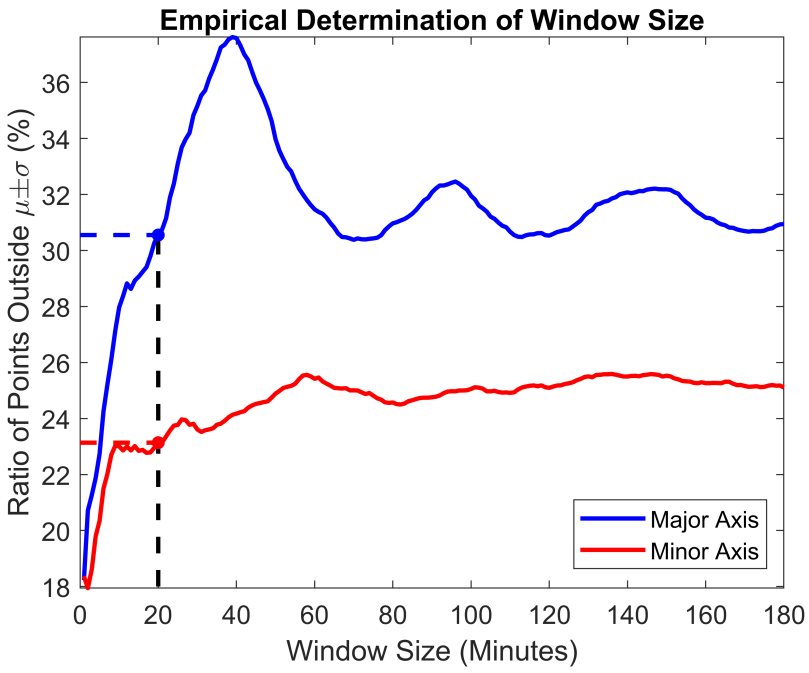

Figure 6.13: Graphical test to empirically determine an approximately optimal window size to segment the field campaign data. The major axis is shown as a blue line and the minor axis is shown as a red line.

Using the initial hypothesis of the proper window size being approximately 15−25 minutes as described above, the next step is to examine the metrics of interest, namely the correlation length scale. Analogous to above, increasing the window size used for a cross-correlation would increase its fidelity, but decrease its sensitivity to temporal variations. Thus, a proper window size would be as long as possible, while maintaining temporal sensitivity. This can be empirically found as the shortest window size that just stabilizes the variation in the correlation length scale. Figure 6.14 shows the change in correlation length scale as a function of time and window size. The top panel shows the major axis correlation length, where each line represents a different window size as noted in the legend. The red dashed line is the correlation length for the entire time series. Each point in each line corresponds to the start time of the window used. The bottom panel shows the minor axis correlation length. Note that window overlap is not considered in this figure and each window has no overlap with the neighboring windows. Figure 6.15 is identical to Figure 6.14, but the smallest four window sizes (10, 15, 20, and 25 minutes) are highlighted. The gray lines, the larger window sizes, are all consistent and by highlighting the smaller window

sizes it becomes evident that the correlation length scales in both the major and minor axis begin to converge around 25 minutes. Figure 6.16 is similar to Figure 6.14, but the smallest window size is set to 25 minutes. In this case it becomes very evident that the different window sizes, for both the major and minor axis, have converged to the same shape. This indicates that 20-25 minutes would be a proper window size to use, which is consistent with the initial hypothesis from above.

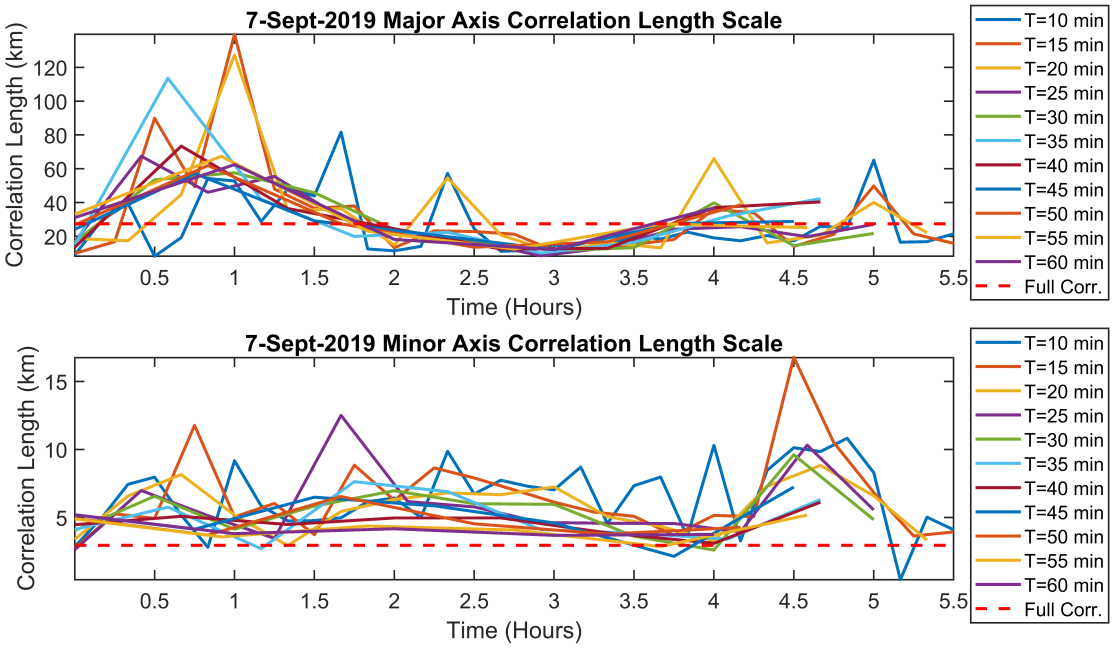

Figure 6.14: Superposition of the correlation length scale, as a function of time, calculated for varying window sizes. The top panel shows the major axis correlation length and the bottom panel shows the minor axis correlation length.

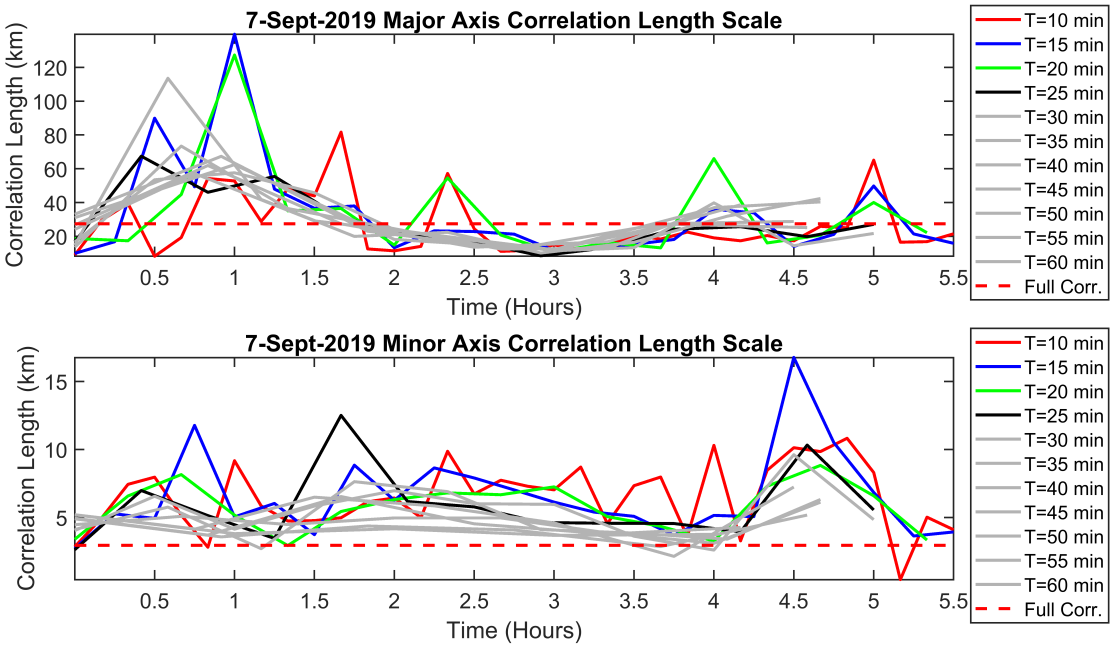

Figure 6.15: Superposition of the correlation length scale, as a function of time, calculated for varying window sizes with the four smallest window sizes highlighted. The top panel shows the major axis correlation length and the bottom panel shows the minor axis correlation length.

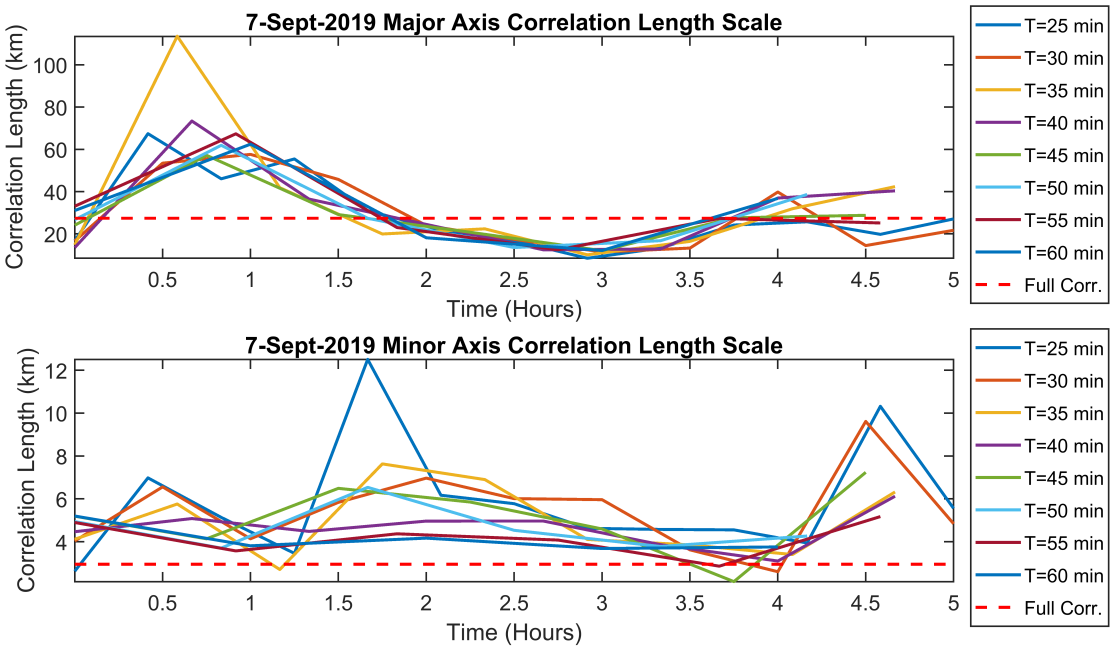

Figure 6.16: Superposition of the correlation length scale, as a function of time, calculated for varying window sizes with the three smallest window sizes removed. The top panel shows the major axis correlation length and the bottom panel shows the minor axis correlation length.

Window overlapping will now be considered in order to maximize the length of each window and the number of windows. Figure 6.17 shows the variation in correlation length for two window sizes (15 minutes and 20 minutes) for three degrees of overlap (0, 2.5, and 5 minutes) for the major axis, top panel, and minor axis, bottom panel. In this case, the overlap is padded on the beginning and end of the indicated window. For example, a 20-minute window with a 2.5-minute overlap would effectively be a 25-minute window since the 2.5 minutes is added to each side of the window. From inspection of the top panel, it is evident that all lines tend to track each other fairly well. Ultimately, from this figure and from the other analysis described above, a window size of 20 minutes with a 2.5-minute overlap was selected since it tracked the scenario of a window size of 20 minutes and no overlap quite closely – a situation with negligible loss in temporal sensitivity and a gain in measurement fidelity.

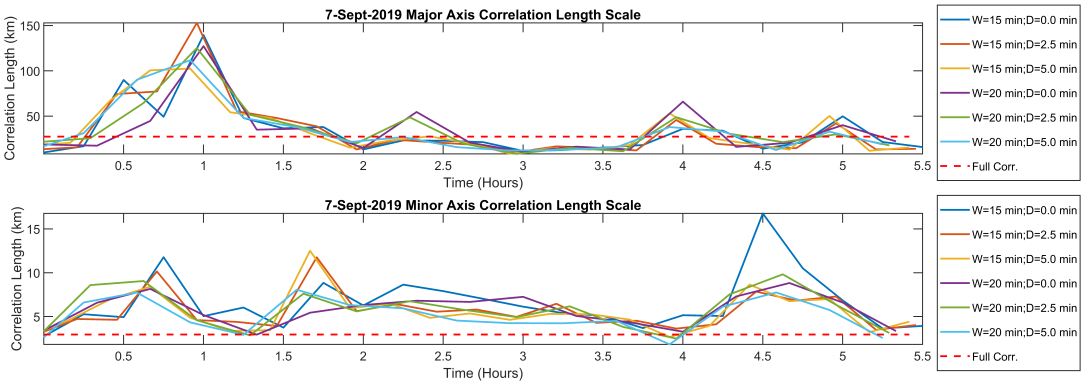

Figure 6.17: Superposition of the correlation length scale, as a function of time, calculated for varying window (denoted as "W" in the legend) and overlap (denoted as "D" in the legend) sizes. The top panel shows the major axis correlation length and the bottom panel shows the minor axis correlation length.

6.2.2 Horizontal Roughness

Using a window and overlap size of 20 ± 2.5 minutes, as determined in the previous section, all the collected field campaign data can be segmented and analyzed. This section will focus on the "horizontal roughness", namely the correlation length scale. Figure 6.18 summarizes all the collected field campaign data. The data is segmented by major and minor axis and by the orientation of the antenna array in regard to the transmitter being detected. Recall that "radial" refers to the array being parallel to the path of propagation and "transverse" refers to the array being perpendicular to the path of propagation. In each of the four panels a histogram of the correlation length scale, normalized by the wavenumber according to Equation 6.1, is shown with the y-axis indicating the probability density function, or PDF. The geometric mean and standard deviation are shown in the top right corner of each panel. The black line over each histogram is a best fit Rician distribution meant to capture the shape and trend of the distribution of each data set. The most pronounced trend in the figure is the difference between the major and minor axis correlation lengths in terms of the shapes, i.e. mean and standard deviation, of the distributions. The differences between the radial and transverse distributions, for both the major and minor axis, are a lot more subtle. This may suggest that the major axis, or H_ϕ, is sensitive to a different scattering mechanism than the minor axis, or H_θ.

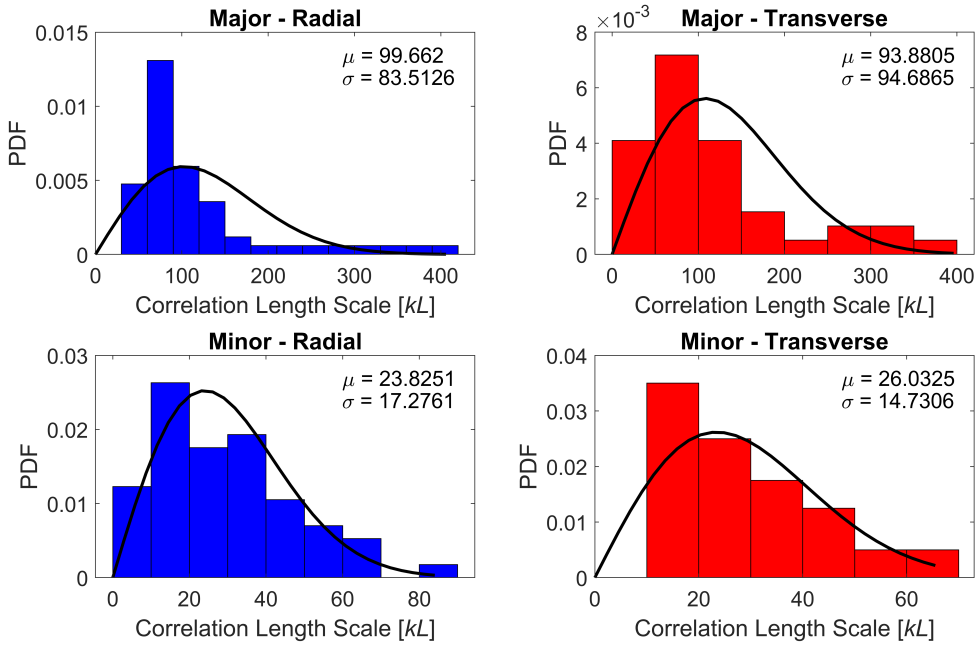

Figure 6.18: Summary of the measured correlation length scale values for all field campaigns. Top left panel: Major axis correlation length scale for the radial direction. Top right panel: Major axis correlation length scale for the transverse direction. Bottom left panel: Minor axis correlation length scale for the radial direction. Bottom right panel: Minor axis correlation length scale for the transverse direction.

$$kL = \frac{2\pi}{\lambda} L \tag{6.1}$$

Another way of interpreting the data in Figure 6.18 is in reference to the estimated Fresnel zone size for the respective dimension. Figure 6.19 shows the same data as in Figure 6.18, but normalized by the Fresnel zone. Due to the long propagation paths used, the radial dimension of the Fresnel zone is much larger than the transverse dimension, with the latter remaining consistent. This property can be observed in the two left panels of the figure, the radial orientations, which have different shapes than those in Figure 6.18, but the right panels, the transverse orientation, remained fairly consistent. In literature, the ratio of the correlation length and the Fresnel zone is used to determine what, if any, approximations can be made to model scattering. The work done by *Spetzler and Snieder* [2001a], *Spetzler and Snieder* [2001b], and *Spetzler et al.* [2002] investigated when it was appropriate to use ray theory versus scattering theory based on this ratio, which can be used

to provide a sense of scale of roughness. The correlation length scale can be thought of as a proxy for the scale of the perturbation, *Bowles et al.* [1963], or rather the resulting angular spreading of the signal, *Bramley* [1951] and *Lindner* [1975b]. If the primary scattering mechanism is attributed to some number of small irregularities, then the correlation length scale is expected to be smaller than the Fresnel zone, **?**. If the correlation length scale is larger than the Fresnel zone, then it is suggested that a larger-scale structure is causing the scattering. The radial major axis, top left panel, and minor axis values, two bottom panels, both fall in the regime of "scattering theory", i.e. $\frac{L}{L_F} < 1$, while the top right panel, the case of the transverse major axis, falls partly in the regime of "ray theory", i.e. $\frac{L}{L_F} >> 1$.

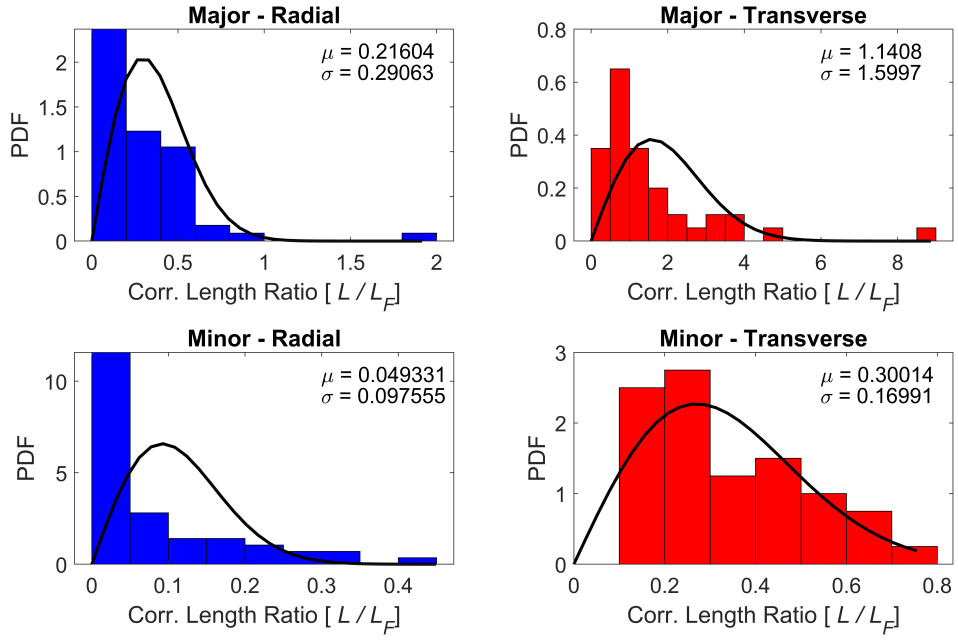

Figure 6.19: Summary of the measured correlation length scale values for all field campaigns normalized by their approximate Fresnel zone dimensions. Top left panel: Major axis correlation length scale for the radial direction. Top right panel: Major axis correlation length scale for the transverse direction. Bottom left panel: Minor axis correlation length scale for the radial direction. Bottom right panel: Minor axis correlation length scale for the transverse direction.

Each panel of Figure 6.18 can be segmented into the respective campaigns, such as in Tables 6.3, 6.4, 6.5, and 6.6. Table 6.3 and 6.5 aggregate the radial major axis and radial minor axis correlation length means and standard deviations for the data collected from three NDGPS transmitters: Detroit (MI), Tampa (FL), and Card Sound (FL), transmitting

at 319 kHz, 312 kHz, and 314 kHz respectively. Table 6.4 and 6.6 aggregate the transverse major axis and minor axis correlation length means and standard deviations for the data collected from the transmitter in English Turn (LA) transmitting at 293 kHz. When the data is separated by field campaigns, date of collection, day to day variations can be examined.

For example, in Figure 6.3 the campaign data from 13-June-2019 and 22-August-2019 appears to be less perturbed than on the other days since both the mean and the standard deviations for those days are lower. This pattern can be seen in Table 6.4, however 6-September-2019 doesn't appear to be perturbed. It is possible, since Table 6.3 shows predominantly North-South paths and Table 6.4 shows a long East-West path, that the perturbed part of the D-region may not be captured until the following day, 7-September-2019. One possible hypothesis for this pattern of perturbation could be that it is caused by atmospheric gravity waves (AGWs), *Maurya et al.* [2019], from hurricane Dorian, *Kumar et al.* [2017], which was off the coast of the southeastern CONUS during this time in early September and the delay in these perturbations reaching the East-West propagation path in the transverse direction (between Baxley (GA) and English Turn (LA)) being the distance from the source. However, without more exhaustive data collection, this is merely conjecture. A second hypothesis for the trend observed could be an underlying seasonal variation being captured where summer months are less rough than the winter months, *Tan et al.* [2015]. However, once more, more exhaustive data collection is needed to test this hypothesis. Although both trends mentioned aren't evident in the minor axis data shown in Table 6.5 and 6.6, this may suggest that the major and minor axis are sensitive to different scattering mechanisms.

Table 6.3: Summary table for the major axis correlation length measurements taken in the radial orientation. Aggregates data from the NDGPS transmitters in Detroit (319 kHz), Tampa (312 kHz), and Card Sound (314 kHz).

Campaign Date	Mean	Standard Deviation	Number of Windows
01/14/19	104.99	38.31	3
06/13/19	93.6	81.92	12
08/22/19	86.57	25.34	14
09/06/19	125.77	385.52	11
09/07/19	116.30	108.96	17

Table 6.4: Summary table for the major axis correlation length measurements taken in the transverse orientation. Aggregates data from the NDGPS transmitter in English Turn (293 kHz).

Campaign Date	Mean	Standard Deviation	Number of Windows
01/14/19	151.20	143.0	3
06/13/19	46.29	17.98	4
08/22/19	84.19	15.15	5
09/06/19	53.26	23.10	11
09/07/19	171.88	172.16	17

Table 6.5: Summary table for the minor axis correlation length measurements taken in the radial orientation. Aggregates data from the NDGPS transmitters in Detroit (319 kHz), Tampa (312 kHz), and Card Sound (314 kHz).

Campaign Date	Mean	Standard Deviation	Number of Windows
01/14/19	32.21	12.46	3
06/13/19	24.26	22.78	12
08/22/19	33.11	16.16	14
09/06/19	12.21	4.07	11
09/07/19	26.21	13.66	17

Table 6.6: Summary table for the minor axis correlation length measurements taken in the transverse orientation. Aggregates data from the NDGPS transmitter in English Turn (293 kHz).

Campaign Date	Mean	Standard Deviation	Number of Windows
01/14/19	40.72	20.00	3
06/13/19	16.40	7.13	4
08/22/19	32.97	13.51	5
09/06/19	17.14	4.28	11
09/07/19	32.79	13.85	17

6.2.3 Vertical Roughness

Once more using the window size and overlap of 20 ± 2.5 minutes, the data is segmented and analyzed to investigate the vertical roughness. Figure 6.20 summarizes all the collected field campaign data. The data is segmented by the orientation of the antenna array in regard to the transmitter being detected – radial and transverse. In each panel a histogram of the RMS height variation, normalized by the wavenumber according to Equation 6.2, is shown with the y-axis indicating the probability density function, or PDF. The geometric mean and standard deviation are shown in the top right corner of each panel. The black line over each histogram is a best fit Rician distribution meant to capture the shape and trend of the distribution of each data set. Unlike the correlation length scale data, the variation in the RMS height appears to be a lot lower. In addition, the RMS height appears to be consistent across field campaigns, however, as in the case of the correlation length scale, more data must be collected in order to determine any seasonal trends.

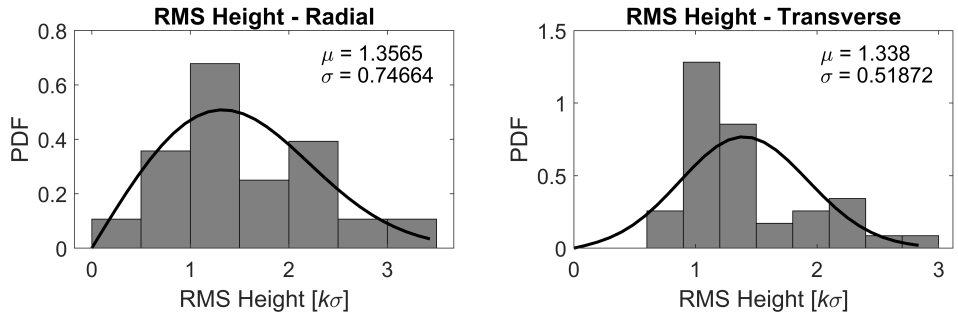

Figure 6.20: Summary of the RMS height variation values for all field campaigns calculated using the differential phase height method. Left panel: RMS height values calculated for the radial orientation. Right panel: RMS height values calculated for the transverse orientation.

$$k\sigma = \frac{2\pi}{\lambda}\sigma \tag{6.2}$$

6.2.4 Comparison to VLF Data

Using a Very Low Frequency (VLF) transmitter on a similar path to a LF/MF NDGPS transmitter, the above roughness metrics can be studied as a function of frequency. This comparison can be done using the data collected on the 7-September-2019 field campaign in Baxley, Georgia, for the VLF transmitter in North Dakota, call sign "NML", and the NDGPS transmitter in Detroit, Michigan. Figure 6.21 shows the transmitter-receiver geometry (red lines) between Baxley, Georgia, (blue dot) and the two transmitters (red dots). The Detroit NDGPS transmitter is located approximately 1151.7 km from Baxley (GA) in a North-South path and transmits at 319 kHz. The NML transmitter is located approximately 2104.7 km from Baxley (GA) in a more Northwest-Southeast path and transmits at 25.2 kHz. Although the NML-to-Baxley path is not an ideal comparison to the Detroit-to-Baxley path, it can serve as a useful proxy for investigating how the roughness metrics vary with frequency.

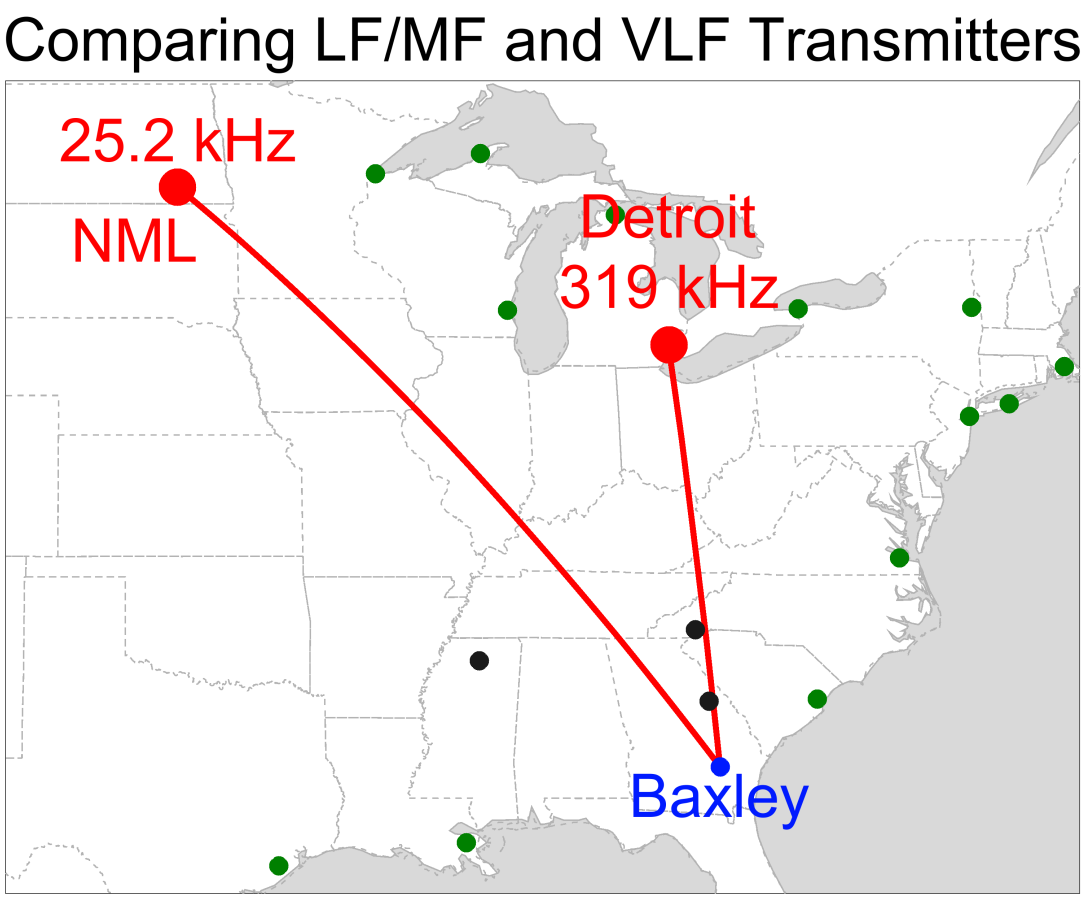

Figure 6.21: Map of the two transmitter-receiver great circle paths (red lines) used to compare the roughness metrics from a VLF transmitter (NML, 25.2 kHz) and an NDGPS transmitter (Detroit (MI), 319 kHz). Data was collected during the 7-September-2019 field campaign in Baxley, Georgia (blue dot).

First, using the same window and overlap size of 20 ± 2.5 minutes, the horizontal roughness, or correlation length scale, is investigated. Figure 6.22 summarizes the correlation length scale data for both transmitters. The two left panels show the data for the NDGPS transmitter. The top panel shows the major axis correlation length scale data and the bottom panel shows the minor axis correlation length scale data. The right panels show the data for the VLF transmitter. The top panel shows the major axis correlation length scale data and the bottom panel shows the minor axis correlation length scale data. Once more, in each panel, the mean, μ, and standard deviation, σ, are show in the top right corner and the black line shows the best fit Rician to give a sense of the shape of the distribution. All values are normalized by the *wavenumber* of the respective transmitter.

Between both frequencies, the major and minor axis correlation lengths have similar shapes, but there is a significant difference in the magnitudes of the correlation length values. The NDGPS transmitter values tend to be much higher than the VLF values, primarily due to the correlation length scales being normalized by the wavenumber (i.e. $\propto \frac{1}{\lambda}$) of the transmitters, where VLF wavelengths are about $10\times$ larger than LF/MF wavelengths. The normalization gives a reference for how rough the D-region is given the wavelength and, in general, the correlation length scale can serve as a proxy for the scale of the perturbation, e.g. *Bowles et al.* [1963], *Bramley* [1951], and *Lindner* [1975b]. In the case of Figure 6.22, the major axis correlation length scale measured using the NDGPS transmitter is about $8\times$ larger than that measured by the VLF transmitter when normalized by the wavenumber, $3.8\times$ for the minor axis. This suggests that the roughness, or perturbations, measured by the NDGPS transmitters were larger, or caused more angular spreading, relative to the frequency compared to the VLF transmitters. This roughly translates to the D-region electron density being measured as "smoother" when using VLF. Early work using the partial reflection technique, *Lindner* [1975a], found that the angular spreading tended to increase with height. This would be consistent with the trend here if it is assumed that the absolute reflection height of the VLF wave is lower than the LF/MF wave.

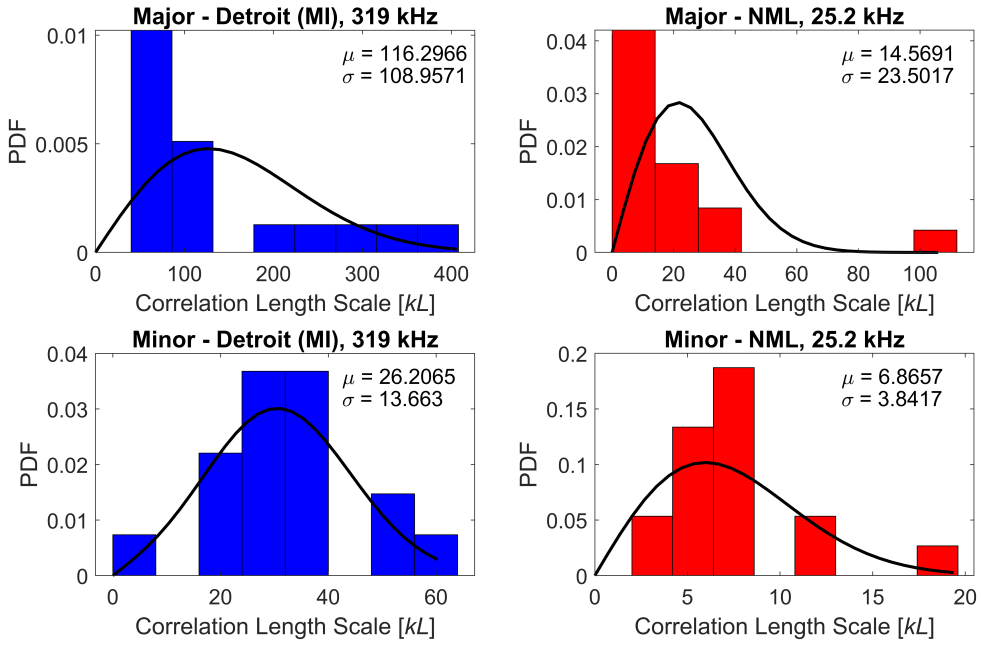

Figure 6.22: Summary of the correlation length scale values from the 7-September-2019 field campaign calculated in the radial direction. Left panels: Major axis (top) and minor axis (bottom) correlation length scales calculated for the NDGPS transmitter in Detroit (MI) transmitting at 319 kHz at a distance of 1151.7 km. Right panel: Major axis (top) and minor axis (bottom) correlation length scales calculated for the VLF transmitter "NML" transmitting at 25.2 kHz at a distance of 2104.7 km.

Next, using the same window configuration, the vertical roughness, or RMS height variation, is investigated. Figure 6.23 summarizes the RMS height variation data for both transmitters. The left panel shows the data for the NDGPS transmitter. The right panel shows the data for the VLF transmitter. In each panel, the mean, μ, and standard deviation, σ, are show in the top right corner and the black line shows the best fit Rician to give a sense of the shape of the distribution. All values are normalized by the *wavenumber* of the respective transmitter. Recall that the RMS height variation measured is calculated using the *differential phase height* method described in the previous chapter. Thus, this is a relative measure between two points in the D-region. Both panels have similar shapes, however the left panel mean value, showing the NDGPS transmitter, is about 36$\times$ larger than the right right panel, VLF transmitter, mean. This suggests that the variation in phase height between two points is much higher, relatively to a wavelength, for an LF/MF wave than for a VLF wave. This is consistent with the correlation length scale measurement

in suggesting that the D-region appears "smoother" for the VLF transmitter.

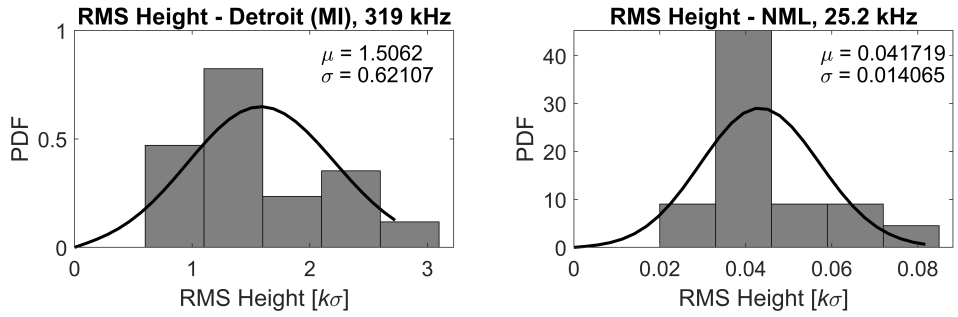

Figure 6.23: Summary of the RMS height variation values from the 7-September-2019 field campaign calculated using the differential phase height method in the radial direction. Left panel: RMS height values calculated for the NDGPS transmitter in Detroit (MI) transmitting at 319 kHz at a distance of 1151.7 km. Right panel: RMS height values calculated for the VLF transmitter "NML" transmitting at 25.2 kHz at a distance of 2104.7 km.

6.3 Modeling Results from Field Campaigns

In Section 5.5 a method for modeling the potential electron density roughness of the D-region using the Monte Carlo method (MCM) with a Finite-Difference Time-Domain (FDTD) model. Using the data collected from the field campaigns, the measured results for the correlation length scale can be compared to the modeled correlation length scales in order to try estimate the electron density roughness using the "ionospheric length scale" metric. Two propagation paths will be investigated using the MCM FDTD method to examine the variation in the ionospheric length scale.

The first propagation path that will be investigated is from the transmitter in Card Sound (FL), transmitting at 314 kHz, to about 740 km away at the field campaign site in Baxley (GA). Figure 6.24 shows a summary of the modeled results around the receiver location. The left panel shows the full solution space around the receiver as a function of distance (from transmitter), correlation length scale, and ionospheric length scale. This is very similar to the figure shown in Section 5.5, but the correlation length scale has been normalized by the wavenumber to be consistent with the campaign results shown in this chapter. The right panel shows three horizontal slices of the left panel to illustrate the relationship between the correlation length scale and ionospheric length scale for three

different distances. Generally, as the ionospheric length scale increases, the correlation length scale increases as well. This is driven in part because the roughness, or irregularities in the electron density, become larger relative to a wavelength. The right panel of this figure can be recreated for the approximate distance from the transmitter to the receiver. Figure 6.25 shows the appropriate slice at 740 km that can be used to estimate the correlation length scale values at the receiver site. Using the standard window size of 20 ± 2.5 minutes, the radial major axis correlation length scale for all the campaign data collected for Card Sound (FL), which includes data from the 6/13/2019 and 8/22/2019 measurement sets, is found to have a mean and standard deviation of 117.1095 ± 38.7277. Unfortunately, these values are much larger than the modeled results. If the window size is decreased to 5 ± 5 minutes, then there is only one data point that can be matched to the modeled results – a 38.5052 correlation length scale that corresponds to an ionospheric length scale of 45.66 km, which is indicated by the dashed red lines in the figure.

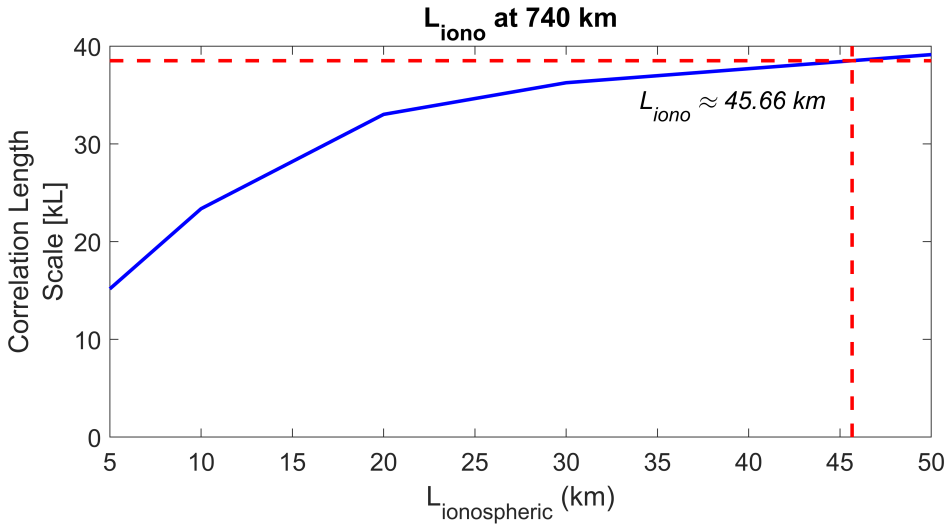

Figure 6.25: The modeled correlation length scale, normalized by the wavenumber, as a function of the ionospheric length scale for a distance of 740 km, the approximate distance of the NDGPS transmitter in Card Sound (FL) to Baxley (GA).

The second propagation path that will be investigated is from the transmitter in Detroit (MI), transmitting at 319 kHz, to about 1158 km away at the field campaign site in Baxley (GA). Figure 6.26 shows a summary of the modeled results around the receiver location. The left panel shows the full solution space around the receiver as a function of distance

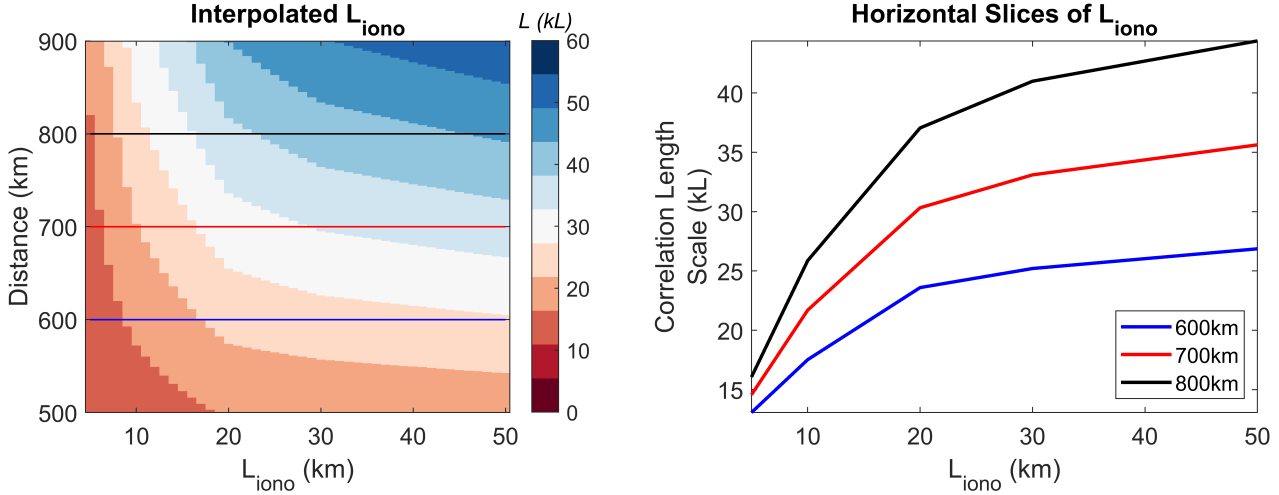

Figure 6.24: Left panel: A two dimensional image depicting the relationship between the ionospheric length scale, the estimated correlation length scale (normalized by the wavenumber), and the distance from the transmitter for a 293 kHz source. Right panel: Three horizontal slices of the left panel depicting three individual distances and the relationship between ionospheric length scale and correlation length scale.

(from transmitter), correlation length scale, and ionospheric length scale. In this case, the correlation length scale has not been normalized by the wavenumber. The right panel shows three horizontal slices of the left panel to illustrate the relationship between the correlation length scale and ionospheric length scale for three different distances. In contrast to Figure 6.24, the correlation length scale does not monotonically increase as the ionospheric length scale increases. Instead, there are two peaks at $L_{iono} \approx 10$km and $L_{iono} \approx 25$km. Figure 6.27 shows the appropriate slice at 1158 km that can be used to estimate the correlation length scale values at the receiver site. Using the standard window size of 20 ± 2.5 minutes, the radial major axis correlation length scale for all the campaign data collected for Detroit (MI), which includes data from the 6/13/2019, 8/22/2019, 9/06/2019, and 9/07/2019 measurement sets, is found to have a mean and standard deviation of 23.83 ± 34.33. While the previous case underestimated the correlation length values, this case appears to overestimate the correlation length values. About 16.7% of observation points can be explained using the MCM FDTD method and are plotted as the red dots in the left panel of Figure 6.27 and summarized by the histogram in the right panel. Although there are multiple solutions, in some cases two or three possible solutions, the dots were plotted assuming the highest possible ionospheric length scale. It is important to highlight that the majority of the data explained using the MCM FDTD method comes from the June and August campaigns, which are relatively calmer, but the bulk of the data was actually collected during the two September campaigns, which had a hurricane off the coast of the CONUS. Thus, more quiet data is needed in order to truly determine the baseline effectiveness of this method.

Two propagation paths were investigated using the MCM FDTD method. The first case, Figure 6.24, examined the Card Sound (FL) transmitter at a distance of about 740 km and found that only a single observation point could be explained. In this case, the method underestimated the correlation length scale values. The second case, Figure 6.26, examined the Detroit (MI) transmitter at a distance of about 1158 km and explained about 16.7% of observations points, but generally overestimated the correlation length scale values. In both cases, there is clearly an underlying mechanism of the roughness that is not being fully captured by the MCM FDTD method. The use of the ionospheric length scale and the

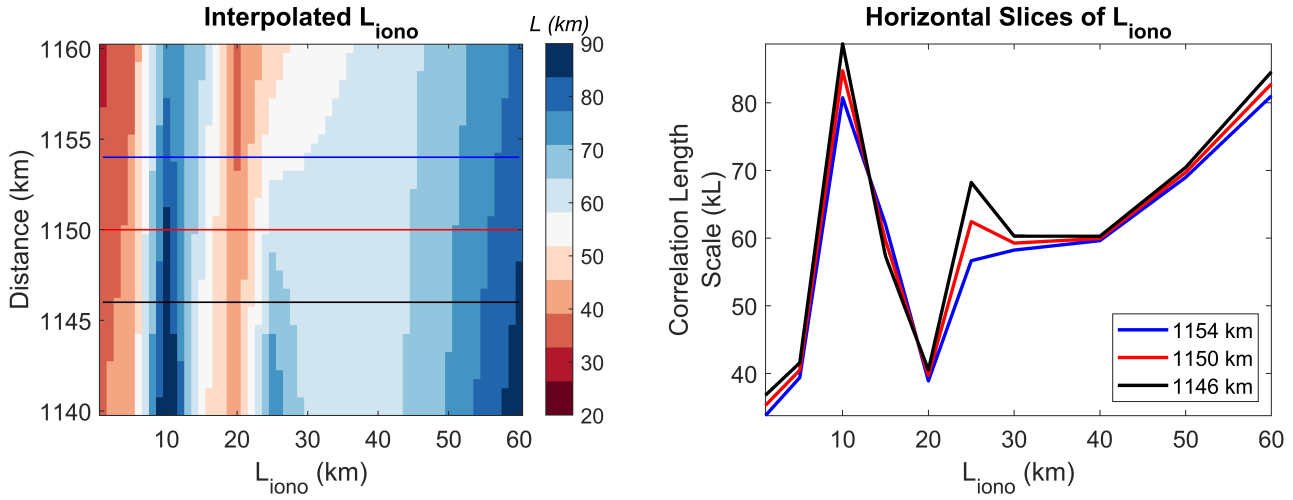

Figure 6.26: Left panel: A two dimensional image depicting the relationship between the ionospheric length scale, the estimated correlation length scale, and the distance from the transmitter for a 319 kHz source. Right panel: Three horizontal slices of the left panel depicting three individual distances and the relationship between ionospheric length scale and correlation length scale.

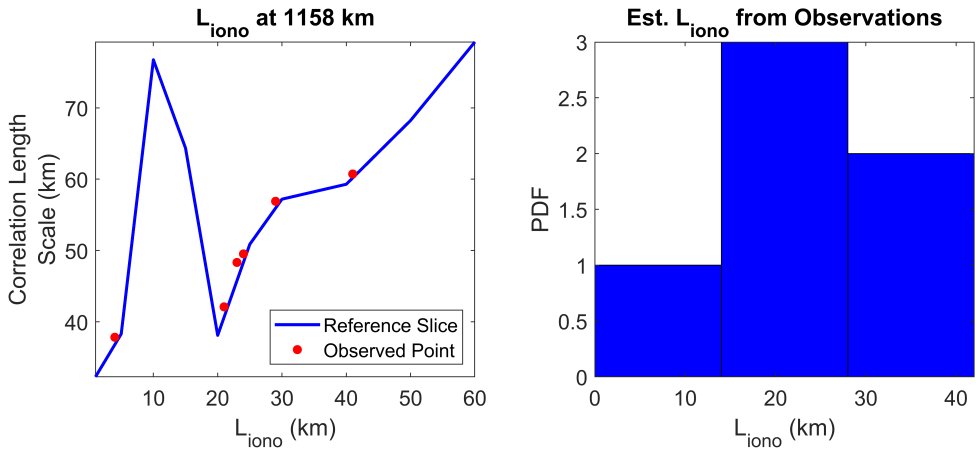

Figure 6.27: The modeled correlation length scale as a function of the ionospheric length scale for a distance of 1158 km, the approximate distance of the NDGPS transmitter in Detroit (MI) to Baxley (GA). Observations that can be explained by the modeled correlation length scale are shown as red dots.

MCM FDTD has a strong dependence with distance – generally as the distance from the transmitter increases the correlation length scale will also increase. However, the observations from the field campaigns don't show this same trend. Thus, this would indicate that some mechanism of roughness is not being properly modeled. Future modeling should focus on resolving this inconsistency. Three possible directions for future work could be to: 1) extend the MCM FDTD to a three-dimensional model, 2) model the effect of atmospheric gravity waves on the correlation length scale, and 3) model the effect of turbulence, e.g. moving "blobs" or "planes" of higher electron density, on the correlation length scale.

6.4 Suggestions for Future Field Campaigns

Future field campaign efforts should focus on two things: 1) continuous data collection for a year of time, 2) simultaneous collection of the radial and transverse component for a transmitter. The first point, briefly discussed in Sections 6.2.2 and 6.2.3, is needed to investigate underlying trends in the data, such as seasonal variations in roughness or changes in roughness due to perturbations. The second point addresses the spatial inconsistencies of the campaign styled field collection done for this work. Namely, data from transmitter-receiver paths were captured in either the radial or transverse direction and so different patches of the D-region were being simultaneously probed. In addition, if the array configuration

were changed from radial to transverse on the same night/campaign the issue of D-region non-stationarity would arise, and the radial/transverse measurements would be effectively for different D-regions.

To address both of these points, a "D-region roughness observatory", such as the one depicted in Figure 6.28, should be deployed as a permanent receiver array. Using three receivers in an L-configuration, with the radial direction pointed at a single transmitter, the array configuration will capture the radial and transverse correlation length scale simultaneously. Using the results discussed in Section 6.2.2, an appropriate radial spacing, marked as d_1, and transverse spacing, marked as d_2, can be determined. The mean radial major axis correlation length scale occurs at approximately 15.9λ, where λ is the wavelength of the transmitter, and the mean radial minor axis correlation length scale occurs at approximately 3.8λ. Thus, to measure the radial correlation length scale the second receiver should be placed at a distance, d_1, that allows for the measure of both the major and minor axis values with minimal extrapolation error. The second receiver should be placed at a distance of atleast half the correlation length scale to the full value of the correlation length scale. This gives a range of approximately 1.9λ to 3.8λ for the minor axis and 7.95λ to 15.9λ. The optimal spacing would be the spacing where both ranges overlap, which doesn't happen in this case. However, a second best alternative would be a spacing, d_1, between 3.8λ and 7.95λ. The mean transverse major axis correlation length scale occurs at approximately 14.9λ and the mean transverse minor axis correlation length scale occurs at approximately 4.1λ. Using the same logic for the transverse spacing, d_2, should be between 4.1λ to 7.4λ.

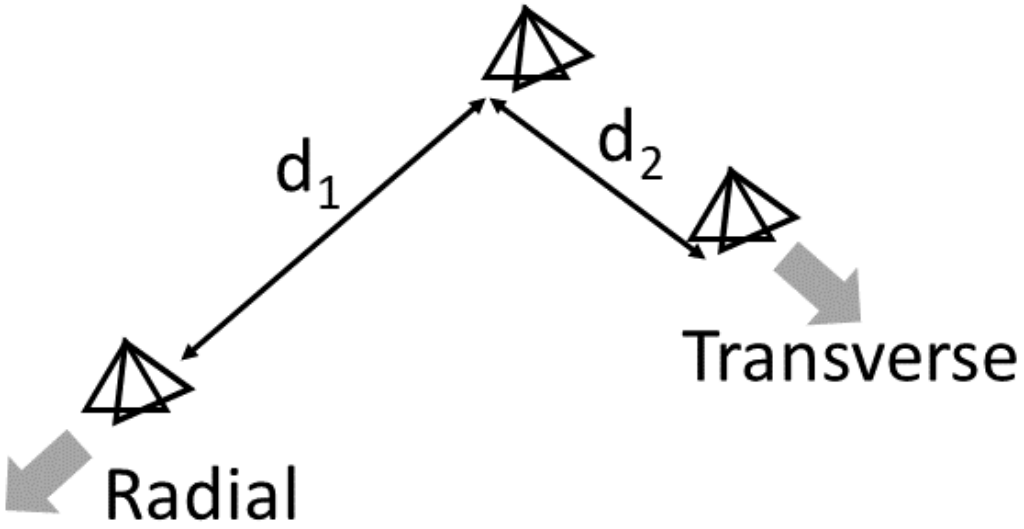

Figure 6.28: Proposed layout for a "D-region roughness observatory".

CHAPTER 7
SUMMARY AND SUGGESTIONS FOR FUTURE WORK

7.1 Summary

The roughness of the D-region electron density is poorly understood. Yet, measuring and characterizing the roughness would benefit our understanding of geophysical processes and phenomena, such as transionospheric propagation. This thesis presents a novel method to measure and characterize the D-region electron density roughness using a number of simultaneous measurements from LF/MF signals of opportunity.

In Chapter 1, the purpose of the research and background material are outlined. First, the research purpose and goals are described. Next, details about the LF/MF signals of opportunity, the Nationwide Differential GPS (NDGPS) network, and the radio receiver system, the LF AWESOME receiver, used are described. A review of D-region plasma physics and LF/MF propagation is presented next, followed by an overview of current D-region remote sensing techniques. Past works related to LF/MF remote sensing of the D-region and on lower ionospheric roughness are discussed. Finally, the conference and journal contributions related to this thesis are outlined.

In Chapter 2, an overview of D-region remote sensing using the NDGPS transmitters is presented. The data available from the LF AWESOME receivers and its interpretation is described. Then, using the data from the receivers, several observations are discussed including diurnal effects, seasonal effects, and perturbations.

In Chapter 3, the theory of propagation modeling using the full-wave method (FWM) and finite-difference time-domain (FDTD) method is presented. The FDTD method is then applied to study groundwave and skywave propagation from an NDGPS transmitter.

In Chapter 4, a case study investigating the 21-August-2017 "Great American" solar eclipse is presented to demonstrate the tools and techniques described in the first three chapters. Observations of forward and back scattering are presented. FDTD modeling is used to investigate the mechanism of back scatter from the eclipse totality spot and an

estimate for the D-region "settling rate", or the rate of change of the D-region needed to enable back scattering, is presented.

In Chapter 5, the theory of technique used to measure and characterize the D-region electron density roughness is presented. First, the theory of electromagnetic roughness is introduced. Next, the concept of the Fresnel zone, and its implication for this work, is described. Next, the technique used to measure the vertical and horizontal roughness are presented and discussed. Finally, the use of the Monte Carlo method (MCM) on an FDTD model is outlined and how the modeled results connect to the observations is discussed.

In Chapter 6, the data collected from a series of field campaigns will be outlined. The details of the field campaigns, and the needed hardware modifications, are described. The analysis of the field data using the described horizontal and vertical roughness metrics is presented. Comparisons are made between LF/MF data and VLF data using the roughness metrics. The MCM FDTD modeling method is then used to examine the field campaign observations. Finally, suggestions for future field campaigns are presented.

7.2 Future Work

7.2.1 Data Collection

Although field campaign-styled data collection is ideal for experimenting with receiver layout configuration or for targeted objectives, such as a proof of concept, its usefulness compared to the effort needed quickly diminishes. The next step to continue the work in this thesis would be to collect about a year of data for the vertical and horizontal roughness metrics, i.e. RMS height variation and correlation length. This could be done by deploying the "roughness observatory" outlined in Section 6.4. This wealth of data would enable the of study seasonal trends, to statistically characterize the roughness with greater confidence, and to study the effect of perturbations on the roughness, e.g. early/fast events, atmospheric gravity waves, and sprites/TLEs.

7.2.2 Roughness Modeling

Another way in which the work in this thesis can be expanded upon is by extending the MCM FDTD method described in Section 5.5. Specifically, the method can be expanded from a two-dimensional to a three-dimensional grid to investigate coupling between the radial and transverse roughness. In addition, the MCM FDTD could be used to investigate the effect of perturbations, e.g. atmospheric gravity waves, and turbulence, "bubbles" and "layers" of higher electron density, on the roughness metrics.

7.2.3 Investigate and Model Back Scattering

Finally, the case study in Chapter 4 can be extended in two ways. First, the back scatter modeling done for the 21-August-2017 solar eclipse can be extended to a three-dimensional grid, which may provide a more accurate estimate of the back scattering amplitude and the width of the transition region of the totality spot. Secondly, LF/MF back scattering from different perturbations, such as early/fast events or lightning-induced electron precipitation, can be investigated and modeled.

BIBLIOGRAPHY

Appleton, E. (1928), The study of signal fading. An account of the work of the Peterborough Radio Research Station of the Department of Scientific and Industrial Research, *Journal of the Institution of Electrical Engineers*, *66*(380), 872–881, doi: 10.1049/jiee-1.1928.0098.

Arikan, F., and C. B. Erol (1998), Statistical characterization of time variability in midlatitude single-tone HF channel response, *Radio Science*, *33*(5), 1429–1443, doi: 10.1029/98RS01889.

Barr, R. (1971), The effect of the Earth's magnetic field on the propagation of ELF and VLF radio waves, *Journal of Atmospheric and Terrestrial Physics*, *33*(10), 1577–1583, doi: 10.1016/0021-9169(71)90075-4.

Barr, R., D. Jones, and C. Rodger (2000), ELF and VLF radio waves, *Journal of Atmospheric and Solar-Terrestrial Physics*, *62*(17-18), 1689–1718, doi: 10.1016/S1364-6826(00)00121-8.

Belrose, J., and L. Thomas (1968), Ionization changes in the middle lattitude D-region associated with geomagnetic storms, *Journal of Atmospheric and Terrestrial Physics*, *30*(7), 1397–1413, doi: 10.1016/S0021-9169(68)91260-9.

Belrose, J., W. Hatton, C. McKerrow, and R. Thain (1959), The Engineering of Communication Systems for Low Radio Frequencies, *Proceedings of the IRE*, *47*(5), 661–680, doi: 10.1109/JRPROC.1959.287236.

Belrose, J., D. Ross, and A. McNamara (1972), Ionization changes in the lower ionosphere during the solar eclipse of 7 March 1970, *Journal of Atmospheric and Terrestrial Physics*, *34*(4), 627–640, doi: 10.1016/0021-9169(72)90150-X.

Belrose, J. S. (1970), Radio wave probing of the ionosphere by the partial reflection of radio waves (from heights below 100 km), *Journal of Atmospheric and Terrestrial Physics*, *32*(4), 567–596, doi: 10.1016/0021-9169(70)90209-6.

Belrose, J. S., and M. J. Burke (1964), Study of the lower ionosphere using partial reflection: 1. Experimental technique and method of analysis, *Journal of Geophysical Research*, *69*(13), 2799–2818, doi: 10.1029/JZ069i013p02799.

Bennett, F., J. Hall, and P. Dickinson (1972), D-region electron densities and collision frequencies from Faraday rotation and differential absorption measurements, *Journal of Atmospheric and Terrestrial Physics*, *34*(8), 1321–1335, doi: 10.1016/0021-9169(72)90188-2.

Berenger, J.-P. (1994), A perfectly matched layer for the absorption of electromagnetic waves, *Journal of Computational Physics*, *114*(2), 185–200, doi: 10.1006/JCPH.1994.1159.

Bickel, J. E. (1957), A method for obtaining LF oblique-incidence reflection coefficients and its application to 135.6-kc/s data in the Alaskan area, *Journal of Geophysical Research*, *62*(3), 373–381, doi: 10.1029/JZ062i003p00373.

Bilitza, D., D. Altadill, V. Truhlik, V. Shubin, I. Galkin, B. Reinisch, and X. Huang (2017), International Reference Ionosphere 2016: From ionospheric climate to real-time weather predictions, *Space Weather*, *15*(2), 418–429, doi: 10.1002/2016SW001593.

Bowles, K. L., B. B. Balsley, and R. Cohen (1963), Field-aligned E -region irregularities identified with acoustic plasma waves, *Journal of Geophysical Research*, *68*(9), 2485–2501, doi: 10.1029/jz068i009p02485.

Bramley, E. (1951), Diversity effects in spaced-aerial reception of ionospheric waves, *Proceedings of the IEE - Part III: Radio and Communication Engineering*, *98*(51), 19–25, doi: 10.1049/pi-3.1951.0004.

Briggs, B. H., G. J. Phillips, and D. H. Shinn (1950), The analysis of observations on spaced receivers of the fading of radio signals, *Proceedings of the Physical Society. Section B*, *63*(2), 106–121, doi: 10.1088/0370-1301/63/2/305.

Budden, K. G. (1955a), The numerical solution of differential equations governing reflexion of long radio waves from the ionosphere, *Proceedings of the Royal Society of London. Series A. Mathematical and Physical Sciences*, *227*(1171), 516–537, doi: 10.1098/rspa.1955.0027.

Budden, K. G. (1955b), The Numerical Solution of the Differential Equations Governing the Reflexion of Long Radio Waves from the Ionosphere. II, *Philosophical Transactions of the Royal Society A: Mathematical, Physical and Engineering Sciences*, *248*(939), 45–72, doi: 10.1098/rsta.1955.0009.

Budden, K. G. (1985), *The propagation of radio waves*, Cambridge University Press, Cambridge, doi: 10.1017/CBO9780511564321.

Burton, E., and E. Boardman (1933), Audio-Frequency Atmospherics, *Proceedings of the IRE*, *21*(10), 1476–1494, doi: 10.1109/JRPROC.1933.227485.

Chapman, S., and T. Cowling (1970), *The Mathematical Theory of Non-Uniform Gases*, Cambridge University Press, Cambridge, England.

Clarke, C. (1962), Atmospheric radio-noise studies based on amplitude-probability measurements at Slough, England, during the International Geophysical Year, *Proceedings of the IEE Part B: Electronic and Communication Engineering*, *109*(47), 393, doi: 10.1049/pi-b-2.1962.0224.

Clilverd, M. A., N. R. Thomson, and C. J. Rodger (1999), Sunrise effects on VLF signals propagating over a long north-south path, *Radio Science*, *34*(4), 939–948, doi: 10.1029/1999RS900052.

Clilverd, M. A., C. J. Rodger, N. R. Thomson, J. Lichtenberger, P. Steinbach, P. Cannon, and M. J. Angling (2001), Total solar eclipse effects on VLF signals: Observations and modeling, *Radio Science*, *36*(4), 773–788, doi: 10.1029/2000RS002395.

Cohen, M. (2009), ELF/VLF phased array generation via frequency-matched steering of a continuous HF ionospheric heating beam, Ph. D. thesis, Stanford University, 2009.

Cohen, M., U. Inan, and E. Paschal (2010), Sensitive Broadband ELF/VLF Radio Reception With the AWESOME Instrument, *IEEE Transactions on Geoscience and Remote Sensing*, *48*(1), 3–17, doi: 10.1109/TGRS.2009.2028334.

Cohen, M. B., N. G. Lehtinen, and U. S. Inan (2012), Models of ionospheric VLF absorption of powerful ground based transmitters, *Geophysical Research Letters*, *39*(24), n/a–n/a, doi: 10.1029/2012GL054437.

Cohen, M. B., N. C. Gross, M. A. Higginson-Rollins, R. A. Marshall, M. Gołkowski, W. Liles, D. Rodriguez, and J. Rockway (2018a), The Lower Ionospheric VLF/LF Response to the 2017 Great American Solar Eclipse Observed Across the Continent, *Geophysical Research Letters*, *45*(8), 3348–3355, doi: 10.1002/2018GL077351.

Cohen, M. B., R. K. Said, E. W. Paschal, J. C. McCormick, N. C. Gross, L. Thompson, M. Higginson-Rollins, U. S. Inan, and J. Chang (2018b), Broadband longwave radio remote sensing instrumentation, *Review of Scientific Instruments*, *89*(9), 094,501, doi: 10.1063/1.5041419.

Coster, A. J., L. Goncharenko, S. R. Zhang, P. J. Erickson, W. Rideout, and J. Vierinen (2017), GNSS Observations of Ionospheric Variations During the 21 August 2017 Solar Eclipse, *Geophysical Research Letters*, *44*(24), 12,041–12,048, doi: 10.1002/2017GL075774.

Cummer, S. A. (2000), Modeling electromagnetic propagation in the Earth-ionosphere waveguide, *IEEE Transactions on Antennas and Propagation*, *48*(9), 1420–1429, doi: 10.1109/8.898776.

Cummer, S. A., U. S. Inan, and T. F. Bell (1998), Ionospheric D region remote sensing using VLF radio atmospherics, *Radio Science*, *33*(6), 1781–1792, doi: 10.1029/98RS02381.

Cummins, K. L., and M. J. Murphy (2009), An Overview of Lightning Locating Systems: History, Techniques, and Data Uses, With an In-Depth Look at the U.S. NLDN, *IEEE Transactions on Electromagnetic Compatibility*, *51*(3), 499–518, doi: 10.1109/TEMC.2009.2023450.

Doviak, J., J. Lataitis, L. Holloway, and J. Van Baelen (1994), A Generalized Theoretical Analysis of Cross-correlation and Cross-spectra for Spaced-antenna Wind Profilers, doi: 10.5065/D6N014G4.

Durgin, G. (2002), Space-Time Wireless Channels, *Space-Time Wireless Channels*, pp. 1–19, doi: 10.1300/J155v04n04_01.

Emerson, M. (2018), Federal Register :: Discontinuance of the Nationwide Differential Global Positioning System (NDGPS).

Ferguson, J. A. (1980), Ionospheric profiles for predicting nighttime VLF/LF propagation, *Naval Ocean Systems Center Tech. Rep. NOSC/TR 530, NTIS Accession. ADA085399.*

Ferguson, J. A. (1998), Computer Programs for Assessment of Long-Wavelength Radio Communications, Version 2.0: User's Guide and Source Files.

Füllekrug, M., A. Mezentsev, R. Watson, S. Gaffet, I. Astin, and A. Evans (2014), Array analysis of electromagnetic radiation from radio transmitters for submarine communication, *Geophysical Research Letters*, *41*(24), 9143–9149, doi: 10.1002/2014GL062126.

Füllekrug, M., N. Smith, A. Mezentsev, R. Watson, I. Astin, S. Gaffet, A. Evans, and M. Rycroft (2015a), Multipath propagation of low-frequency radio waves inferred from high-resolution array analysis, *Radio Science*, *50*(11), 1141–1149, doi: 10.1002/2015RS005781.

Füllekrug, M., A. Mezentsev, R. Watson, S. Gaffet, I. Astin, N. Smith, and A. Evans (2015b), Map of low-frequency electromagnetic noise in the sky, *Geophysical Research Letters*, *42*(11), 4648–4653, doi: 10.1002/2015GL064142.

Füllekrug, M., Z. Liu, K. Koh, A. Mezentsev, S. Pedeboy, S. Soula, S.-E. Enno, J. Sugier, and M. J. Rycroft (2016), Mapping lightning in the sky with a mini array, *Geophysical Research Letters*, *43*(19), 10,448–10,454, doi: 10.1002/2016GL070737.

Gross, N. C., M. B. Cohen, R. K. Said, and M. Gołkowski (2018), Polarization of Narrowband VLF Transmitter Signals as an Ionospheric Diagnostic, *Journal of Geophysical Research: Space Physics*, *123*(1), 901–917, doi: 10.1002/2017JA024907.

Han, F., and S. A. Cummer (2010), Midlatitude nighttime D region ionosphere variability on hourly to monthly time scales, *Journal of Geophysical Research: Space Physics*, *115*(9), doi: 10.1029/2010JA015437.

Han, F., S. A. Cummer, J. Li, and G. Lu (2011), Daytime ionospheric D region sharpness derived from VLF radio atmospherics, *Journal of Geophysical Research: Space Physics*, *116*(5), doi: 10.1029/2010JA016299.

Hastings, F. D., J. B. Schneider, and S. L. Broschat (1995), Monte-Carlo FDTD technique for rough surface scattering, *IEEE Transactions on Antennas and Propagation*, *43*(11), 1183–1191, doi: 10.1109/8.475089.

Higginson-Rollins, M. A., and M. B. Cohen (2017), Exploiting LF/MF signals of opportunity for lower ionospheric remote sensing, *Geophysical Research Letters*, *44*(16), 8665–8671, doi: 10.1002/2017GL074236.

Hocking, W. (1987), Reduction of the effects of non-stationarity in studies of amplitude statistics of radio wave backscatter, *Journal of Atmospheric and Terrestrial Physics*, *49*(11-12), 1119–1131, doi: 10.1016/0021-9169(87)90094-8.

Hocking, W., and R. Vincent (1982), A comparison between HF partial reflection profiles from the D-region and simultaneous Langmuir probe electron density measurements, *Journal of Atmospheric and Terrestrial Physics*, *44*(10), 843–854, doi: 10.1016/0021-9169(82)90037-X.

Hoy, R. D. (1969), The effect of a total solar eclipse on the phase of long path v.l.f. transmissions, *Journal of Atmospheric and Terrestrial Physics*, *31*(7), 1027–1028, doi: 10.1016/0021-9169(69)90149-4.

Hu, W., and S. Cummer (2006), An FDTD Model for Low and High Altitude Lightning-Generated EM Fields, *IEEE Transactions on Antennas and Propagation*, *54*(5), 1513–1522, doi: 10.1109/TAP.2006.874336.

Huxley, L., and J. Ratcliffe (1949), A survey of ionospheric cross-modulation (wave interaction or Luxembourg effect), *Journal of the Institution of Electrical Engineers*, *1949*(11), 276–276, doi: 10.1049/jiee-2.1949.0126.

Inan, U. S., A. Slingeland, V. P. Pasko, and J. V. Rodriguez (1996a), VLF and LF signatures of mesospheric/lower ionospheric response to lightning discharges, *Journal of Geophysical Research: Space Physics*, *101*(A3), 5219–5238, doi: 10.1029/95JA03514.

Inan, U. S., V. P. Pasko, and T. F. Bell (1996b), Sustained heating of the ionosphere above thunderstorms as evidenced in "early/fast" VLF events, *Geophysical Research Letters*, *23*(10), 1067–1070, doi: 10.1029/96GL01360.

Inan, U. S., S. A. Cummer, and R. A. Marshall (2010), A survey of ELF and VLF research on lightning-ionosphere interactions and causative discharges, *Journal of Geophysical Research: Space Physics*, *115*(A6), n/a–n/a, doi: 10.1029/2009JA014775.

ITU-R (2017), Electrical Characteristics of The Surface of The Earth, *Tech. rep.*

Jacobson, A. R., R. Holzworth, and X. M. Shao (2008), Low-frequency ionospheric sounding with Narrow Bipolar Event lightning radio emissions: Energy-reflectivity spectrum, *Annales Geophysicae*, *26*(7), 1793–1803, doi: 10.5194/angeo-26-1793-2008.

Johnson, M. P., U. S. Inan, S. J. Lev-Tov, and T. F. Bell (1999), Scattering pattern of lightning-induced ionospheric disturbances associated with early/fast VLF events, *Geophysical Research Letters*, *26*(15), 2363–2366, doi: 10.1029/1999GL900521.

Kane, J. A. (1961), Re-evaluation of ionospheric electron densities and collision frequencies derived from rocket measurements of refractive index and attenuation, *Journal of Atmospheric and Terrestrial Physics*, *23*(C), 338–347, doi: 10.1016/0021-9169(61)90056-3.

Kaufmann, P., and R. Schaal (1968), The effect of a total solar eclipse on long path VLF transmission, *Journal of Atmospheric and Terrestrial Physics*, *30*(3), 469–471, doi: 10.1016/0021-9169(68)90119-0.

Koh, K. L., Z. Liu, and M. Füllekrug (2018), Lower Ionosphere Effects on Narrowband Very Low Frequency Transmission Propagation: Fast Variabilities and Frequency Dependence, *Radio Science*, *53*(5), 611–623, doi: 10.1002/2017RS006456.

Kotovsky, D. A., and R. C. Moore (2016), Photochemical response of the nighttime mesosphere to electric field heating-Onset of electron density enhancements, *Journal of Geophysical Research: Space Physics*, *121*(5), 4782–4799, doi: 10.1002/2015JA022054.

Kumar, S., S. NaitAmor, O. Chanrion, and T. Neubert (2017), Perturbations to the lower ionosphere by tropical cyclone Evan in the South Pacific Region, *Journal of Geophysical Research: Space Physics*, *122*(8), 8720–8732, doi: 10.1002/2017JA024023.

Last, D., and D. Poppe (1996), A Coverage Prediction Model for Radio Beacon Differential Satellite Navigation Systems, *Navigation*, *43*(4), 451–469, doi: 10.1002/j.2161-4296.1996.tb01932.x.

Last, J., and D. Poppe (1997), Effect of skywave interference on coverage of radiobeacon DGPS stations, *IEE Proceedings - Radar, Sonar and Navigation*, *144*(3), 163, doi: 10.1049/ip-rsn:19971177.

Lay, E. H., and X. M. Shao (2011a), Multi-station probing of thunderstorm-generated D-layer fluctuations by using time-domain lightning waveforms, *Geophysical Research Letters*, *38*(23), n/a–n/a, doi: 10.1029/2011GL049790.

Lay, E. H., and X. M. Shao (2011b), High temporal and spatial - resolution detection of D - layer fluctuations by using time - domain lightning waveforms, *Journal of Geophysical Research: Space Physics*, *116*(January), 1–8, doi: 10.1029/2010JA016018.

Lee, J. H., and D. K. Kalluri (1999), Three-dimensional FDTD simulation of electromagnetic wave transformation in a dynamic inhomogeneous magnetized plasma, *IEEE Transactions on Antennas and Propagation*, *47*(7), 1146–1151, doi: 10.1109/8.785745.

Lehtinen, N. G., and U. S. Inan (2008), Radiation of ELF/VLF waves by harmonically varying currents into a stratified ionosphere with application to radiation by a modulated electrojet, *Journal of Geophysical Research: Space Physics*, *113*(A6), n/a–n/a, doi: 10.1029/2007JA012911.

Lehtinen, N. G., and U. S. Inan (2009), Full-wave modeling of transionospheric propagation of VLF waves, *Geophysical Research Letters*, *36*(3), n/a–n/a, doi: 10.1029/2008GL036535.

Lehtinen, N. G., R. A. Marshall, and U. S. Inan (2010), Full-wave modeling of "early" VLF perturbations caused by lightning electromagnetic pulses, *Journal of Geophysical Research: Space Physics*, *115*(A7), n/a–n/a, doi: 10.1029/2009JA014776.

Lindner, B. (1975a), The Nature of D-region Scattering of Vertical Incidence Radio Waves. II. Experimental Observations Using Spaced Antenna Reception, *Australian Journal of Physics*, *28*(2), 171, doi: 10.1071/PH750171.

Lindner, B. (1975b), The Nature of D-region Scattering of Vertical Incidence Radio Waves. I. Generalized Statistical Theory of Diversity Effects Between Spaced Receiving Antennas, *Australian Journal of Physics*, *28*(2), 163, doi: 10.1071/PH750163.

Lynn, K. J. (1981), The total solar eclipse of 23 October 1976 observed at VLF, *Journal of Atmospheric and Terrestrial Physics*, *43*(12), 1309–1316, doi: 10.1016/0021-9169(81)90156-2.

Manninen, A. T. (1997), Surface roughness of Baltic sea ice, *Journal of Geophysical Research C: Oceans*, *102*(1), 1119–1139, doi: 10.1029/96jc02991.

Marshall, R. A. (2012), An improved model of the lightning electromagnetic field interaction with the D-region ionosphere, *Journal of Geophysical Research: Space Physics*, *117*(A3), n/a–n/a, doi: 10.1029/2011JA017408.

Mathews, J. (1984), The incoherent scatter radar as a tool for studying the ionospheric D-region, *Journal of Atmospheric and Terrestrial Physics*, *46*(11), 975–986, doi: 10.1016/0021-9169(84)90004-7.

Mathews, J. D., J. H. Shapiro, and B. S. Tanenbaum (1973), Evidence for distributed scattering in D region partial-reflection processes, *Journal of Geophysical Research*, *78*(34), 8266–8275, doi: 10.1029/JA078i034p08266.

Maurya, A. K., M. B. Cohen, K. Niranjan Kumar, D. Phanikumar, R. Singh, P. Vineeth, and K. Kishore Kumar (2019), Observation of Very Short Period Atmospheric Gravity Waves in the Lower Ionosphere Using Very Low Frequency Waves, *Journal of Geophysical Research: Space Physics*, *124*(11), 9448–9461, doi: 10.1029/2019JA027360.

McKerrow, C. (1957), Some Recent Measurements of Atmospheric Noise in Canada, *Proceedings of the IRE*, *45*(6), 782–786, doi: 10.1109/JRPROC.1957.278475.

McKerrow, C. A. (1960), Some measurements of atmospheric noise levels at low and very low frequencies in Canada, *Journal of Geophysical Research*, *65*(7), 1911–1926, doi: 10.1029/JZ065i007p01911.

McRae, W. M., and N. R. Thomson (2000), VLF phase and amplitude: Daytime ionospheric parameters, *Journal of Atmospheric and Solar-Terrestrial Physics*, *62*(7), 609–618, doi: 10.1016/S1364-6826(00)00027-4.

McRae, W. M., and N. R. Thomson (2004), Solar flare induced ionospheric D-region enhancements from VLF phase and amplitude observations, *Journal of Atmospheric and Solar-Terrestrial Physics*, *66*(1), 77–87, doi: 10.1016/j.jastp.2003.09.009.

Mechtly, E. A. (1974), Accuracy of rocket measurements of lower ionosphere electron concentrations, *Radio Science*, *9*(3), 373–378, doi: 10.1029/RS009i003p00373.

Morfitt, D. G. (1977), Effective electron density distributions describing VLF/ELF propagation data, *National Technical Information Service Springfield*, *NTIS Acces*(Naval Ocean Systems Center Technical Report NOSC/TR 141).

Nagano, I., M. Mambo, and G. Hutatsuishi (1975), Numerical calculation of electromagnetic waves in an anisotropic multilayered medium, *Radio Science*, *10*(6), 611–617, doi: 10.1029/RS010i006p00611.

Newman, D. B., and A. J. Ferraro (1976), Amplitude distributions of partially reflected signals from the mid-latitude D region, *Journal of Geophysical Research*, *81*(13), 2442–2444, doi: 10.1029/JA081i013p02442.

Nicolet, M., and A. C. Aikin (1960), The formation of the D region of the ionosphere, *Journal of Geophysical Research*, *65*(5), 1469–1483, doi: 10.1029/JZ065i005p01469.

Norton, K. A., and A. C. Omberg (1947), The Maximum Range of a Radar Set, *Proceedings of the IRE*, *35*(1), 4–24, doi: 10.1109/JRPROC.1947.231216.

Ogilvy, J. A. (1991), *Theory of Wave Scattering From Random Rough Surfaces*, 292 pp., Taylor & Francis.

P. Beckmann, and A. Spizzichino (1963), *The Scattering of Electromagnetic Waves from Rough Surfaces*, 503 pp., Pergamon Press, New York.

Pfaff, R., R. Holzworth, R. Goldberg, H. Freudenreich, H. Voss, C. Croskey, J. Mitchell, J. Gumbel, S. Bounds, W. Singer, and R. Latteck (2001), Rocket probe observations of electric field irregularities in the polar summer mesosphere, *Geophysical Research Letters*, *28*(8), 1431–1434, doi: 10.1029/2000GL012677.

Picone, J. M., A. E. Hedin, D. P. Drob, and A. C. Aikin (2002), NRLMSISE-00 empirical model of the atmosphere: Statistical comparisons and scientific issues, *Journal of Geophysical Research: Space Physics*, *107*(A12), doi: 10.1029/2002JA009430.

Piggott, W. (1953), The reflection and absorption of radio waves in the ionosphere, *Proceedings of the IEE - Part III: Radio and Communication Engineering*, *100*(64), 61–72, doi: 10.1049/pi-3.1953.0015.

Piggott, W. R., M. L. V. Pitteway, and E. V. Thrane (1965), The Numerical Calculation of Wave-Fields, Reflexion Coefficients and Polarizations for Long Radio Waves in the Lower Ionosphere. II, *Philosophical Transactions of the Royal Society A: Mathematical, Physical and Engineering Sciences*, *257*(1079), 243–271, doi: 10.1098/rsta.1965.0005.

Pitteway, M. L. V. (1959), Reflexion Levels and Coupling Regions in a Horizontally Stratified Ionosphere, *Philosophical Transactions of the Royal Society A: Mathematical, Physical and Engineering Sciences*, *252*(1004), 53–68, doi: 10.1098/rsta.1959.0014.

Pitteway, M. L. V. (1965), The Numerical Calculation of Wave-Fields, Reflexion Coefficients and Polarizations for Long Radio Waves in the Lower Ionosphere. I., *Philosophical Transactions of the Royal Society A: Mathematical, Physical and Engineering Sciences*, *257*(1079), 219–241, doi: 10.1098/rsta.1965.0004.

Rastogi, P. K., and O. Holt (1981), On detecting reflections in presence of scattering from amplitude statistics with application to D region partial reflections, *Radio Science*, *16*(6), 1431–1443, doi: 10.1029/RS016i006p01431.

Ratcliffe, J. (1959), *The magneto-ionic theory and its applications to the ionosphere.*

Ratcliffe, J. A. (1956), Some aspects of diffraction theory and their application to the ionosphere, *Reports on Progress in Physics*, *19*(1), 188–267, doi: 10.1088/0034-4885/19/1/306.

Reid, G. C. (1970), Production and loss of electrons in the quiet daytime D region of the ionosphere, *Journal of Geophysical Research*, *75*(13), 2551–2562, doi: 10.1029/JA075i013p02551.

Roden, J. A., and S. D. Gedney (2000), Convolution PML (CPML): An efficient FDTD implementation of the CFS-PML for arbitrary media, *Microwave and Optical Technology Letters*, *27*(5), 334–339, doi: 10.1002/1098-2760(20001205)27:5⟨334::AID-MOP14⟩3.0.CO;2-A.

Rodger, C. J., M. A. Clilverd, and R. L. Dowden (2002), D region reflection height modification by whistler-induced electron precipitation, *Journal of Geophysical Research: Space Physics*, *107*(A7), 1145, doi: 10.1029/2001JA000311.

Røyrvik, O., and L. G. Smith (1984), Comparison of mesospheric VHF radar echoes and rocket probe electron concentration measurements, *Journal of Geophysical Research*, *89*(A10), 9014, doi: 10.1029/JA089iA10p09014.

Salut, M. M., M. B. Cohen, M. A. M. Ali, K. L. Graf, B. R. T. Cotts, and S. Kumar (2013), On the relationship between lightning peak current and Early VLF perturbations, *Journal of Geophysical Research: Space Physics*, *118*(11), 7272–7282, doi: 10.1002/2013JA019087.

Schaal, R. E., A. M. Mendes, S. Ananthakrishnan, and P. Kaufmann (1970), VLF propagation effects produced by the eclipse, *Nature*, *226*(5251), 1127–1129, doi: 10.1038/2261127a0.

Schunk, R. W., and A. F. Nagy (2000), Ionospheres: Physics, plasma physics, and chemistry, *Space Sci. Ser*, *59*, 554.

Sears, R. D. (1965), Cosmic noise absorption and VLF phase measurements on the eclipse of May 30, 1965, *Journal of Geophysical Research*, *70*(23), 5967–5969, doi: 10.1029/jz070i023p05967.

Sechrist, C. F. (1974), Comparisons of techniques for measurement of D-region electron densities, *Radio Science*, *9*(2), 137–149, doi: 10.1029/RS009i002p00137.

Seddon, J. C. (1953), Propagation measurements in the ionosphere with the aid of rockets, *Journal of Geophysical Research*, *58*(3), 323–335, doi: 10.1029/JZ058i003p00323.

Shapiro, J. H. (1973), Statistical models for D-region partial-reflection experiments, *Radio Science*, *8*(5), 431–435, doi: 10.1029/RS008i005p00431.

Singletary, P. (2020), Using a High-Speed Plasma as a Conducting Channel to Enable a Novel Antenna Approach, Ph.D. thesis, Georgia Institute of Technology.

Spetzler, J., and R. Snieder (2001a), The formation of caustics in two-and three-dimensional media, *Geophysical Journal International*, *144*(1), 175–182, doi: 10.1046/j.1365-246X.2001.00308.x.

Spetzler, J., and R. Snieder (2001b), The effect of small-scale heterogeneity on the arrival time of waves, *Geophysical Journal International*, *145*(3), 786–796, doi: 10.1046/j.1365-246X.2001.01438.x.

Spetzler, J., C. Sivaji, O. Nishizawa, and Y. Fukushima (2002), A test of ray theory and scattering theory based on a laboratory experiment using ultrasonic waves and numerical simulation by finite-difference method, *Geophysical Journal International*, *148*(2), 165–178, doi: 10.1046/j.1365-246X.2002.01552.x.

Sprenger, K., E. Lauter, and K. Schmelovsky (1962), Solar eclipse effects in low and medium frequency propagation, *Journal of Atmospheric and Terrestrial Physics*, *24*(12), 1041–1057, doi: 10.1016/0021-9169(62)90159-9.

Strutt, J. W. (2011), *The theory of sound*, vol. 9781108032, 1–326 pp., doi: 10.1017/CBO9781139058087.

Šulić, D. M., V. A. Srećković, and A. A. Mihajlov (2016a), A study of VLF signals variations associated with the changes of ionization level in the D-region in consequence of solar conditions, *Advances in Space Research*, *57*(4), 1029–1043, doi: 10.1016/j.asr.2015.12.025.

Šulić, D. M., V. A. Srećković, and A. A. Mihajlov (2016b), A study of VLF signals variations associated with the changes of ionization level in the D-region in consequence of solar conditions, *Advances in Space Research*, *57*(4), 1029–1043, doi: 10.1016/j.asr.2015.12.025.

Tan, L. M., N. N. Thu, T. Q. Ha, and Q. Nguyen-Luong (2015), Seasonal variations of nighttime D-region ionosphere in 2013 solar maximum observed from a low-latitude station, *Earth, Planets and Space*, *67*(1), doi: 10.1186/s40623-015-0331-y.

Tanenbaum, B. S., J. H. Shapiro, and J. E. Reed (1973), Phase-difference distributions in a D-region partial-reflection experiment, *Radio Science*, *8*(5), 437–448, doi: 10.1029/RS008i005p00437.

Thébault, E., C. C. Finlay, C. D. Beggan, P. Alken, J. Aubert, O. Barrois, F. Bertrand, T. Bondar, A. Boness, L. Brocco, E. Canet, A. Chambodut, A. Chulliat, P. Coïsson, F. Civet, A. Du, A. Fournier, I. Fratter, N. Gillet, B. Hamilton, M. Hamoudi, G. Hulot, T. Jager, M. Korte, W. Kuang, X. Lalanne, B. Langlais, J. M. Léger, V. Lesur, F. J. Lowes, S. Macmillan, M. Mandea, C. Manoj, S. Maus, N. Olsen, V. Petrov, V. Ridley, M. Rother, T. J. Sabaka, D. Saturnino, R. Schachtschneider, O. Sirol, A. Tangborn, A. Thomson, L. Tøffner-Clausen, P. Vigneron, I. Wardinski, and T. Zvereva (2015), International geomagnetic reference field: The 12th generation international geomagnetic reference field - The twelfth generation, *Earth, Planets and Space*, *67*(1), doi: 10.1186/s40623-015-0228-9.

Thomson, N. R. (1993), Experimental daytime VLF ionospheric parameters, *Journal of Atmospheric and Terrestrial Physics*, *55*(2), 173–184, doi: 10.1016/0021-9169(93)90122-F.

Thomson, N. R., M. A. Clilverd, and W. M. McRae (2007), Nighttime ionospheric D region parameters from VLF phase and amplitude, *Journal of Geophysical Research: Space Physics*, *112*(7), n/a–n/a, doi: 10.1029/2007JA012271.

Thrane, E. V., and W. R. Piggott (1966), The collision frequency in the E- and D-regions of the ionosphere, *Journal of Atmospheric and Terrestrial Physics*, *28*(8), 721–737, doi: 10.1016/0021-9169(66)90021-3.

von Biel, H. (1981), A statistical assessment of synoptic D-region partial reflection data, *Journal of Atmospheric and Terrestrial Physics*, *43*(3), 225–230, doi: 10.1016/0021-9169(81)90043-X.

von Biel, H. A. (1971), Amplitude distributions of D -region partial reflections, *Journal of Geophysical Research*, *76*(34), 8365–8367, doi: 10.1029/JA076i034p08365.

Wait, J., and K. Spies (1964), Characteristics of the Earth-ionosphere waveguide for VLF radio waves.

Wait, J. R., and A. Murphy (1956), Multiple reflections between the earth and the ionosphere in V.L.F. propagation, *Geofisica Pura e Applicata*, *35*(1), 61–72, doi: 10.1007/BF02122867.

Wernik, A. W., C. H. Liu, and K. C. Yeh (1983), Modeling of spaced-receiver scintillation measurements, *Radio Science*, *18*(5), 743–764, doi: 10.1029/RS018i005p00743.

Wolfe, D. B., C. L. Judy, E. J. Haukkala, and D. J. Godfrey (2000), Engineering The World's Largest DGPS Network, *Control Engineering*, *1*(June), 26–28, doi: 10.1109/OCEANS.2000.881237.

Yee, K. S. (1966), Numerical Solution of Initial Boundary Value Problems Involving Maxwell's Equations in Isotropic Media, doi: 10.1109/TAP.1966.1138693.